Molecular-level characterization of curved water interfaces with sum frequency and second harmonic scattering

THIS IS A TEMPORARY TITLE PAGE

It will be replaced for the final print by a version
provided by the service academique

THÈSE No XXXX (2017)

PRÉSENTÉE LE 27 SEPTEMBRE 2017

À LA FACULTÉ DES SCIENCES ET TECHNIQUES DE L'INGÉNIEUR
CHAIRE JULIA JACOBI DE PHOTOMÉDECINE - LABORATOIRE DE BIOPHOTONIQUE FONDAMENTALE
PROGRAMME DOCTORAL EN PHOTONIQUE

ÉCOLE POLYTECHNIQUE FÉDÉRALE DE LAUSANNE

POUR L'OBTENTION DU GRADE DE DOCTEUR ÈS SCIENCES

PAR

Nikolay SMOLENTSEV

acceptée sur proposition du jury :

Prof. Jacques-Edouard Moser, président du jury

Prof. Sylvie Roke, directrice de thèse

Prof. Esther Amstad, rapporteuse

Prof. Huib Bakker, rapporteur

Prof. Peter Hamm, rapporteur

Suisse
2017

Acknowledgements

First and foremost, I would like to acknowledge my supervisor, Professor Sylvie Roke, for giving me the opportunity to work on the exciting projects in the laboratory for fundamental biophotonics, for her dedicated guidance and continuous support. She spent countless hours teaching me, correcting my manuscripts and replies to referees and, finally, the thesis as well as discussing with me many other even not directly related scientific problems. I am really glad that I had a chance to work with her and enjoyed the great atmosphere in the lab at the forefront of science with talented people around. Furthermore, in Sylvie's lab, I have been working with some of the best experimental setups in the world and had access to virtually any chemical compound. It was an amazing experience.

I would like to thank members of my committee: Prof. Esther Amstad, Prof. Peter Hamm, Prof. Jacques-Eduard Moser and especially Prof. Huib Bakker for reading my thesis and their feedback. Prof. Huib Bakker was also a collaborator in one of the projects, and I acknowledge him for critical remarks and insightful ideas.

Many thanks to Kailash Jena, who taught me how to work in an optical laboratory and introduced me to the SFS technique during my first year at the EPFL. I would like to especially thank my co-authors and the whole LBP group. I thank Cornelis Lütgebaucks, for his important contribution in the lipid project, and for so much fun and interesting discussions about that. I thank Halil Okur for his support, not only related to chemistry but also for some help related to my family life. Many thanks also go to Yixing Chen and Alex de Beer for their help and fruitful discussions. Of course, thanks to all my officemates during these years for creating such productive atmosphere: Evi, Nicos, Filip, Katja; and the entire LBP team, especially persons who started before me, Carlos and Rüdiger, for sharing their knowledge and for wonderful discussions. I would also like to thank Vitalijs for making great time-saving sample during his short stay in our lab. I thank Marie and Rebecca for all their nice cakes. Thanks to my collaborators outside of the EPFL: Matthew Brown and Wilbert Smit. I also thank all the people not mentioned above who might be related to this thesis and the staff of the Southern Federal University where I obtained an excellent education which helped me to succeed with the thesis here.

Last but not least, I would like to thank my family: my brother Grigory, who has always been the great example for me to follow, my father, Yuriy, and my wife Tamara and our children Elizaveta and Leon for all their love, patience and all the inspiration they gave me.

Abstract

Aqueous interfaces are omnipresent in nature. Some of them are visible: droplets in clouds, aerosols, and surfaces of oceans, lakes, and rivers. Many more surfaces are hidden: water in contact with cell membranes, proteins, and the surface of droplets in emulsions. The hydrophobic interaction plays a key role in many biological and industrial processes; hence understanding of water structure at the hydrophobic interfaces is needed. To elucidate molecular-level water structure at these interfaces and to learn about the molecular-level mechanisms behind hydrophobicity we use sum frequency and second harmonic scattering spectroscopy. We apply these techniques to probe the molecular structure (orientational order and strength of the hydrogen bonds) at the interfaces of droplet and liposomes. First, we demonstrate a way to use the focusing properties of a liquid jet for nonlinear scattering experiments. As the jet surface is continuously refreshed, reduced heating effects and cleanliness are advantages of this technique. Then, investigating water structure in water droplets in oil, we find that hydrogen bonds of water at the surface of the droplet resemble that of planar oil/water interface made of the same chemicals at 50°C lower temperature. Using water droplets dispersed in CCl_4 we show that second harmonic scattering data has a high sensitivity to the ionic strength of the solution. We estimate the concentration of free charge carriers (reverse micelles and hydrated ions) and discuss changes in the surface water ordering and the surface potential, which reflect the formation of reversed micelles at the droplet interface. Finally, we study water and lipid transmembrane asymmetry using liposomes composed of neutral and charged lipids, which are a good model system of a phospholipid bilayer of a cell membrane. We calculate the distribution of the phosphate tilt angle and quantify lipid transmembrane asymmetry. Furthermore, we discuss a mechanism responsible for the observed lipid asymmetry that involves intermolecular hydrogen bonding between phosphate and amine groups of adjacent lipids.

Keywords

Water, hydrophobicity, nanoscale interfaces, droplets, membranes, lipid, liquid jet, sum frequency generation, second harmonic generation, nonlinear light scattering

Résumé

Les interfaces aqueuses sont omniprésentes dans la nature. Certaines d'entre elles sont visibles : les gouttelettes dans les nuages, les aérosols, et les surfaces des océans, des lacs et des rivières. Beaucoup plus de surfaces sont cachées : l'eau en contact avec les membranes cellulaires, les protéines, et la surface des gouttelettes dans les émulsions. L'interaction hydrophobe joue un rôle clé dans de nombreux processus biologiques et industriels; la compréhension de la structure de l'eau aux interfaces hydrophobes est donc nécessaire. Pour élucider cette structure au niveau moléculaire et pour connaître les mécanismes liés à l'hydrophobicité, nous utilisons la spectroscopie de diffusion de la fréquence somme et de second harmonique. Nous appliquons ces techniques pour sonder la structure moléculaire (ordre orientationnel et force des liaisons hydrogènes) aux interfaces des gouttelettes et des liposomes. Tout d'abord, nous démontrons un moyen d'utiliser les propriétés de focalisation d'un jet de liquide pour des expériences de diffusion lumineuse non linéaire. Comme la surface du jet est continuellement renouvelée, cette technique a pour avantage de réduire les effets de chauffage et de contamination. Ensuite, en étudiant la structure de l'eau présente en gouttelettes dans l'huile, nous constatons que les liaisons hydrogène de l'eau à la surface des goutelettes sont similaires à celles d'une interface planaire huile/eau faite des mêmes produits chimiques maintenue à une température de 50°C plus basse. En utilisant des gouttelettes d'eau dispersées dans du tétrachlorométhane (CCl_4), nous montrons que les données de diffusion de second harmonique présentent une forte sensibilité à la force ionique de la solution. Nous estimons la concentration des porteurs de charge libres (micelles inverses et ions hydratés) et discutons des changements dans l'ordre des molécules d'eau à la surface et du potentiel de surface, qui reflètent la formation de micelles inversées à l'interface des gouttelettes. Enfin, nous étudions l'asymétrie transmembranaire de l'eau et des lipides en utilisant des liposomes composés de lipides neutres et chargés, qui constituent un bon modèle de membrane cellulaire avec une bicouche phospholipidique. Nous calculons la répartition de l'angle d'inclinaison du groupement phosphate des lipides, et quantifions leur asymétrie transmembranaire. En outre, nous discutons d'un mécanisme responsable de l'asymétrie lipidique observée, impliquant une liaison hydrogène intermoléculaire entre les groupes phosphate et amine de lipides adjacents.

Mots-clés

Eau, hydrophobie, interfaces de taille nanométriques, gouttes, membranes, lipide, jet d'eau, génération de la fréquence somme, génération de seconde harmonique, diffusion de la lumière non linéaire

Contents

List of Figures

List of Tables

Chapter 1: Introduction

1.1 Water and hydrophobicity

Water is the most important liquid on our planet. Water in the form of white clouds, blue ocean or shiny glaciers covers most of Earth's surface visible from space. But even more water surfaces can be found in living organisms: cell membranes, and the surfaces of proteins or other macromolecules. Water is one of the main components of cells, and it interacts with organic compounds, which contain an enormous amount of non-polar groups (in particular CH_2 and CH_3 groups).

Hydrophobicity is the association of non-polar groups or molecules in an aqueous environment which arises from the tendency of water to exclude non-polar molecules [1]. Interactions and interfaces between hydrophobic liquids and water play a key role in biological [2] and chemical processes [3]. In biology, processes such as enzyme activity, protein folding, catalysis, and membrane formation depend on hydrophobic/water interactions [2]. In chemistry [3, 4], the same holds for processes such as wetting, drug design, aerosol formation and stabilization, nanoparticle and droplet formation and stabilization, and emulsification.

Although a hydrophobic interaction is a common term to describe the interaction of polar water molecules with non-polar molecules, as such, the hydrophobic interaction does not exist. It is used for simplicity to describe the combination of interactions: dipole-dipole interaction in water, dispersion interaction, and hydrogen bonding (H-bonding). In the presence of ions (or dissociated water species H^+ or OH^-) more interactions start to play a role, such as ion-dipole interaction or forces involving induced dipoles. These interactions have different characteristic energy and length scales, but the one that is particularly important for the hydrophobicity is the H-bonding. Apart from that, H-bonding gives rise to unexpectedly high boiling and melting points, a higher density of liquid state compare with solid state, and many more anomalies of liquid water [5].

How can we describe the structure of water? In bulk water there are an average 3.6 H-bonds per water molecule [6] (each water molecule can form up to 4 H-bonds, see Figure 1.1). Moreover, there is a short-range correlation in the spatial distribution of water molecules which can be described with an oxygen-oxygen pair distribution function [5]. Another important parameter is water-water orientational correlations, which may have a long range in the presence of ions [7]. Liquid water is not static: there is a lot of dynamics in bulk water, such as rotational, vibrational,

translational, and librational movement (with characteristic time scales of typically 10-100 fs) as well as diffusion, and proton transfer [8].

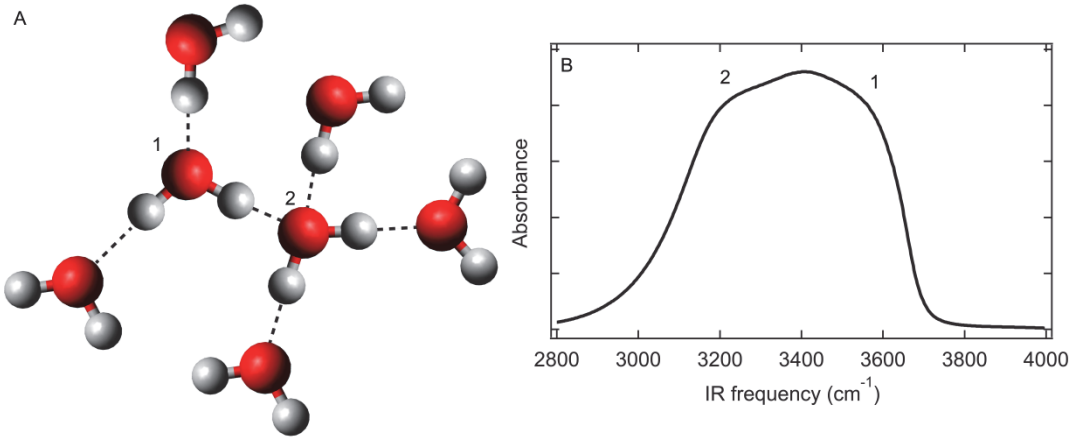

Figure 1.1. A. Water molecules can form up to 4 hydrogen bonds. Water molecules which form all 4 H-bonds are called strongly H-bonded (2), and the ones which form less then 4 H-bonds are called weakly H-bonded molecules (1). B. IR absorption spectrum of water in OH symmetric stretch vibrational region. The strongly H-bonded molecules are responsible for the red side of the spectrum while weakly H-bonded molecules are responsible for the blue part.

At the interface, the situation becomes even more complex. As for the bulk water, the number and strength of H-bonds, as well as preferential orientation of water dipoles are key parameters to describe water structure at the interfaces. The absence of H-bonding or breaking of H-bonds is an essential part of the hydrophobic interaction. The hydrophobic interfaces typically carry negative charge [9, 10]. Their electrostatic surface potential induces water order in the extended region from the interface [3], called diffuse layer. Therefore, the structure of water at hydrophobic interfaces depends on characteristics such as charge, dielectric constant and dipole moment, as well as the molecular shape / geometry and related molecular and interfacial corrugation [11, 12]. The presence of hydrated molecules or hydrated parts of molecules (e.g. headgroups of surfactants) also changes the structure of the surface. Elucidation of water structure in the presence of hydrophobic molecules, ions, surfactants, proteins, and lipids will help to understand the surface chemistry of biointerfaces.

Many types of structures can be formed due to hydrophobic interactions. These structures include droplets standing on a hydrophobic support, emulsions, micelles, bilayers, etc. Some of them are sketched in Figure 1.2. Two immiscible liquids form an emulsion in which droplets of one liquid are dispersed in the second liquid. There are two most common types of emulsions: oil-in-water (milk, mayonnaise) and water-in-oil (butter, creams). Other organic molecules (surfactant and lipids) may stabilize emulsions and form micelles and bilayers in water. Surfactants are organic molecules containing hydrophilic and hydrophobic parts. Depending on the ratio between these two, they may stabilize either oil-in-water or water-in-oil emulsions. Phospholipids are organic molecules which are one of the main constitutes of the eukaryotic cell membrane. They often assem-

ble in bilayers or liposomes in water solutions. A sphere of a bilayer is called a phospholipid vesicle or a liposome. The diameter of liposomes is typically larger than 30 nm. All above mentioned structures are omnipresent in our organisms and their surface properties define functions of biointerfaces.

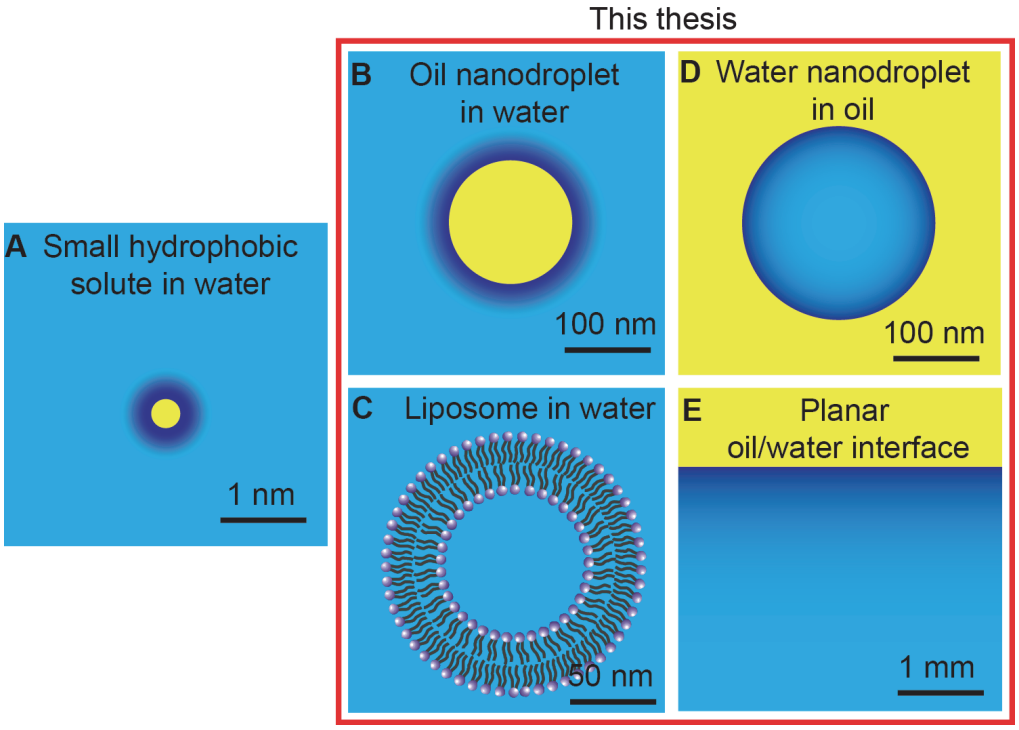

Figure 1.2. Sketch of different types of model hydrophobic systems: a hydrophobic solute dispersed in water (A), oil nanodroplet in water (B), phospholipid liposome (C), water nanodroplet in oil (D) and planar oil/water interface (E). In this thesis, the nanodroplets (both of water-in-oil and oil-in-water), liposomes and planar interfaces were studied. Scale bars indicate the characteristic size of the systems; molecules are not to scale. Oil is shown in yellow and water in blue. Dark blue indicates water molecules affected by hydrophobic groups.

In the next section of this chapter, we present currently open questions in the literature. Then we discuss the possible type of samples and techniques to study them and give a short description of second-order nonlinear scattering spectroscopy that is mainly used in this work. Finally, we provide the outline of the thesis.

1.2 Open questions

There are still many open questions concerning the relationship between the molecular structure and the chemical properties of the interfaces. Answers to these questions are relevant for many applied and fundamental problems: the development of drug delivery systems based on liposomes or water droplets, mechanisms of cell signaling, freezing of ice on hydrophobically coated surfaces, and the phase diagram of water.

1. Can we study water/air interface using optical nonlinear scattering spectroscopy, and minimize heating effects and chemical impurities which might influence studies of water/air interfaces?

2. Is the length scale relevant for the molecular structure of interfacial water? Is the molecular structure of water around a small hydrophobic solute (<1 nm), at the nanoscopic droplet interface (~100 nm) or at the macroscopic water/oil interface the same? Does the curvature of the surface play a role here?

3. How to investigate properties of water droplets dispersed in a non-polar solvent? Can we develop techniques to study droplets resembling real life systems?

4. Does water structure and hydration play a role in organization and self-assembly of cell membranes?

1.3 How to probe hydrophobic interactions?

Hydrophobic interactions can be probed using samples with different characteristic length scale: from hydrophobic solutes (water around dissolved hydrophobic molecule or non-polar group of a molecule), nanoscaled interfaces (e.g. water ordering around oil nanodroplet or in the water nanodroplet), or on macroscopic level (at planar oil/water interfaces or surfaces of crystals coated with hydrophobic layers). Figure 1.2 shows examples of such structures. As all these samples have different chemical properties, they can be studied with different techniques. Below we briefly describe the techniques and some findings reported in the recent literature.

1.3.1 Studies of hydrophobic solutes

When a hydrophobic solute is dissolved in water, it certainly affects water structure and H-bonds around it. But do hydrophobic solutes increase or decrease water ordering around them? Are they structure-making or structure-breaking [13]? This is a long standing question and different results have been obtained by different research groups.

Historically, the explanation of hydrophobicity was given using the concept of tiny “icebergs” of water near small hydrophobic solutes [14]. The term “iceberg” means here the enhancement of water H-bonds around the solute (e.g. larger number of H-bonds and/or an increase of their strength). This interpretation is derived from classical thermodynamic measurements performed in the 1940s [14] and 1960s [15]. Later on, this explanation was questioned: studies using techniques such as X-ray spectroscopy [16] or neutron diffraction [17, 18] reported that water around hydrophobic solutes is not different from the bulk. Besides, small hydrophobic solutes were studied with vibrational spectroscopy methods. In the group of Prof. Dor Ben-Amotz, the combination of Raman spectroscopy with multivariate curve resolution analysis (Raman-MCR) was developed [19]. Then

this technique was applied to study the solvation shell structure of hydrophobic groups of alcohols by analyzing spectra of water around these groups [20]. However, the results about hydrophobic hydration were obtained using hydrophilic samples (alcohols) which are completely mixable with water. The reason for this is that hydrophobic molecules have a very low solubility in water and one needs to increase the concentration of the solutes to measure the weak Raman signal. IR spectroscopy can also be used to study solvation shell of solutes [21, 22]. Grdadolnik et al. [22] used a more sophisticated way: they measured IR spectra of water with dissolved gases at high pressure. It helped to increase the concentration of the solutes. Both groups [20, 22] confirmed the classical view of the hydrophobic hydration.

The characteristic size is an important parameter in the hydrophobic interactions [23]. Planar interfaces and small hydrophobic solutes are hydrated differently. Thus there must be a cross-over between the behavior of the small hydrophobic solutes and planar hydrophobic interfaces. Such characteristic length scale was estimated by Chandler as 1 nm [23, 24]. Solutes smaller than this size are expected to increase water ordering around them, whereas larger ones destroy the ordering.

1.3.2 Studies of planar interfaces and droplets

Liquid/liquid interfaces are perhaps the most difficult interfaces for experimental studies. Many surface sensitive techniques require a vacuum to probe the first interfacial molecules since they use electrons or ions (such as X-ray photoelectron spectroscopy) and thus are not compatible with liquid/liquid interfaces, need a crystalline order (X-ray reflectivity and scattering) or have too large penetration depth (Attenuated Total Reflectance IR absorption). Optical spectroscopies do not require vacuum and thus can be applied to study liquid/liquid interfaces. The field of nonlinear optics quickly established itself after the invention of the first laser. Later on, with the improvement of high power short pulse laser sources, vibrationally sensitive sum frequency generation spectroscopy was developed [25, 26]. Due to specific selection rules the vibration sensitive sum frequency generation (SFG) spectroscopy [27-31] probes to the interfacial structure and charge of 2-3 monolayers below and above the interface. With SFG spectroscopy vibrational modes active both in Raman and IR absorption spectra can be studied. Thus SFG and its simplified version, second harmonic generation (SHG) became very common tools for surface studies. Nevertheless, the current understanding of the molecular structure of water at hydrophobic interfaces is controversial and limited due to the difficulties associated with probing it. We provide below some details of the current state-of-the-art in the field, highlighting aspects that are not well understood as well as controversy and challenges.

Hydrophobic droplets, particles, or gas bubbles have been repeatedly measured to have a negative charge [9, 10]. The origin of this charge is still debated [12, 32-37]. The ζ-potential of oil

droplets and air bubbles decreases with the increase of pH. The most intuitive and long standing explanation for the negative charge of the hydrophobic/water interface is that OH^- ions from the water autoprotolysis reaction preferentially adsorb in the surface region (e.g. Refs. [37, 38]). The surface tension of the air/water interface (which is considered as a hydrophobic liquid/water interface) increases with increasing pH, apparently in contradiction with the favorable adsorption of small ions. The interpretation of this data suggests that OH^- is excluded from the interface [39]. Thus electrophoretic mobility data and surface tension data are in disagreement. To resolve this problem many spectroscopic experiments have been performed recently. A search for spectroscopic signatures that are directly attributable to OH^- ions in the interfacial region has been performed. OH^- could be detected in the interfacial region by means of its 2p valence excitation, using X-ray photoelectron spectroscopy (XPS) on a liquid jet. XPS is interface-sensitive over a length scale of a few nm. Using this method, OH^- ions were, however, not detected in the surface region [40]. Another direct route is the detection of a resonant second harmonic generation (SHG) signal of the optical charge transfer-to-solvent transition of interfacial OH^- ions at a wave-length of 190 nm [41, 42]. Petersen et al. [42] did not detect any preferential adsorption of OH^- ions at the air/water interface. Alternatively, the OH/OD stretch vibration of OH^-/OD^- ions could be detected [43, 44]. However, the SF spectra do not change with increasing pH and do not contain any evidence for the presence of interfacial hydroxyl ions [12]. Taking into account that the electrokinetic mobility increases drastically with pH, a charge transfer scenario is most in accord with the present data to explain the negative charge at the water/oil interface [12]. However, since most experiments compare structures measured on planar surfaces to mobility measurements of droplets <100 nm, it could be a matter of comparing apples with oranges.

But even when apples are compared to apples problems may arise. Data obtained with the same technique sometimes give different results: Oil/water interface SFG spectra from the Richmond group show a weakening of H-bonds [45] while SFG data from the same interface taken by the Bakker group [46, 47] show an enhancement of H-bonds (see Figure 1.3). The results reported in Ref. [46, 47] show that the intensity of the broad water band increases drastically when going from air/D_2O to the hexane/D_2O or heptane/D_2O interface and decreases when the temperature is raised. The authors suggested that the original experiments from the Richmond lab were influenced by heating effects from the IR laser pulses that interact with the bulk water. This indeed occurs in many surface film experiments on H_2O (and in a much lesser extent on D_2O) [48]. In addition, the oil film on water might be non-uniform and this may affect SFG results: The microscopy image of a pentane film on water [49] that shows different film thicknesses, with rafts, clefts, and air exposed water pockets is very insightful.

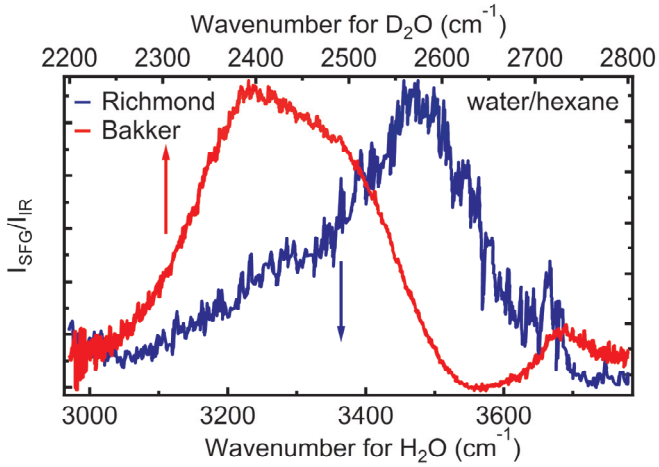

Figure 1.3. SFG spectra of water/hexane interface reported by 2 different groups: Bakker (red) [47] and Richmond (blue) [45]. The scaling of D_2O to H_2O wavenumbers was done using a scale factor of 1.35 [50]. The SFG spectra from the water/air interface using H_2O and D_2O from these two groups are similar.

Another contradiction is concerning the shape and pH dependence of octadecyltrichlorosilane (OTS) / water interface SFG spectra measured by Tian et al. [51] and Ye et al. [52]. In [51] the reported spectral changes are attributed to originate from effects induced by the adsorption of hydroxide ions, whereas in [52] the observed spectral changes are interpreted as coming from the interplay of water molecules at the OTS/water interface and the water molecules between quartz and OTS layer . Furthermore, there is an ongoing debate in the literature concerning the analysis of water/air SFG spectra with different interpretations initially proposed by Shen [53], Bonn [54] and Skinner [55]. In some experiments, the impurity of the interfaces [12], thermal effects [48] or inherent inhomogeneity or preparation of the interface [56] may alter the conclusions. In addition to the large amount of the experimental work, many theoretical efforts have been made to describe hydrophobic phenomena, including works of Stillinger employing the concept of the vapor-like layer between hydrophobic surface and bulk water [57] and following papers by Pratt and Chandler [11, 23, 24, 58, 59].

Therefore, new avenues are needed to probe liquid hydrophobic interfaces. Ideally these methods use stable reproducible interfaces, with less sensitivity to experimental artefacts and influences.

1.4 Nonlinear spectroscopy techniques

1.4.1 Sum frequency and second harmonic generation

In this thesis, we use second-order nonlinear spectroscopy to obtain molecular level information of the interfaces. The first second harmonic generation experiment was reported in 1961 [60] shortly after the invention of a ruby laser in 1960. Later the theory of the surface second harmonic generation was developed [61]. The first studies of monolayers using second harmonic generation were

performed in 1969 [62]. The surface sensitive sum-frequency spectroscopy was developed in 1987 [25, 26]. We give below a brief description of second harmonic and sum frequency generation.

The polarization ***P*** can be expanded in a power series around ***E***

$$\boldsymbol{P} = \boldsymbol{P}(\boldsymbol{E}^{(1)}) + \boldsymbol{P}(\boldsymbol{E}^{(2)}) + \boldsymbol{P}(\boldsymbol{E}^{(3)}) + \ldots$$

where second and higher order terms are significant if the driving electric field ***E*** is strong enough. Refraction, reflection, and linear scattering are driven by the first term in this series. The second term can be used to describe second order nonlinear effects, such as Second Harmonic Generation (SHG), Sum Frequency Generation (SFG) or Difference Frequency Generation (DFG). Figure 1.4 shows energy diagrams for SHG and SFG processes.

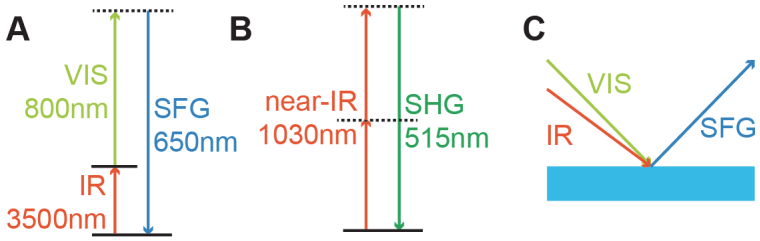

Figure 1.4. Energy diagram for SFG (A) and SHG (B) and the scheme of the experimental geometry for the reflection SFG experiment (C).

Because of symmetry considerations, in the electric dipole approximation [29], second harmonic light can be generated only when inversion symmetry is broken. There are two important consequences of this rule. First, only crystals with no inversion symmetry are used to generate efficiently SHG, SFG or DFG beams. Such crystals are used in optical parametric amplifiers to change the wavelength of the laser pulse. Second, in ideal liquids, an average inversion symmetry is present and no second harmonic generation can be observed. Nevertheless, at the interface of two centrosymmetric materials inversion symmetry is broken, thus second harmonic or sum frequency light can be generated. At a planar interface, this light may be transmitted or reflected in the direction given by the sum of wave vectors of incoming beams (the phase matching direction).

The polarization of the sum frequency light can be written as

$$P_i^{(2)}(\omega_1 + \omega_2) = \chi_{ijk}^{(2)} E_j(\omega_1) E_k(\omega_2)$$

where, generally speaking, $\chi^{(2)}$ is the second order tensor containing 27 elements. For an isotropic surface, the number of non-zero components is 7 and only 4 are independent [29].

The second order susceptibility $\chi^{(2)}$ depends on the molecular hyperpolarizability $\beta^{(2)}$, the density of molecules at the interface and their orientational distribution [31]. On resonance, for the case of infrared-visible SFG (or vibrational sensitive SFG) the strength of the second order hyperpolarizability $\beta^{(2)}$ is given by

$$\beta^{(2)} = \beta_{NR}^{(2)} + \sum_q \frac{\beta^q}{\omega_{IR} - \omega_q + i\gamma_q}$$

where the first term $\beta_{NR}^{(2)}$ represents non-resonant contributions (small for dielectric interfaces not in electronic resonance), β^q, ω_q and γ_q are the sum frequency factor tensor, resonant frequency and damping constant of the *q*th molecular vibrational mode, respectively. The tensor elements of β^q are related to the IR and Raman properties of the vibrational mode

$$\beta_{ijk}^q \propto \frac{\delta\alpha_{ij}}{\delta Q_q}\frac{\delta\mu_k}{\delta Q_q}$$

in which $\frac{\delta\alpha_{ij}}{\delta Q_q}$ and $\frac{\delta\alpha_{ij}}{\delta Q_q}$ are the partial derivatives of the Raman polarizability tensor and the IR transition dipole moment of the *q*th vibrational mode; and Q_q is the normal coordinate of the same mode. As a result, any non-zero sum frequency vibrational mode has to be both IR and Raman active. In other words, the inversion symmetry has to be broken at both molecular and interfacial levels. Using different frequencies of the IR pulse and fixed frequency of the visible pulse, different vibrational modes can be probed. Therefore, sum frequency generation spectroscopy has chemical sensitivity. In addition, with selective replacement of certain H atoms with D atoms one can choose vibrational mode of interest.

The SFG or SFS experiments are performed in particular polarization combinations denoted as, for example, SSP where P refers to the horizontally and S to the vertically polarized light (all experiments were performed in the horizontal plane). The letters are in the order of increasing wavelength of the beams: The first letter corresponds to the polarization of the SF beam, the second letter corresponds to the polarization of the VIS beam and the last letter corresponds to the polarization of IR beam. In SH experiments there are only two beams. In this case, the first letter corresponds to the polarization of SH beam and second letter corresponds to the polarization of the incoming (fundamental) beam. The SFG response is only allowed in PPP, SSP, SPS and PSS polarization combinations.

1.4.2 Sum frequency and second harmonic scattering

In this section, we provide a brief description of SFS and SHS and discuss some advantages of the scattering technique, e.g. reduced sensitivity for impurities. The SFS spectroscopy was developed in 2003 by Roke et al. [30] and used for studies of nanoparticles [30, 63], surfactants on oil droplets [64, 65], and self-assembled surfactant vesicles [66]. When visible (VIS) and infrared (IR) beams are overlapped in a suspension or in an emulsion, a second-order polarization cannot be excited from the homogeneous centrosymmetric bulk. However, at the interface of the particles, centrosymmetry is broken and the second order polarization is excited. This polarization is the source of

SF photons (SH photons if two beams are same). At the far field, they interfere and give rise to a scattering pattern. The amplitude of the sum frequency signal from a single nanoparticle is proportional to the second order polarization $\boldsymbol{P}^{(2)}$:

$$P_i^{(2)}(\theta, \omega_1 + \omega_2) = \Gamma_{ijk}^{(2)}(\theta) E_j(\omega_1) E_k(\omega_2)$$

where θ is the scattering angle with respect to the phase matching direction, and $\Gamma^{(2)}$ is the effective particle susceptibility, containing all information on the scatter and the scattering geometry. $\Gamma^{(2)}$ depends on the second order susceptibility $\chi^{(2)}$ and the scattering form factor functions [67]. Figure 1.5 A shows a scheme of the SFS experiment. The selection rules for small spherical particles in SFS are similar to the selection rules for planar SFG: the SFS is allowed in PPP, SSP, SPS and PSS polarization combinations [68]. For non-spherical particles these selection rules are not valid and the SFS response can be observed in all polarization combinations [69, 70]. In the small particle limit, SFS intensity is related to the radius of a single particle *R* as:

$$I \propto R^6$$

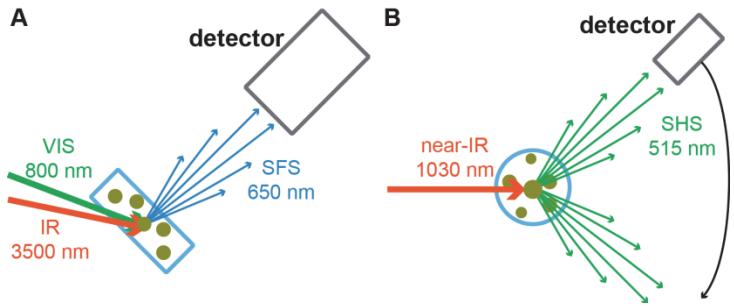

Figure 1.5. Scheme of the experimental geometry for the SFS (A) and SHS (B) for colloidal particles. SFS experiments were performed in the fixed angle geometry while SHS experiments were performed using the photomultiplier tube mounted on the rotation stage.

The SF scattering pattern for emulsions with droplet radii from 100 to 200 nm has a maximum intensity for scattering angle around 55° [71]. In this work, the detector was set to this position to measure the SFS spectra. Indeed, at low densities of particles, the SFS intensity is proportional to the number of particles in the probed volume. At higher concentrations, multiple scattering may play a role. The optimal concentration of droplets was discussed in [72].

Sum frequency and second harmonic generation are similar phenomena and can be described using the same mathematical basis. The main difference is that in the SHS the incoming beams are degenerate. A scheme of the SHS experiment is shown in Figure 1.5 B. In a non-resonant second harmonic generation experiment, the chemical sensitivity is less pronounced because the SHS signal depends only on the strength of the non-resonant molecular hyperpolarizability, the amount of molecules and their ordering [73]. Non-resonant SHS experiments are typically performed with the fundamental beam wavelength of ~ 1 μm. In this case, when dipolar water is in

contact with the organic phase, the SHS signal originates from water molecules (see for example Ref. [73-75]). Organic molecules, found in the studied samples, such as alkanes, surfactants or phospholipids typically do not have strong molecular hyperpolarizability values, because of the absence of dipole moments. The concentration of these molecules is also much smaller than that of water.

In this work, second harmonic scattering data were recorded at different detection angles, e.g. angular scattering patterns were measured. These patterns can be simulated using the nonlinear light scattering theory which can provide the absolute value of surface potential using molecular hyperpolarizabilities of water [76], dielectric constant, radii and number density of particles. The theoretical basis of SHS and SFS is described in a number of papers [30, 67, 68, 71, 73, 77, 78]. With this technique, a very high degree of counterion condensation on charged membranes in water was found [75].

SHS and SFS can thus be used to measure the molecular interfacial structure from particles and droplets and facilitating our fundamental understanding of hydrophobicity at nanoscale. In addition small sample volumes (60 µL) can be used and effects of impurities can be drastically reduced, as explained below.

1.4.3 Impurities at planar interfaces and in nanodroplets

One of the main advantages of scattering techniques is that they are less sensitive to impurities because of the much larger surface-to-volume ratio of nanodroplets compare with a planar surface [12]. Indeed, the presence of chemical impurities at the interface, caused by the inherent purity restrictions to available chemicals, can be a source of the signal. For example, a 1 mL 1 mM solution of a 99.5 % pure chemical may contain enough impurity molecules to cover 15-30 cm^2 of surface area (assuming a worst case scenario that all impurities are surface active and that the molecular area is 50 -100 $Å^2$). Typical planar or reflection mode SFG measurements have a probing area of ~1 × 10^{-2} mm^2, and if they are performed in (e.g.) a Langmuir trough, the liquid volume and surface area are respectively 18 – 336 mL and 150 – 841 cm^2 [79]. Under worst case scenario conditions the Langmuir trough surface will be fully covered with impurities. To be absolutely sure that impurities do not cover more than 1 % of the available surface area, chemicals with a purity of at least 99.9995 % are therefore needed, which are not always available. Table 1.1 summarizes the result of this simple computation. This restriction is much reduced in nonlinear light scattering experiments performed on a nanodroplet system: A nanodroplet dispersion can be prepared in-situ using only a small volumes of chemicals. A 4 mL 4 vol% nanodroplet dispersion of droplets with a radius of 100 nm contains ~12000 cm^2 of surface area. For the above worst case scenario, if this solution contains 1 mM of a 99.5 % pure chemical, only 1 % of the available surface area can at most be covered with impurity molecules, even if all impurity molecules adsorb on the surface (i.e.

irrespective of the chemical equilibrium). Therefore, SFS (SHS) is significantly less sensitive to the amount of impurities than conventional SFG (SHG) using planar interfaces.

Parameters	**Small Langmuir trough**	**Nanodroplets**
Liquid Volume (mL)	18	4
Total interfacial area (cm^2)	150	11936
Droplet radius (nm)	-	100
Volume fraction of droplets (%)	-	1
Purity:	**Interfacial Coverage of Impurity**	
	Small Langmuir trough	**Nanodroplets**
99.5 %	> 100 % (360 %)	1 %
99.95 %	36 %	0.1 %
99.995 %	3.6 %	0.01 %
99.9995 %	0.36 %	0.001 %

Table 1.1. Available interfacial area, volume, and maximum possible interfacial coverage for a hypothetical impurity molecule with a projected surface of 1 nm^2 at the surface of a small Langmuir trough and a nanodroplet system.

1.5 This thesis

The remainder of this thesis is organized as follows:

In this thesis, in Chapter 2, we first describe methods, sum frequency and second harmonic scattering spectroscopy, as well as dynamic light scattering and ζ-potential measurements. Then we provide experimental details of SHS, SFS, and describe the designed temperature cell for the SFS measurements and generation of the broad-band IR pulse. We also provide some details of the data analysis used in the next chapters.

In Chapter 3 we describe a way to measure the SHG and SFG data from a liquid/air interface using a liquid jet. This experimental approach allows for an enhancement of the signal as well as minimizing heating effects and constantly refreshing the surface.

In Chapter 4 we elucidate the interfacial water structure of water droplets dispersed in a hydrophobic solvent. We show that water at the surface of a nanoscale droplet is more ordered than at the planar interface made of the same chemicals. From a comparison of spectra of supercooled and frozen droplets, we conclude that this finding is specific for liquid water.

In Chapter 5 we further continue and extend our study to the charged surface of water droplets dispersed in CCl_4. We determine the surface potential, ion pairing in non-ionic solvent and surface structure of water. Formation of micelles at the surface of water droplets is discussed.

In Chapter 6 we show the presence of lipid asymmetry in liposomes composed of certain binary mixtures of lipids and importance of water-mediated interactions for this process. We quantify lipid asymmetry and propose a possible underlying mechanism based on the H-bonding between the headgroups of the neighboring lipids.

Finally, we conclude with the summary and outlook for future developments. Each result chapter of this thesis is based on a separate publication/manuscript. A detailed list of publications is given at the end of the thesis.

References

1. McNaught, A.D.W., A., *IUPAC. Compendium of Chemical Terminology, 2nd ed. (the "Gold Book").*1997, Oxford: Blackwell Scientific Publications.
2. Ball, P., *Water as an active constituent in cell biology.* Chem. Rev., 2008. **108**(1): p. 74-108.
3. Israelachvili, J.N., *Intermolecular and surface forces* 1991: Academic Press; New York.
4. Jung, Y.S. and R.A. Marcus, *On the theory of organic catalysis on water.* J. Am. Chem. Soc., 2007. **129**(17): p. 5492-5502.
5. Nilsson, A. and L.G.M. Pettersson, *The structural origin of anomalous properties of liquid water.* 2015. **6**: p. 8998.
6. Wernet, P., et al., *The Structure of the First Coordination Shell in Liquid Water.* Science, 2004. **304**(5673): p. 995-999.
7. Chen, Y., et al., *Electrolytes induce long-range orientational order and free energy changes in the H-bond network of bulk water.* Science Advances, 2016. **2**(4).
8. Perakis, F., et al., *Vibrational Spectroscopy and Dynamics of Water.* Chem. Rev., 2016. **116**(13): p. 7590-7607.
9. Marinova, K.G., et al., *Charging of Oil−Water Interfaces Due to Spontaneous Adsorption of Hydroxyl Ions.* Langmuir, 1996. **12**(8): p. 2045-2051.
10. Graciaa, A., et al., *The ζ-Potential of Gas Bubbles.* J. Colloid Interface Sci., 1995. **172**(1): p. 131-136.
11. Pratt, L.R. and A. Pohorille, *Hydrophobic effects and modeling of biophysical aqueous solution interfaces.* Chem. Rev., 2002. **102**(8): p. 2671-2691.
12. Samson, J.-S., et al., *Sum frequency spectroscopy of the hydrophobic nanodroplet/water interface: Absence of hydroxyl ion and dangling OH bond signatures.* Chem. Phys. Lett., 2014. **615**: p. 124-131.
13. Ball, P., *Water as an Active Constituent in Cell Biology.* Chem. Rev., 2007. **108**(1): p. 74-108.
14. Frank, H.S. and M.W. Evans, *Free volume and entropy in condensed systems iii. Entropy in binary liquid mixtures; partial molal entropy in dilute solutions; structure and thermodynamics in aqueous electrolytes.* J. Chem. Phys., 1945. **13**(11): p. 507-532.
15. Glew, D.N., *Aqueous solubility and the gas-hydrates. The methane-water system.* J. Phys. Chem., 1962. **66**(4): p. 605-609.
16. Bowron, D.T., et al., *Temperature-induced disordering of the hydrophobic hydration shell of Kr and Xe.* Chem. Phys. Lett., 1998. **293**(1): p. 33-37.
17. Buchanan, P., et al., *Decreased structure on dissolving methane in water.* Chem. Phys. Lett., 2005. **415**(1): p. 89-93.

18. Koh, C.A., et al., *Water ordering around methane during hydrate formation.* J. Chem. Phys., 2000. **113**(15): p. 6390-6397.
19. Perera, P., et al., *Solute-Induced Perturbations of Solvent-Shell Molecules Observed Using Multivariate Raman Curve Resolution.* J. Am. Chem. Soc., 2008. **130**(14): p. 4576-4577.
20. Davis, J.G., et al., *Water structural transformation at molecular hydrophobic interfaces.* Nature, 2012. **491**(7425): p. 582-585.
21. Sun, Y. and P.B. Petersen, *Solvation Shell Structure of Small Molecules and Proteins by IR-MCR Spectroscopy.* J, Phys. Chem. Lett., 2017. **8**(3): p. 611-614.
22. Grdadolnik, J., F. Merzel, and F. Avbelj, *Origin of hydrophobicity and enhanced water hydrogen bond strength near purely hydrophobic solutes.* Proc. Natl. Acad. Sci., 2017. **114**(2): p. 322-327.
23. Lum, K., D. Chandler, and J.D. Weeks, *Hydrophobicity at Small and Large Length Scales.* J. Phys. Chem. B, 1999. **103**(22): p. 4570-4577.
24. Chandler, D., *Interfaces and the driving force of hydrophobic assembly.* Nature, 2005. **437**(7059): p. 640-647.
25. Hunt, J.H., P. Guyot-Sionnest, and Y.R. Shen, *Observation of C-H stretch vibrations of monolayers of molecules optical sum-frequency generation.* Chem. Phys. Lett., 1987. **133**(3): p. 189-192.
26. Harris, A.L., et al., *Monolayer vibrational spectroscopy by infrared-visible sum generation at metal and semiconductor surfaces.* Chem. Phys. Lett., 1987. **141**(4): p. 350-356.
27. Raschke, M.B. and Y.R. Shen, *Nonlinear optical spectroscopy of solid interfaces.* Curr. Opin. Solid State Mater. Sci., 2004. **8**(5): p. 343-352.
28. Hopkins, A.J., C.L. McFearin, and G.L. Richmond, *Investigations of the solid–aqueous interface with vibrational sum-frequency spectroscopy.* Curr. Opin. Solid State Mater. Sci., 2005. **9**(1–2): p. 19-27.
29. Lambert, A.G., P.B. Davies, and D.J. Neivandt, *Implementing the Theory of Sum Frequency Generation Vibrational Spectroscopy: A Tutorial Review.* Appl. Spectrosc. Rev., 2005. **40**(2): p. 103-145.
30. Roke, S., et al., *Vibrational sum frequency scattering from a sub-micron suspension.* Phys. Rev. Lett., 2003. **91**: p. 258302.
31. Wang, H.-F., et al., *Quantitative spectral and orientational analysis in surface sum frequency generation vibrational spectroscopy (SFG-VS).* Int. Rev. Phys. Chem., 2005. **24**(2): p. 191-256.
32. Jena, K.C., R. Scheu, and S. Roke, *Surface impurities are not responsible for the charge on the oil/water interface: a comment.* Angew. Chem., Int. Ed., 2012. **51**(52): p. 12938-12940.
33. Roger, K. and B. Cabane, *Uncontaminated Hydrophobic/Water Interfaces Are Uncharged: A Reply.* Angew. Chem. Int. Ed., 2012. **51**(52): p. 12943-12945.

34. Roger, K. and B. Cabane, *Why Are Hydrophobic/Water Interfaces Negatively Charged?* Angew. Chem. Int. Ed., 2012. **51**(23): p. 5625-5628.
35. Fang, H., et al., *Evidence of the adsorption of hydroxide ion at hexadecane/water interface from second harmonic generation study.* RSC Advances, 2015. **5**(30): p. 23578-23585.
36. Beattie, J.K. and A. Gray-Weale, *Oil/Water Interface Charged by Hydroxide Ions and Deprotonated Fatty Acids: A Comment.* Angew. Chem. Int. Ed., 2012. **51**(52): p. 12941-12942.
37. Beattie, J.K. and A.M. Djerdjev, *The Pristine Oil/Water Interface: Surfactant-Free Hydroxide-Charged Emulsions.* Angew. Chem. Int. Ed., 2004. **43**(27): p. 3568-3571.
38. Creux, P., et al., *Strong Specific Hydroxide Ion Binding at the Pristine Oil/Water and Air/Water Interfaces.* J. Phys. Chem. B, 2009. **113**(43): p. 14146-14150.
39. Agmon, N., et al., *Protons and Hydroxide Ions in Aqueous Systems.* Chem. Rev., 2016. **116**(13): p. 7642-7672.
40. Aziz, E.F., et al., *Interaction between liquid water and hydroxide revealed by core-hole de-excitation.* Nature, 2008. **455**(7209): p. 89-91.
41. Petersen, P.B. and R.J. Saykally, *Evidence for an Enhanced Hydronium Concentration at the Liquid Water Surface.* J. Phys. Chem. B, 2005. **109**(16): p. 7976-7980.
42. Petersen, P.B. and R.J. Saykally, *Is the liquid water surface basic or acidic? Macroscopic vs. molecular-scale investigations.* Chem. Phys. Lett., 2008. **458**(4): p. 255-261.
43. Librovich, N.B., V.P. Sakun, and N.D. Sokolov, *H+ and OH− ions in aqueous solutions vibrational spectra of hydrates.* Chem. Phys., 1979. **39**(3): p. 351-366.
44. Hermansson, K., et al., *The vibrating hydroxide ion in water.* Chem. Phys. Lett., 2011. **514**(1): p. 1-15.
45. Scatena, L.F., M.G. Brown, and G.L. Richmond, *Water at Hydrophobic Surfaces: Weak Hydrogen Bonding and Strong Orientation Effects.* Science, 2001. **292**(5518): p. 908-912.
46. Strazdaite, S., J. Versluis, and H.J. Bakker, *Water orientation at hydrophobic interfaces.* J. Chem. Phys., 2015. **143**(8): p. 084708.
47. Strazdaite, S., et al., *Enhanced ordering of water at hydrophobic surfaces.* J. Chem. Phys., 2014. **140**(5): p. 054711.
48. Backus, E.H.G., et al., *Laser-Heating-Induced Displacement of Surfactants on the Water Surface.* J. Phys. Chem. B, 2012. **116**(9): p. 2703-2712.
49. Del Cerro, C. and G.J. Jameson, *The behavior of pentane, hexane, and heptane on water.* J. Colloid Interface Sci., 1980. **78**(2): p. 362-375.
50. Bonn, M., Y. Nagata, and E.H.G. Backus, *Molecular structure and dynamics of water at the water–air interface studied with surface-specific vibrational spectroscopy.* Angew. Chem. Int. Ed., 2015. **54**(19): p. 5560-5576.

51. Tian, C.S. and Y.R. Shen, *Structure and charging of hydrophobic material/water interfaces studied by phase-sensitive sum-frequency vibrational spectroscopy.* Proc. Natl. Acad. Sci., 2009. **106**(36): p. 15148-15153.
52. Ye, S., S. Nihonyanagi, and K. Uosaki, *Sum frequency generation (SFG) study of the pH-dependent water structure on a fused quartz surface modified by an octadecyltrichlorosilane (OTS) monolayer.* Phys. Chem. Chem. Phys., 2001. **3**(16): p. 3463-3469.
53. Du, Q., et al., *Vibrational spectroscopy of water at the vapor/water interface.* Phys. Rev. Lett., 1993. **70**(15): p. 2313-2316.
54. Sovago, M., et al., *Vibrational Response of Hydrogen-Bonded Interfacial Water is Dominated by Intramolecular Coupling.* Phys. Rev. Lett., 2008. **100**(17): p. 173901.
55. Auer, B.M. and J.L. Skinner, *Vibrational Sum-Frequency Spectroscopy of the Water Liquid/Vapor Interface†.* J. Phys. Chem. B, 2009. **113**(13): p. 4125-4130.
56. Tyrode, E. and J.F.D. Liljeblad, *Water Structure Next to Ordered and Disordered Hydrophobic Silane Monolayers: A Vibrational Sum Frequency Spectroscopy Study.* J. Phys. Chem. C, 2013. **117**(4): p. 1780-1790.
57. Stillinger, F.H., *Structure in aqueous solutions of nonpolar solutes from the standpoint of scaled-particle theory.* J. Solution Chem., 1973. **2**(2): p. 141-158.
58. Pratt, L.R. and D. Chandler, *Theory of the hydrophobic effect* J. Chem. Phys., 1977. **67**(8): p. 3683-3704.
59. Ashbaugh, H.S. and L.R. Pratt, *Colloquium.* Reviews of Modern Physics, 2006. **78**(1): p. 159-178.
60. Franken, P.A., et al., *Generation of Optical Harmonics.* Phys. Rev. Lett., 1961. **7**(4): p. 118-119.
61. Bloembergen, N., et al., *Optical Second-Harmonic Generation in Reflection from Media with Inversion Symmetry.* Phys. Rev., 1968. **174**(3): p. 813-822.
62. Brown, F. and M. Matsuoka, *Effect of Adsorbed Surface Layers on Second-Harmonic Light from Silver.* Phys. Rev., 1969. **185**(3): p. 985-987.
63. de Aguiar, H.B., A.G.F. de Beer, and S. Roke, *The Presence of Ultralow Densities of Nanocrystallites in Amorphous Poly(lactic acid) Microspheres.* J. Phys. Chem. B, 2013. **117**(29): p. 8906-8910.
64. de Aguiar, H.B., et al., *Surface structure of SDS Surfactant and oil at the oil-in-water droplet liquid/liquid interface: A manifestation of a non-equilibrium surface state.* J Phys Chem B, 2011. **115**: p. 2970-2978.
65. Aguiar, H.B.d., et al., *The Interfacial Tension of Nanoscopic Oil Droplets in Water Is Hardly Affected by SDS Surfactant.* J. Am. Chem. Soc., 2010. **132**(7): p. 2122-2123.
66. Strader, M.L., et al., *Label-free spectroscopic detection of vesicles in water using vibrational sum frequency scattering.* Soft Matter, 2011. **7**(10): p. 4959-4963.

67. de Beer, A.G.F., R.K. Campen, and S. Roke, *Separating surface structure and surface charge with second-harmonic and sum-frequency scattering.* Phys. Rev. B, 2010. **82**(23): p. 235431.
68. de Beer, A.G.F. and S. Roke, *Obtaining molecular orientation from second harmonic and sum frequency scattering experiments in water: Angular distribution and polarization dependence.* J. Chem. Phys., 2010. **132**(23): p. 234702.
69. de Beer, A.G.F., S. Roke, and J.I. Dadap, *Theory of optical second-harmonic and sum-frequency scattering from arbitrarily shaped particles.* J. Opt. Soc. Am. B, 2011. **28**(6): p. 1374-1384.
70. Smit, W.J., et al., *Freezing effects of oil-in-water emulsions studied by sum-frequency scattering spectroscopy.* J. Chem. Phys., 2016. **145**(4): p. 044706.
71. de Beer, A.G.F. and S. Roke, *Nonlinear Mie theory for second-harmonic and sum-frequency scattering.* Phys. Rev. B, 2009. **79**(15): p. 155420.
72. de Aguiar, H.B., J.-S. Samson, and S. Roke, *Probing nanoscopic droplet interfaces in aqueous solution with vibrational sum-frequency scattering: A study of the effects of path length, droplet density and pulse energy.* Chem. Phys. Lett., 2011. **512**(1–3): p. 76-80.
73. Gonella, G., et al., *Second Harmonic and Sum-Frequency Generation from Aqueous Interfaces Is Modulated by Interference.* The Journal of Physical Chemistry C, 2016. **120**(17): p. 9165-9173.
74. Schürer, B., et al., *Probing colloidal interfaces by angle-resolved second harmonic light scattering.* Phys. Rev. B: Condens. Matter, 2010. **82**(24): p. 241404.
75. Lütgebaucks, C., C. Macias-Romero, and S. Roke, *Characterization of the interface of binary mixed DOPC:DOPS liposomes in water: The impact of charge condensation.* J. Chem. Phys., 2017. **146**(4): p. 044701.
76. Gubskaya, A.V. and P.G. Kusalik, *The multipole polarizabilities and hyperpolarizabilities of the water molecule in liquid state: an ab initio study.* Mol. Phys., 2001. **99**(13): p. 1107-1120.
77. Dadap, J.I., J. Shan, and T.F. Heinz, *Theory of optical second-harmonic generation from a sphere of centrosymmetric material: small-particle limit.* J. Opt. Soc. Am. B, 2004. **21**(7): p. 1328-1347.
78. Dadap, J.I., et al., *Second-Harmonic Rayleigh Scattering from a Sphere of Centrosymmetric Material.* Phys. Rev. Lett., 1999. **83**(20): p. 4045-4048.
79. http://www.biolinscientific.com/product/langmuir-troughs-langmuir-blodgett-troughs/.

Chapter 2: Methods and experimental details

This chapter aims at providing the reader with background information about the employed methods including sum frequency and second harmonic generation and scattering, dynamic light scattering and ζ-potential measurements. The experimental details and some details of the analysis are given.

2.1 Theoretical background

Here we briefly describe a theoretical basis of sum frequency and second harmonic generation and scattering spectroscopy. More details about nonlinear optics are given in the book [1] and a detailed review of sum frequency generation is given in, for example, [2]. Then, we describe dynamic light scattering [3] and ζ-potential measurements [4] used to characterize emulsions and liposomes. Finally, we provide experimental details of the used methods.

2.1.1 Sum frequency scattering

In this section, we describe the relation between the molecular properties (molecular hyperpolarizability $\boldsymbol{\beta}^{(2)}$) and observed sum frequency scattering intensity, which was first reported by Roke et al. [5] and a more detailed description was given in [6]. The geometry and coordinate systems for nonlinear light scattering are shown in Figure 2.1.

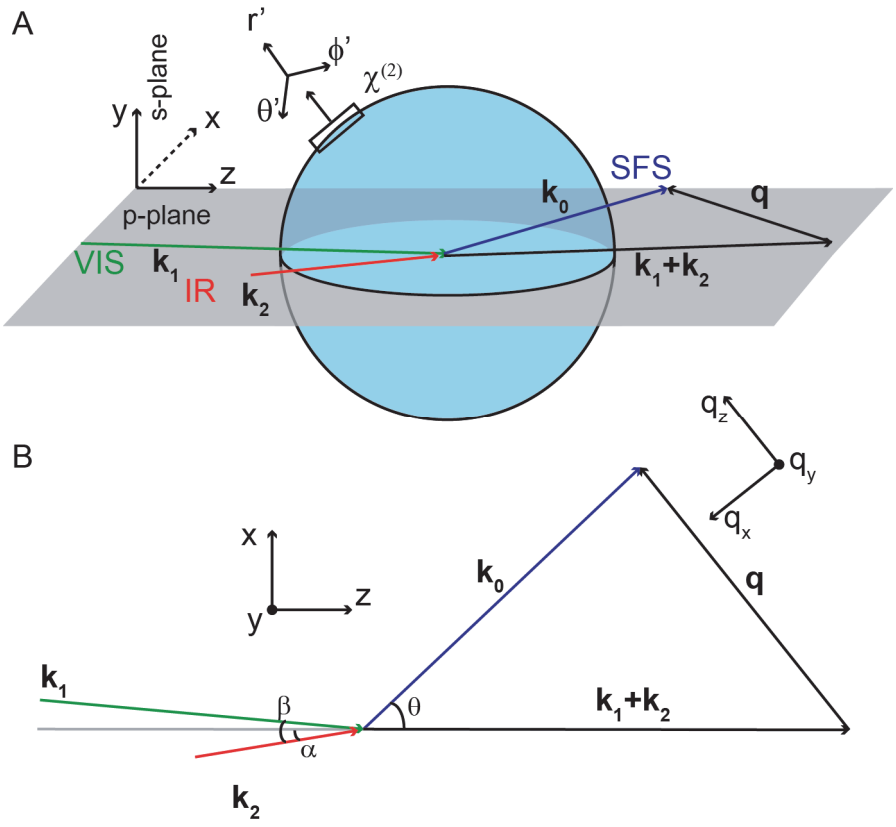

Figure 2.1. A: The geometry of an SHS/SFS experiment. Incoming visible (VIS, $\mathbf{k_1}$) and IR ($\mathbf{k_2}$) beams generate SFS ($\mathbf{k_0}$) scattered light because of the presence of a non-zero surface susceptibility $\chi^{(2)}$. The scattering wavevector **q** is defined as the difference between $\mathbf{k}_0$ and $\mathbf{k}_1$+$\mathbf{k}_2$. The external (x,y,z) coordinate system and surface coordinate systems (r',θ',ϕ') are shown. B: Top view on the horizontal scattering plane. The scattering angle and opening angles are θ, α, and β, respectively. The q coordinate system is also shown.

In an NLS experiment θ is the scattering angle, which is the angle between the k vector of the scattered (detected) light (k_0) and the sum of the incoming k vectors (k_1+k_2). The opening angles α and β are defined as shown in Figure 2.1. All angles correspond to counterclockwise rotations. In the

SHS experiments the geometry is the same. For collinear SHS there are two wave vectors, k_1 (incoming along z) and outgoing k_0 (same as for nonlinear scattering). Thus in this case the opening angles are zero (α=0 and β =0).

The principle equations for the emitted *E*-field at a distance r_0 from the particle and the effective susceptibility for second-order scattering in SI units are:

$$E_0(r_0,\omega_0) = \frac{ick_0^3}{2\pi|\hat{r}||\hat{l}|}\frac{e^{ik_0r_0}}{r_0}E_1E_2\sum_{a_0a_1a_2}\Gamma^{(2)}_{a_0a_1a_2}(\omega_0)\prod_{i=0}^{2}(\boldsymbol{q}_{a_i}\cdot\boldsymbol{u}_{i,l}) \tag{2.1}$$

$$\Gamma^{(2)}_{a_0a_1a_2}(\omega_0) = \sum_{c_0c_1c_2}\int \; d\boldsymbol{r}'^3\left\{\chi^{(2)}_{c_0c_1c_2}(\omega_0)\delta(|\boldsymbol{r}'|-R)e^{-i\boldsymbol{q}\cdot\boldsymbol{r}'}\prod_{i=0}^{2}(\boldsymbol{e}_{c_i}\cdot\boldsymbol{q}_{a_i})\right\}, \tag{2.2}$$

where $|\hat{l}|$and $|\hat{r}|$ are unit current and distances, respectively. The coordinates a_i represent the axes system of $q/\Gamma^{(2)}$, and c_i represent the coordinates of the particle surface. For a spherical particle we chose spherical coordinates (r', θ', ϕ') which have the range: $r' = [0,R]; \theta' = [0,\pi]; \phi' = [0,2\pi]$ and $d\boldsymbol{r}'^3 = r'^2dr'\sin\theta' d\theta' d\phi'$. The index *l* represents the polarization directions of all beams and can take value of P or S. The beam are indicated with the index *i* which numerical values 0,1,2 correspond to SFG, VIS and IR beams in case of the SFS experiment.

The scattering wave vector **q** is defined as:

$$\mathbf{q} = \mathbf{k_0} - (\mathbf{k_1} + \mathbf{k_2}) \text{ and } q(\theta) = |\boldsymbol{q}| = 2k_0\sin(\theta/2)$$

The out of plane scattering is described in detail in Ref. [7]. For in-plane scattering the direction of the k-vectors are defined as follows:

$$\boldsymbol{k}_0 = k_0(\sin\theta\,, 0, \cos\theta)$$

$$\boldsymbol{k}_1 = k_1(-\sin(\beta-\alpha)\,, 0, \cos(\beta-\alpha))$$

$$\boldsymbol{k}_2 = k_2(\sin(\alpha)\,, 0, \cos(\alpha))$$

$$\boldsymbol{k}_1 + \boldsymbol{k}_2 = |\boldsymbol{k}_1 + \boldsymbol{k}_2|(0,0,1)$$

For in-plane scattering the unit polarization vectors of the scattered and incoming beams are given as follows:

$$\boldsymbol{u}_{0,p} = (\cos\theta\,, 0, -\sin\theta)$$

$$\boldsymbol{u}_{1,p} = (\cos(\beta-\alpha)\,, 0, \sin(\beta-\alpha))$$

$$\boldsymbol{u}_{2,p} = (\cos(\alpha)\,, 0, -\sin(\alpha))$$

$$\boldsymbol{u}_{0,s} = \boldsymbol{u}_{1,s} = \boldsymbol{u}_{2,s} = (0,1,0)$$

Below we continue the calculation for spherical particles. Non-spherical particles are described in Ref. [8]. For scattering from a spherical particle, the axis system around q is a rotated Cartesian coordinate system. This is needed in order to evaluate the integral in (2.2) analytically.

$$\boldsymbol{q}_x = (-\sin\theta/2\,, 0, -\cos(\theta/2))$$

$$\boldsymbol{q}_y = (0,1,0)$$

$$\boldsymbol{q}_z = (\cos(\theta/2)\,, 0, -\sin\theta/2)$$

which is the same as $(-e_z, e_y, e_x)$ and then rotated over an angle θ/2

The spherical coordinate system (r', θ', ϕ') is defined with its polar axis along q_z, so that we can write for the coordinates:

$$\boldsymbol{e}_{\boldsymbol{r'}} = \sin(\theta')\cos(\phi')\boldsymbol{q}_{\boldsymbol{x}} + \sin(\theta')\sin(\phi')\,\boldsymbol{q}_{\boldsymbol{y}} + \cos(\theta')\,\boldsymbol{q}_{\boldsymbol{z}}$$

$$\boldsymbol{e}_{\boldsymbol{\theta'}} = \cos(\theta')\cos(\phi')\boldsymbol{q}_{\boldsymbol{x}} + \cos(\theta')\sin(\phi')\,\boldsymbol{q}_{\boldsymbol{y}} - \sin(\theta')\,\boldsymbol{q}_{\boldsymbol{z}}$$

$$\boldsymbol{e}_{\boldsymbol{\phi'}} = -\sin(\phi')\boldsymbol{q}_{\boldsymbol{x}} + cos\,(\phi')\,\boldsymbol{q}_{\boldsymbol{y}}$$

Then we can write Eqs. (2.1) and (2.2) as follows

$$E_{ppp} = C[\cos\left(\frac{\theta}{2}\right)\cos\left(\frac{\theta}{2}-\alpha\right)\cos\left(\frac{\theta}{2}-\alpha+\beta\right)\Gamma_1^{(2)} + \cos(\theta-\alpha+\beta)\,E_{ssp} + \cos(\theta-\alpha)\,E_{sps} + \cos(\beta)\,E_{pss}],$$

$$E_{ssp} = C[\cos\left(\frac{\theta}{2}-\alpha\right)\Gamma_2^{(2)}],$$

$$E_{sps} = C[\cos\left(\frac{\theta}{2}-\alpha+\beta\right)\Gamma_3^{(2)}],$$

$$E_{pss} = C[\cos\left(\frac{\theta}{2}\right)\Gamma_4^{(2)}], \qquad (2.3)$$

using $C = \frac{ick_0^3}{2\pi|\hat{r}||\hat{l}|}\frac{e^{ik_0r_0}}{r_0}$ and $\Gamma_1^{(2)} = \Gamma_{\perp\perp\perp}^{(2)} - \Gamma_{\parallel\parallel\perp}^{(2)} - \Gamma_{\parallel\perp\parallel}^{(2)} - \Gamma_{\perp\parallel\parallel}^{(2)}$, $\Gamma_2^{(2)} = \Gamma_{\parallel\parallel\perp}^{(2)}$, $\Gamma_3^{(2)} = \Gamma_{\parallel\perp\parallel}^{(2)}$, and $\Gamma_4^{(2)} = \Gamma_{\perp\parallel\parallel}^{(2)}$. The indices ∥ and ⊥ denote parallel and perpendicular directions with respect to the relevant coordinate system. In the case of scattering from a spherical particle ⊥ represents the direction parallel to q_z ∥ and ∥' are orthogonal to that (parallel to q_x and q_y).

In the Rayleigh-Gans-Debye approximation [6] we assume that the size of particles is small and the difference in refractive index between the two media is negligible. In this case the transformation from $\chi_i^{(2)}$ to $\Gamma_i^{(2)}$ is given by the matrix:

$$\begin{pmatrix}\Gamma_1^{(2)}\\ \Gamma_2^{(2)}\\ \Gamma_3^{(2)}\\ \Gamma_4^{(2)}\end{pmatrix}=\begin{pmatrix}2F_1-5F_2 & 0 & 0 & 0\\ F_2 & 2F_1 & 0 & 0\\ F_2 & 0 & 2F_1 & 0\\ F_2 & 0 & 0 & 2F_1\end{pmatrix}\begin{pmatrix}\chi_1^{(2)}\\ \chi_2^{(2)}\\ \chi_3^{(2)}\\ \chi_4^{(2)}\end{pmatrix}, \tag{2.4}$$

where $\chi_1^{(2)}=\chi_{\perp\perp\perp}^{(2)}-\chi_{\parallel\parallel\perp}^{(2)}-\chi_{\parallel\perp\parallel}^{(2)}-\chi_{\perp\parallel\parallel}^{(2)}$, $\chi_2^{(2)}=\chi_{\parallel\parallel\perp}^{(2)}$, $\chi_3^{(2)}=\chi_{\parallel\perp\parallel}^{(2)}$, and $\chi_4^{(2)}=\chi_{\perp\parallel\parallel}^{(2)}$. The form factors are:

$$F_1(qR)=2\pi R^2 i\left(\frac{\sin(qR)}{(qR)^2}-\frac{\cos(qR)}{qR}\right)$$

$$F_2(qR)=4\pi R^2 i\left(3\frac{\sin(qR)}{(qR)^4}-3\frac{\cos(qR)}{(qR)^3}-\frac{\sin(qR)}{(qR)^2}\right) \tag{2.5}$$

where R is the radius of the spherical particle. These equations have to be modified in the presence of an electric double layer surrounding the particle [9]. This and the case where interference between the interfacial responses from the inner part of the droplet and the media surrounding the droplet is relevant are described in Chapter 5.

The surface susceptibility $\boldsymbol{\chi}^{(2)}$ is derived from the molecular hyperpolarizability $\boldsymbol{\beta}^{(2)}$ provided that the interface is azimuthally isotropic and non-chiral. We also average here over the twist angle (which is valid for simple symmetric molecules), the formula for a non-averaged twist angle is given in Section 6.2.3. The equation for $\boldsymbol{\chi}^{(2)}$ can be written similarly as follows:

$$\begin{pmatrix}\chi_1^{(2)}\\ \chi_2^{(2)}\\ \chi_3^{(2)}\\ \chi_4^{(2)}\end{pmatrix}=\frac{N_s\langle\cos\phi\rangle}{2}\begin{pmatrix}5D-3 & 0 & 0 & 0\\ 1-D & 2 & 0 & 0\\ 1-D & 0 & 2 & 0\\ 1-D & 0 & 0 & 2\end{pmatrix}\begin{pmatrix}\beta_1^{(2)}\\ \beta_2^{(2)}\\ \beta_3^{(2)}\\ \beta_4^{(2)}\end{pmatrix}, \tag{2.6}$$

in which $\beta_1^{(2)}=\beta_{ccc}^{(2)}-\beta_2^{(2)}-\beta_3^{(2)}-\beta_4^{(2)}$, $\beta_2^{(2)}=\left(\beta_{aac}^{(2)}+\beta_{bbc}^{(2)}\right)/2$, $\beta_3^{(2)}=\left(\beta_{aca}^{(2)}+\beta_{bcb}^{(2)}\right)/2$, and $\beta_4^{(2)}=\left(\beta_{caa}^{(2)}+\beta_{cbb}^{(2)}\right)/2$, using *(a,b,c)* as the local coordinate system of the molecule. N_s is the surface number density of the probed chemical group. The tilt angle ϕ is between the c axis of the molecule and the $\perp$ (r') direction of the surface. The orientation parameter *D* is:

$$D=\langle\cos^3\phi\rangle/\langle\cos\phi\rangle.$$

Thus, the combination of Eq. (2.2) – (2.6) can be used to describe the relative amplitude of the SFS/SHS signal which is determined by the tilt angle ϕ and the molecular hyperpolarizability $\boldsymbol{\beta}^{(2)}$.

The tensor elements of β^q are related to the IR and Raman properties of the vibrational mode:

$$\beta_{ijk}^q \propto \frac{\delta\alpha_{ij}}{\delta Q_q}\frac{\delta\mu_k}{\delta Q_q} \tag{2.7}$$

in which $\frac{\delta\alpha_{ij}}{\delta Q_q}$ and $\frac{\delta\alpha_{ij}}{\delta Q_q}$ are the partial derivatives of the Raman polarizability tensor and the IR transition dipole moment of the q^{th} vibrational mode; and Q_q is the normal coordinate of the same mode. The symmetry properties of hyperpolarizability tensor reduce the number of non-zero and independent elements. Index permutations are possible for beams that are off resonance. These are visible (800 nm) and SFG beams for SFS experiments and all three beams for non-resonant SHS. Furthermore, the number of elements can be reduced more using the spatial symmetries of a molecule and the selected vibrational mode. The relative values for chemical groups such as CH_2 or CH_3 can be calculated using the Raman polarizability ratio [10]. These molecular groups do not participate in H-bonding and these values can be used in many experimental studies (for example, for fitting of SFG or SFS data). In contrast, for water molecules this approach does not work. Water molecules participate in H-bonding and thus its hyperpolarizability values are constantly changing in the dynamic environment of water at the surface [11]. The calculation of the hyperpolarizability using Eq. (2.7) is a challenging task because normal modes and vibrational levels have to be calculated and then averaged over time. Typically a time-dependent approach is used to simulate SFG spectra and surface susceptibility is calculated directly [12]. This approach involves a lot of computational parameters which have to be verified using reference samples. However, differences in reported experimental data, such as the heterodyne-detected SFG spectra of water/air interface, limit this approach [13]. For the SHS experiments (e.g. off resonance) the values of water hyperpolarizability are fluctuating because of the heterogeneity of solvent fluctuations and quantum mechanical fluctuations [14].

2.1.1.1 Normalization and correction for the difference in size distribution

In order to get a comparable value for the scattered SHS or SFS light from different samples we normalized measured SHS (SFS) intensity by the number of droplets (N_d) or liposomes (N_{lip}), obtainable from the amount of lipid used and the DLS distribution and correct for the difference in the radius (R).

For a *monodisperse* solution of droplets or liposomes that are smaller than ~200 nm in radius the total scattered signal (S) from a solution with N_p particles that each scatter an intensity $I(\theta)$ scales as follows [15]:

$$S(\theta) = I(\theta)N_p \propto \alpha(\theta)N_pR^6 \tag{2.8}$$

The factor α contains all the information about the surface response per droplet / liposome, independent of its size. Thus, if we want to compare the lipid or water response per droplet or liposome we have to compute the following:

$$\alpha(\theta) = \frac{S(\theta)}{N_pR^6} = I_{norm}(\theta, R) \tag{2.9}$$

which is what we have used in Chapter 6, and plot on the y-axis in Figure 6.2 A. Note that for the SFS data we plot the measured spectrum (I_{SF}/I_{IR}) and then use the procedure outlined in 6.2.3 to compute the average asymmetry per liposome in lipid number density using the fitted amplitudes of the symmetric P-O stretch and the symmetric CH_3 stretch mode as input. For both the SHS and SFS experiments we correct for polydispersity by replacing the radius *R* in Eq. (2.9) with an effective radius (R_{eff}). The procedure to calculate R_{eff} is described below.

2.1.1.2 Calculation of an effective radius

Since all particles contribute in the same way to the overall intensity of any light scattering experiment, we can use the DLS data to compute an effective radius that can be used for SHS and SFS experiments on polydisperse samples. DLS uses the temporal autocorrelation of scattered light to measure an intensity-weighted particle size distribution histogram. The output of such a measurement is a (normalized) distribution *D(R)*, which we will use here to correct the SHS and SFS signal for variations in the droplet / liposome size distribution, which affects both the scattered intensity per scatterer and the number of scatterers. In other words, we want to replace the total DLS intensity from a polydisperse distribution $\sum_i I(R_i)$ by an intensity $I_{norm}(\theta,R_{eff})$ from a 'monodisperse' solution. The obtained effective radius can then be used to normalize the SH intensity according to Eq. (2.9). In this way, we exclude intensity differences based on different sample sizes and obtain the surface scattering contribution $\alpha(\theta)$, which contains information about surface packing, hydration, and orientation of water molecules of a single scatterer. Explicitly we have from Eq. (2.9):

$$\alpha(\theta) = \frac{\sum_i I_i(\theta)}{N_p R^6} = \frac{S(\theta)}{N_p R_{eff}^6} = I_{norm}(\theta) \tag{2.10}$$

In the RGD limit, which is applicable here [7], the intensity of scattered light in a DLS measurement also scales with R^6, so that:

$$D(R) = \frac{P(R)R^6}{\int P(R)R^6 dR} \tag{2.11}$$

The particle size distribution *P(R)* is a normalized probability distribution, such that $\int P(R)dR = 1$.

We can calculate the particle size distribution from the DLS intensity-weighted distribution by:

$$P(R) = \frac{D(R)}{R^6} / \int \frac{D(R)}{R^6} dR \tag{2.12}$$

Using the particle size distribution we then calculate the effective radius for the liposomes using the following general expression:

$$R_{eff,lip} = \left[\frac{\int P(R) R^6 dR}{\int \frac{1}{2} P(R)(R^2 + (R-d)^2) dR} \right]^{1/4} \tag{2.13}$$

where the denominator takes into account that with changing radius the number of lipids per liposomes changes too (i.e. size and number density are related). For nanodroplets we have the following expression:

$$R_{eff,d} = \left[\frac{\int P(R) R^6 dR}{\int P(R) R^3 dR} \right]^{1/3} \tag{2.14}$$

where the denominator is now representing a sphere rather than a hollow shell.

2.1.2 Dynamic light scattering (DLS) measurements

Dynamic light scattering (DLS) measurements [3] (also known as photon correlation spectroscopy or quasi-elastic light scattering measurements) were used to characterize size distribution of droplets in studied samples. The sample is illuminated with the red HeNe laser (632 nm) and the scattered light is detected at the back-scattering geometry (175°) with the fast photodiode. The analysis of fluctuations of the intensity of the scattered light using correlation function *G(τ)* provides the value of the diffusion coefficient.

$$G(\tau) = \langle I(t) I(t+\tau) \rangle$$

The decay rate *Γ* (first cumulant) is obtained by fitting a third-order polynomial to the logarithm of the intensity correlation function. Second and third cumulants give information about the width of the size distribution [16]. The decay rate is linearly proportional to the diffusion coefficient *D* and scattering vector *q*:

$$\Gamma = q^2 D$$

The diffusion constant is related to the particle hydrodynamic radius *R* by the Stokes-Einstein formula:

$$D = \frac{k_B T}{6\pi\eta R}$$

where k_B is the Boltzmann constant, *T* is the temperature, and *η* is the solvent viscosity.

2.1.3 ζ-potential measurements

Charged particles or droplets dispersed in the ionic solution attract ions of opposite charge. All surface charge is screened by a Stern layer and diffuse layer of ions. When a charged particle moves, part of solvent molecules and ions from the diffuse layer move with the particle because of the viscosity of the solution. A plane dividing the volume of solvent which is firmly attached to the particle from that which is called the slipping plane. The electrophoretic mobility μ of particles can be experimentally measured when the particle moves with constant speed v in the uniform electric field E.

$$\mu = \frac{v}{E}$$

The speed can be measured using a technique based on the Doppler effect and called laser Doppler velocimetry. The change in frequency of a back-scattered laser beam Δf can be measured and related to the speed v, scattering angle θ and laser wavelength λ:

$$\Delta f = \frac{2v \sin \theta/2}{\lambda}$$

The relationship between the electrophoretic mobility and electrokinetic potential at the slipping plane Φ_ζ (called ζ-potential) is given using Smoluchowski approximation [4]:

$$\mu = \frac{\phi_\zeta \varepsilon \varepsilon_0}{\eta}$$

where η is the viscosity of the solvent, ε is the dielectric constant of the dispersion medium, and ε_0 is the permittivity of free space.

2.2 Experimental details

In this section, we describe details of dynamic light scattering, ζ-potential, FTIR, sum frequency and second harmonic scattering measurements.

2.2.1 Sample characterization

DLS measurements were performed using Malvern zeta-sizer Nano ZS and disposable polystyrene or quartz cuvettes for chlorinated solvents. ζ-potential measurements were performed using the same device in disposable polystyrene electrophoretic cell with gold electrodes. For measurements of water droplets in chlorinated solvents or in oil, we used a dip cell made from polyether ether ketone (PEEK) with palladium electrodes in a quartz cuvette which allows using larger E-fields.

FTIR measurements were performed using a Bruker Vertex 70 spectrometer equipped with Ag mirrors. Spectra used for SFS normalization purposes were collected in transmission mode using the same cuvette as for SFS measurements (52 µL 0.2 mm light path 106-QS quartz cuvette from Hellma). The detachable window was replaced with 1.3 mm thick CaF_2 window from CeNing Optics.

2.2.2 Temperature-dependent sum frequency scattering

Vibrational sum frequency spectra were measured using the setup for sum frequency generation experiments described in Ref. [17-19]. An 800 nm regeneratively amplified Ti:sapphire system (Spitfire Pro, Spectra physics) seeded with an 80 MHz 800 nm oscillator (Integral 50, Femtolasers) was operated at a 1 kHz repetition rate to pump a commercial optical parametric generation/optical parametric amplification/difference frequency generation (OPG/OPA/DFG) system (HE-TOPAS-C, Light Conversion), which was used to generate IR pulses. The visible beam was split off directly from the amplifier and spectrally shaped with a home-built pulse shaper. The angle between the 10 µJ visible (VIS) beam (800 nm, FWHM <15 cm^{-1}) and the 6 µJ IR beam (~9400 nm or 3200-5000 nm, FWHM ~160 cm^{-1}) was 20° as measured in air. The focused laser beams were overlapped in a sample cuvette with a path length of 200 µm. The size of the focus of IR beam is ~70 µm and of VIS beam is ~150 µm. At a scattering angle of 55°, the scattered SF light was collimated using a plano-convex lens (f=15 mm, Thorlabs LA1540-B) and passed through two short wave pass filters (3rd Millenium, 3RD770SP). The SF light was spectrally dispersed with a monochromator (Acton, SpectraPro 2300i) and detected with an intensified CCD camera (Princeton Instruments, PI-Max3) using a gate width of 10 ns. A Glan-Taylor prism (Thorlabs, GT15-B), a half-wave plate (EKSMA, 460-4215) and a polarizing beam splitter cube (CVI, PBS-800-050) and two BaF_2 wire grid polarizers (Thorlabs, WP25H-B) were used to control the polarization of the SFG, VIS, and IR beams, respectively. The recorded intensity was baseline subtracted and normalized to the SFG spectrum of a gold mirror (z-cut quartz) in PPP (SSP) polarization that was recorded before each measurement. Typical acquisition times are given in Table 2.1 and the setup is sketched in Figure 2.2.

Type of samples	Vibrational region	Acquisition time, min
Water droplets	OD-stretch and CH-stretch	90
Planar CaF_2/SDS/D_2O interface	OD-stretch and CH-stretch	25
Water droplets, oil droplets	CH-stretch	3
Liposomes	PO_2^--stretch	10-20
Liposomes	CH-stretch	40
Oil droplets stabilized with lipids	PO_2^--stretch	3

Table 2.1. Typical acquisition times for SFS measurements of different samples described in the thesis.

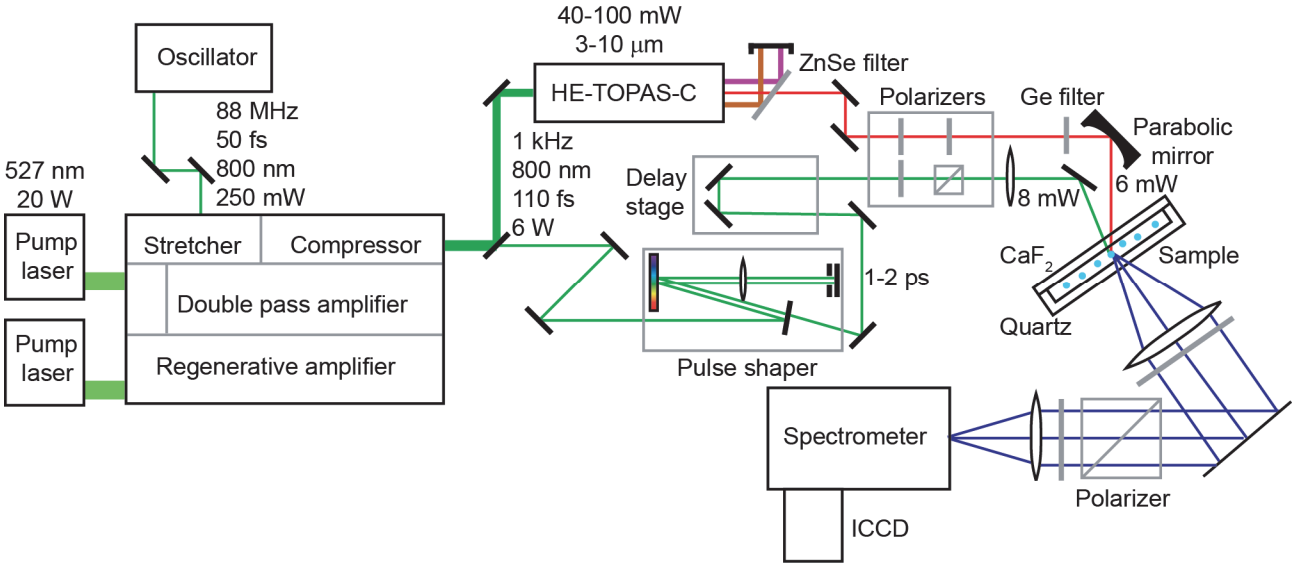

Figure 2.2. Scheme of the SFS setup (not to scale). The setup consists of a Ti:Sa oscillator, two stage amplifier which is pumped with 2 Nd:YAG lasers, and a commercial OPG/OPA/DFG system (HE-TOPAS-C). The 800 nm beam that exits the laser is split, then stretched in time in the pulse shaper and then overlapped with IR beam in time and space in the sample using a delay stage. The scattered light from the sample is collimated, polarization selected, filtered, and guided to the intensified CCD camera.

Temperature controlled SFS measurements were performed using a custom made sample cell (Quantum Northwest, Figure 2.3). The sample cuvette was placed in a metallic holder cooled with a single Peltier element. The sample chamber was closed and filled with N_2 gas to avoid condensation of air. The windows of the temperature cell were made from CaF_2 (for the incoming beams) and quartz (for the scattered SF beam). The temperature cell itself was thermally isolated and also placed inside a box purged with N_2 gas. The hot side of the Peltier element was cooled with a flow of cold liquid ethanol (223 K, using a peristaltic pump, Ismatec ISM1200). The cold ethanol was obtained by cooling ethanol inside a copper coil that was placed in a bath containing a mixture of dry ice and ethanol. The IR beam path outside the laser source was purged with N_2 gas. The setup in working condition is shown in Figure 2.4.

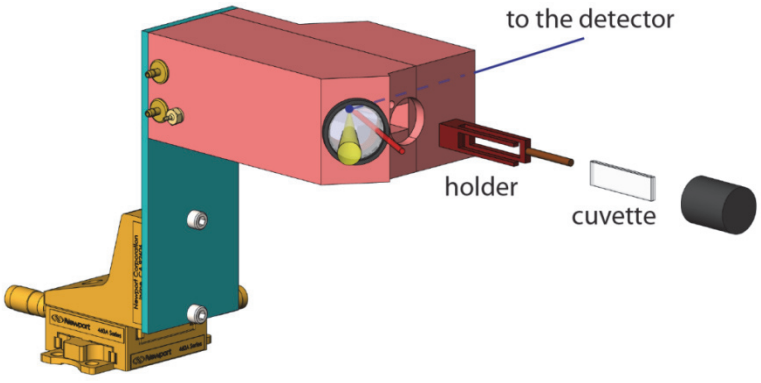

Figure 2.3. Illustration of the temperature cell used in the SFS experiments. The yellow beam indicates the IR pulses, the red beam indicates the VIS pulses and the blue line indicates the scattered SF light.

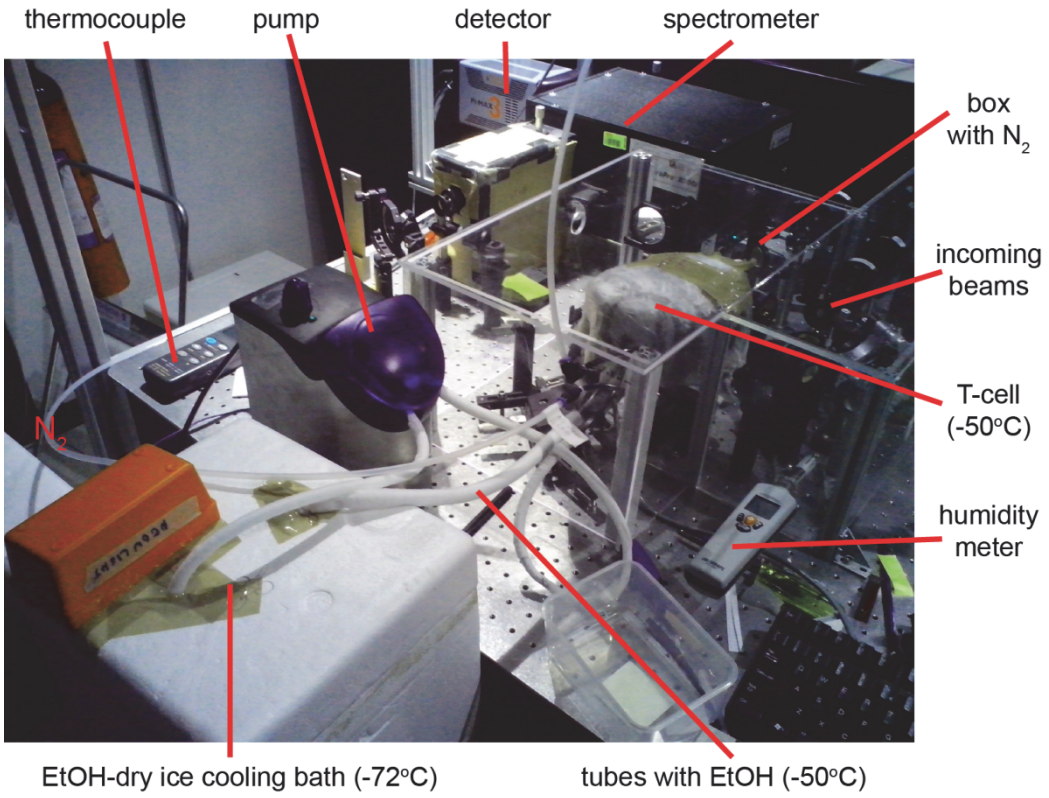

Figure 2.4. A photo of the temperature cell inside the setup. The cell is wrapped in polyurethane foam. The hot side of the Peltier element in the temperature cell is cooled with the flow of cold ethanol which is passing through a copper tube, that is placed in an ethanol-dry ice cooling bath. The setup is purged with N_2 to avoid absorption of the IR pulses by CO_2 and condensation of water or ice on the cold surfaces. The saturation of the box with N_2 is controlled with a humidity meter and the thermocouple measures the temperature of the cooling bath.

2.2.3 Generation of broad spectral IR pulses

In order to probe the whole frequency range of the D_2O stretch mode region, we stepped our 160 cm^{-1} FWHM IR pulses through the spectral window between 2000 cm^{-1} and 3400 cm^{-1} using 50 nm steps by automatically adjusting the HE-TOPAS-C options (leading to a total acquisition time of 5400 s per spectrum). Figure 2.5A shows SF spectra for the different IR center frequencies recorded in reflection mode from a z-cut quartz crystal. The summed spectrum for one of the runs is shown in Figure 2.5B. The SFS (or reflection SFG) data is recorded at these wavelengths, then each of these spectra is baseline subtracted, and then all of them are added up and divided by the spectrum of quartz. The reflection SFG spectrum for a planar D_2O/CaF_2 interface with 10 mM SDS in shown in Figure 2.6 and has good agreement with the literature [20]: all peaks from strongly H-bonded water (2370 cm^{-1}) to weakly H-bonded water (2520 cm^{-1}), free OD (2740 cm^{-1}) and CH modes (2800-3000 cm^{-1}) are present.

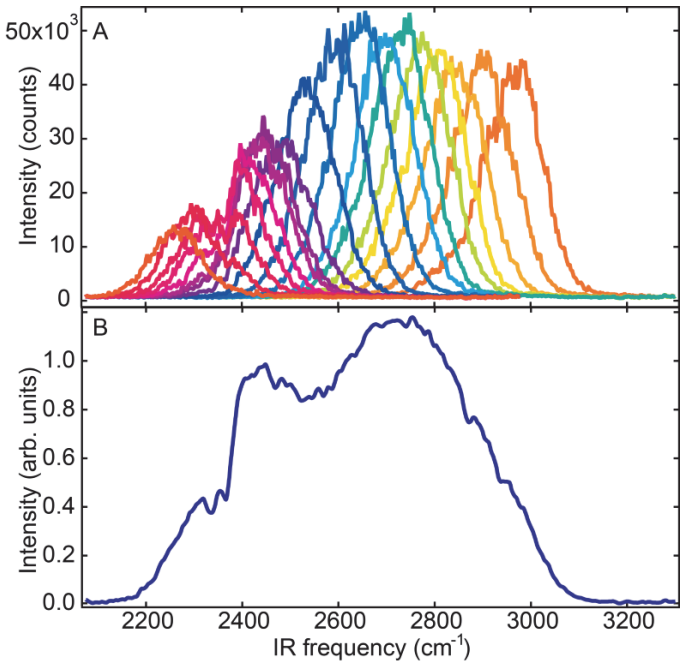

Figure 2.5. IR spectra. A: SFG reflection mode spectra from a z-cut quartz crystal reflecting the spectral shape of the used IR pulses. B: The total IR spectrum resulting from the scan in panel A.

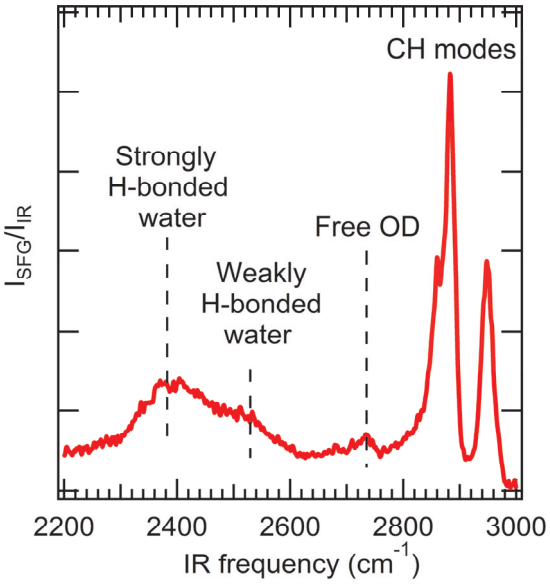

Figure 2.6. Reflection SFG spectrum from a planar CaF_2/10 mM SDS/D_2O interface measured in SSP polarization combination. The peak assignment is given in the figure.

2.2.4 Fitting of sum frequency spectra

The SFS signal intensity $S_{SFS}(\theta,\omega)$ can be described by the following Lorentzian line shape expression [21]:

$$S_{SFS}(\theta,\omega) \propto \left| A_{NR}(\theta) f(\omega) e^{i\varphi_{NR}} + \sum_i \frac{A_i(\theta)\gamma_i}{\omega-\omega_i+i\gamma_i} \right|^2, \qquad (2.15)$$

where $A_{NR}(\theta)$ is the amplitude and $f(\omega)$ is the spectral shape of a weakly dispersive ('non-resonant') background, φ_{NR} is the phase of the background signal relative to that of the resonant signal, $A_i(\theta)$ is the amplitude of the ith vibrational mode with the resonance frequency ω_i and linewidth γ_i. The strength of the vibrational mode is proportional to A_i ($\omega = \omega_i$). The SFS spectra (I_{SFS}/I_{IR}) were fitted using Eq. (2.15), employing IGOR Pro 6 (WaveMetrics) and using Levenberg-Marquardt iterations. The SFS spectra that do not show any detectable features are fitted with a 3rd order polynomial.

2.2.5 Second harmonic scattering

Second harmonic scattering measurements were performed, as previously described in detail [22], using 190 fs laser pulses at 1028 nm with a 200 kHz repetition rate (Pharos, Light Conversion). The input polarization is controlled by a Glan-Taylor polarizer (GT10-B, Thorlabs) and a zero-order half wave plate (WPH05M-1030). The filtered (FEL0750, Thorlabs) input pulses with a pulse energy of 0.3 µJ (incident laser power P = 60 mW) were focused into a cylindrical glass sample cell (4.2 mm inner diameter) with a beam waist diameter of ~32 µm and a Rayleigh length of 3.2 mm. The scattered SH light was collected and collimated with a plano-convex lens (f = 5 cm), polarization analyzed (GT10-A, Thorlabs), filtered, (ET525/50, Chroma) and finally focused into a gated photomultiplier tube (PMT H7421-40, Hamamatsu). Data points for scattering patterns were acquired in steps of 5° from -90° to 90° and an acceptance angle of 3.4°. Typically, measurements settings were 20 x 2 s acquisition time and a gate width of 10 ns. To correct for incoherent hyper Rayleigh scattering (HRS) from the aqueous phase, both the SHS response from the sample solution and the HRS response from the solution without particles are detected under the same conditions. The HRS is then subtracted from the SHS. The obtained difference is then normalized to the isotropic SSS signal of pure water so that we correct for any form of aberration due to differences in the beam profile and obtain a value that can be compared to any other measurement done in the same procedure.

$$\mathrm{S}(\theta) = \left[\frac{I(\theta)_{SHS,sample,PPP} - I(\theta)_{HRS,solution,PPP}}{I(\theta)_{HRS,water,SSS}} \right] \tag{2.16}$$

Figure 2.7 shows the scheme of the second harmonic scattering setup.

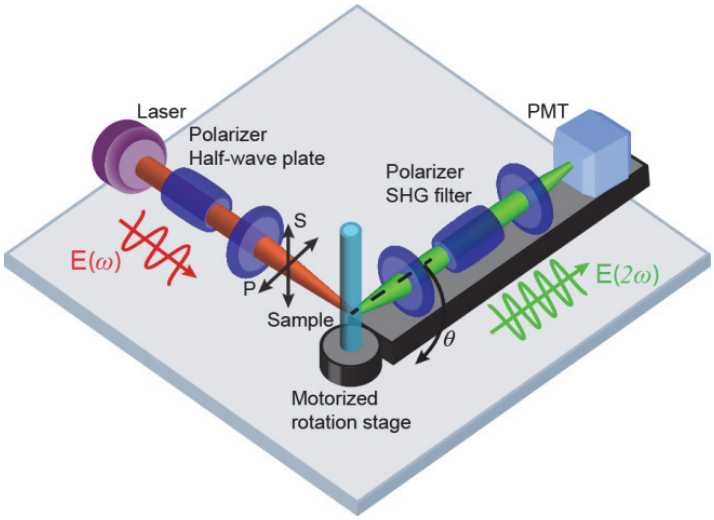

Figure 2.7. The scheme of SHS setup. The focused polarized laser beam illuminates the sample in the cylindrical cuvette. The scattered SH light is detected with the PMT mounted on the rotation stage, after passing through the SHG filter and the polarization analyzer.

The reproducibility of the SHS measurements is 1-2 % (for aqueous solutions) and 5-6 % for the used liposome and droplet solutions. The latter number reflects the uncertainty in the reproducibility of the preparation of the samples. All measurements were performed at 25°C.

2.3 References

1. Boyd, R.W., *Nonlinear Optics (Third Edition)*2008, Burlington: Academic Press. 613.
2. Lambert, A.G., P.B. Davies, and D.J. Neivandt, *Implementing the Theory of Sum Frequency Generation Vibrational Spectroscopy: A Tutorial Review.* Appl. Spectrosc. Rev., 2005. **40**(2): p. 103-145.
3. Berne, B.J.P., R., *Dynamic light scattering : with applications to chemistry, biology, and physics* 2000, New York: Courier Dover Publications.
4. Hunter, R.J., *Zeta Potential in Colloid Science: Principles and Applications* Colloid Sciences Series1989, Cambridge: Academic Press.
5. Roke, S., et al., *Vibrational sum frequency scattering from a sub-micron suspension.* Phys. Rev. Lett., 2003. **91**: p. 258302.
6. de Beer, A.G.F. and S. Roke, *Obtaining molecular orientation from second harmonic and sum frequency scattering experiments in water: Angular distribution and polarization dependence.* J. Chem. Phys., 2010. **132**(23): p. 234702.
7. de Beer, A.G.F. and S. Roke, *Sum frequency generation scattering from the interface of an isotropic particle: Geometrical and chiral effects.* Phys. Rev. B, 2007. **75**(24): p. 245438.
8. de Beer, A.G.F., S. Roke, and J.I. Dadap, *Theory of optical second-harmonic and sum-frequency scattering from arbitrarily shaped particles.* J. Opt. Soc. Am. B, 2011. **28**(6): p. 1374-1384.
9. Gonella, G., et al., *Second Harmonic and Sum-Frequency Generation from Aqueous Interfaces Is Modulated by Interference.* The Journal of Physical Chemistry C, 2016. **120**(17): p. 9165-9173.
10. Zhuang, X., et al., *Mapping molecular orientation and conformation at interfaces by surface nonlinear optics.* Phys. Rev. B, 1999. **59**(19): p. 12632-12640.
11. Morita, A. and J.T. Hynes, *A Theoretical Analysis of the Sum Frequency Generation Spectrum of the Water Surface. II. Time-Dependent Approach.* J. Phys. Chem. B, 2002. **106**(3): p. 673-685.
12. Nagata, Y., et al., *Molecular Modeling of Water Interfaces: From Molecular Spectroscopy to Thermodynamics.* J. Phys. Chem. B, 2016. **120**(16): p. 3785-3796.
13. Ni, Y. and J.L. Skinner, *Communication: Vibrational sum-frequency spectrum of the air-water interface, revisited.* J. Chem. Phys., 2016. **145**(3): p. 031103.
14. Liang, C., et al., *Solvent fluctuation and nuclear quantum effects modulate the molecular hyperpolarizability of water.* arXiv, 2017: p. 1705.01649.
15. de Beer, A.G.F. and S. Roke, *Nonlinear Mie theory for second-harmonic and sum-frequency scattering.* Phys. Rev. B, 2009. **79**(15): p. 155420.

16. Tyrode, E. and J.F.D. Liljeblad, *Water Structure Next to Ordered and Disordered Hydrophobic Silane Monolayers: A Vibrational Sum Frequency Spectroscopy Study.* J. Phys. Chem. C, 2013. **117**(4): p. 1780-1790.
17. de Aguiar, H.B., et al., *Comparison of scattering and reflection SFG: a question of phase-matching.* Phys. Chem. Chem. Phys., 2012. **14**: p. 6826-6832.
18. Scheu, R., et al., *Stern Layer Formation Induced by Hydrophobic Interactions: A Molecular Level Study.* J. Am. Chem. Soc., 2013. **135**(51): p. 19330-19335.
19. Scheu, R., *Specific ion effects and the molecular structure of water, ions and amphiphiles on nanoscopic hydrophobic interfaces*, 2014: École Polytechnique Fédérale de Lausanne. p. 75.
20. Becraft, K.A., F.G. Moore, and G.L. Richmond, *In-situ spectroscopic investigations of surfactant adsorption and water structure at the CaF2/aqueous solution interface.* Phys. Chem. Chem. Phys., 2004. **6**(8): p. 1880-1889.
21. de Aguiar, H.B., et al., *Surface structure of SDS Surfactant and oil at the oil-in-water droplet liquid/liquid interface: A manifestation of a non-equilibrium surface state.* J Phys Chem B, 2011. **115**: p. 2970-2978.
22. Gomopoulos, N., et al., *Label-Free Hyper Rayleigh and Second Harmonic Scattering with High Efficiency.* Opt. Express, 2013. **21**(1): p. 815-821.

Chapter 3: Sum frequency and second harmonic generation from the surface of a liquid microjet

The use of a liquid microjet as a possible source of interest for Second Harmonic Generation (SHG) and Sum Frequency Generation (SFG) spectroscopy is examined. We measured non-resonant SHG scattering patterns from the air/water interface of a microjet of pure water and observe a strong enhancement of the SHG signal for certain scattering angles. These enhancements can be explained by the optical properties and the shape of the liquid microjet. SFG experiments at the surface of a liquid microjet of ethanol in air show that it is also possible to measure the coherent vibrational SFG spectrum of the ethanol/air interface in this way. Our findings are useful for future far-UV or X-ray based nonlinear optical surface experiments on liquid jets. In addition, combined X-ray photoelectron spectroscopy, and SHG/SFG measurements are feasible, which will be very useful in improving our understanding of the molecular foundations of electrostatic and chemical surface properties and phenomena.

This chapter is based on the paper by Nikolay Smolentsev, Yixing Chen, Kailash C. Jena, Matthew A. Brown, and Sylvie Roke "Sum frequency and second harmonic generation from the surface of a liquid microjet" published in the Journal of Chemical Physics, 2014, 141 (18), p. 18C524

3.1 Introduction

Liquid and aqueous interfaces in particular are intimately connected to many biological, chemical and physical processes, such as protein folding and aggregation [1, 2], biological membrane formation [3, 4], catalysis [5, 6], emulsion and aerosol processing [7, 8]. Knowledge of the molecular surface structure is crucial for the understanding of these processes. Molecular level information of an interface can be obtained by using nonlinear surface spectroscopy. The two most common methods are Second Harmonic Generation (SHG) and Sum Frequency Generation (SFG) that were first applied to probing surfaces in 1969 by Brown and Matsuoka [9] and in 1987 by Guyot-Sionnest et al [10, 11], and Harris et al. [12], respectively. In a surface SHG or SFG experiment two intense electromagnetic fields from a pulsed laser source (two beams with identical, often near-infrared or visible frequency (SHG) or an infrared and visible pulse pair (SFG)) are reflected from an interface, where they induce a second-order polarization that oscillates at the second harmonic or sum frequency. The magnitude and spectral shape are determined by the second-order susceptibility tensor ($\boldsymbol{\chi}^{(2)}$) of the material, which represents an averaged response of all molecular responses. Since $\boldsymbol{\chi}^{(2)}$ is a physical property of the material, it must also reflect the spatial symmetry properties of that material (Neumann's principle). As a consequence, (in the electric-dipole approximation) $\boldsymbol{\chi}^{(2)}$ vanishes in centrosymmetric bulk media [13]. This means that SHG and SFG can often be applied as surface sensitive techniques, with which only the first few molecular layers situated at the interface are probed. Vibrationally resonant SFG can be used to measure the coherent vibrational surface spectrum from the interface, which contains information about molecular composition, order, and chirality. Since the initial experiments, thousands of studies have been performed to elucidate the molecular complexity of a large variety of interfaces (reviewed in e.g. [14-27]). The most commonly employed geometry is the reflection geometry from a planar interface, but other geometries are also used. Scattering SHG or SFG, for example, can be used to probe the interfaces of micron and nanometer sized particles and droplets [28, 29]. Such a geometry, aside from allowing access to the interface of small particles in a buried liquid or solid media, also has advantages in decreasing the inherent challenges that are caused by chemical contaminations, which are present in every sample [30]. Scattering experiments thus form an attractive alternative for studying liquid/liquid interfaces [31]. Liquid jets are another alternative for reducing impurity induced artifacts [32, 33], as the interface is continuously refreshed, or avoiding the use of windows [34-36] when the optical excitation demands such applications. Heating effects are also eliminated in the liquid jet, and it allows to study kinetics at interfaces [37-39]. Liquid jets are mostly used in X-ray photoelectron spectroscopy (XPS) and X-ray absorption spectroscopy experiments [40-44], but have been used as well in kinetic resonant second harmonic experiments [37]. Recently, a microflow system based on a liquid microjet combined with a fluorescence microscope was employed to study interfacial reactions [38, 39]. Cooling and freezing of bulk water in droplets have

been studied using femtosecond X-ray spectroscopy on a liquid microjet [45]. Liquid microjets can also be used to study adsorption kinetics of surfactants on millisecond and submillisecond timescales [46-49] which is important for stabilizing foams, spreading of droplets on solid surfaces, inkjet printing, the coalescence of droplets and the breakup of jets. Furthermore, recent studies show that the ordering of water molecules can be different with flow and without flow [50].

Here, we explore the use of a liquid jet to perform non-resonant elastic second harmonic generation and vibrationally resonant sum frequency generation. We measure non-resonant SHG scattering patterns from the air/water interface of a microjet of pure water and observe a strong enhancement of the SHG signal for certain scattering angles. This enhancement can be explained by the optical properties and shape of the liquid microjet. SFG experiments at the surface of a liquid microjet of ethanol in air show that it is also possible to measure the coherent vibrational SFG spectrum of the ethanol/air interface. Based on our experiments, it should be possible in the future to use liquid jets to perform far-UV or X-ray based surface experiments employing SHG and SFG. In addition, combined X-ray photoelectron spectroscopy and SHG/SFG measurements are feasible, which will be very useful in improving our understanding of the molecular foundations of electrostatic and chemical surface properties and phenomena [51]. In what follows, we first describe experimental details of the jet and the optical setups. Then we present SHG angular patterns from the liquid microjet and investigate the optical properties of the scattering geometry with ray optics. Finally, we present the results of the SFG experiments that were performed on a liquid microjet of ethanol.

3.2 Experimental procedures

We used the liquid microjet setup described in Ref. [52, 53]. Briefly, this liquid jet source consists of an HPLC pump operating with a flow rate of 0.4 ml/min that is connected to a quartz nozzle (Microliquids GmbH) with an inner diameter of 35 μm. Pure water or ethanol was continuously pumped through an injection loop made of perfluoroalkoxyalkane (PFA) that is connected to a 2 μm inline PEEK filter that connects to the nozzle. The nozzle was mounted using a 3D translation stage (SmarAct piezo motors), such that the jet flow was vertical. The liquid flow is stable in air and remains intact for at least 2 mm downstream after exiting the nozzle. The jet eventually breaks up due to Rayleigh instabilities to yield aerosols. Consequently, the first 2 mm of the liquid flow is optically transparent (corresponding to laminar flow). Figure 3.1A shows a photograph of the liquid jet in operation.

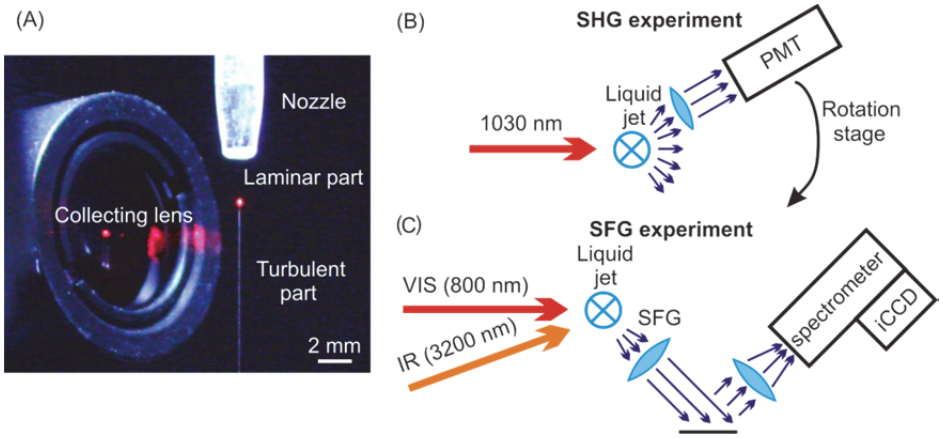

Figure 3.1: Illustration of the experiments A: Photograph of the liquid microjet in operation next to the collecting lens of the SFG setup. The microjet is illuminated by a red diode laser at the boundary between the laminar flow (top, transparent) and turbulent (bottom, white) sections of the liquid microjet. B: Schematic layout of the horizontal plane of the SHG experiment. C: Schematic layout of the horizontal plane of the SFG experiment.

The system used for non-resonant SHG is described in detail in the Section 2.2.5. Figure 3.1B shows a sketch of the setup. The gate width of the PMT was set to 10 ns, the acquisition time was 1.5 seconds and 20 acquisitions were averaged for each data point. The scattered SHG signal was measured with angular steps of 5° and an angular resolution of 3.5°.

Broad-band vibrational sum frequency spectra were measured using the setup for sum frequency generation experiments described in the Section 2.2.2. The angle between the 10 µJ visible (VIS) beam (800 nm, FWHM 15 cm^{-1}) and the 10 µJ IR beam (3200 nm, FWHM 163 cm^{-1}) was 20°. The SFG signal was detected at 45° with respect to the IR beam (see Figure 3.1 C for a sketch). The angular resolution was 22°. The SFG and VIS beams were polarized in the vertical (S) direction, and the IR beam was polarized in the horizontal plane (P), leading to the polarization combination SSP. The recorded intensity was baseline subtracted and normalized by the SFG spectrum of a z-cut quartz crystal that was recorded before each measurement.

Ethanol (99.9 %) was purchased from Sigma-Aldrich. Ultra-purified, filtered and UV treated H_2O with an electrical resistance of at least 18.2 MΩ·cm was obtained from a Milli-Q direct-Q-3UV system (Millipore, Inc.). For a typical measurement ~10 mL of liquid was needed.

3.3 Results and discussion

We investigate the use of a liquid jet by measuring angular SHS intensity patterns in multiple polarization combinations, and for different incident powers. SHS can originate from bulk water in the form of hyper Rayleigh scattering (HRS) as well as from the air/water interface. HRS is a weak incoherent SHG process that originates from the electronic non-centrosymmetry of isotropic liquid molecules [54, 55]. The HRS intensity in the polarization combination SS is the largest (approxi-

mately 8 x larger than the intensity in the combination PP) and the angular intensity is uniform [56]. In contrast, non-resonant SHG signal that is reflected from a water/air interface is strongly peaked around the phase-matched direction and is emitted preferentially in the PP polarization combination. Both HRS and surface SHG processes are characterized by a quadratic dependence on power of the incoming beam.

3.3.1 The liquid jet as a micro-lens

Figure 3.2A shows typical SHG scattering patterns in PP and SS polarization combinations from a water jet. The PP signal displays two sharp peaks at ~35° on top of two broader less intense peaks. The SS signal is also shown, which does not display much intensity. The shape of the pattern was the same for the laminar and the turbulent parts of the liquid jet. It can be seen that the PP signal is 20 x more intense than the SS signal. In addition, the maximum intensity of the PP SHG signal from the liquid jet is 15 x larger than hyper-Rayleigh scattering in SS polarization from bulk water in a cuvette [57]. Given the difference between surface SHG and HRS, it is thus likely that the signal originates from the air/water interface and not from the bulk water. It is of further interest to note that the signal at 35° is ~ 50 x larger than the signal in the direction of the sum of the incoming wave vectors (phase matched direction, without refraction in the jet). In what follows we explain this behavior. For understanding the scattering pattern we use a simplified approach based on ray optics and Gaussian beam optics. We use Mie theory to qualitatively confirm our findings.

To explain the observed angular intensity pattern and to arrive at a reasonable estimate of the found curve, we first consider the intensity characteristics of the fundamental beam with ray optics [45] and Mie scattering [58], and subsequently consider the resulting SH emission. A central parameter in ray optics is the distance of a ray that enters or exits the jet with respect to the optical axis (in the horizontal plane and perpendicular to the optical axis). We assign this parameter with x for the entering beam and y for the emitted beam (see Figure 3.2B). The jet can be modeled as a water cylinder with radius *r* and refractive index *n*. The relationship between x and y is given by:

$$y = r\sin\left(2\arcsin\frac{x}{nr} - \arcsin\frac{x}{r}\right). \tag{3.1}$$

The emission or scattering angle θ is given by:

$$\theta = 2(\arcsin\frac{x}{r} - \arcsin\frac{x}{nr}). \tag{3.2}$$

The intensity of the fundamental beam I_ω at the back side of the cylinder can be expressed as a function of the incoming intensity:

$$I_\omega = I(x)\frac{dx}{dy}. \tag{3.3}$$

It can be shown that this function goes to infinity at a scattering angle of θ=39.2°, which means that there will be strong focusing effect at the back of the cylinder. This angle agrees well with the maximum angle in Figure 3.2A. Our data, however, is not very sharply peaked as the above consideration suggests. Since the size of the 'focus' at 39.2° is limited by diffraction effects it cannot be smaller than the fundamental wavelength (1.028 μm) so that the peaks in the angular pattern will be broadened. The actual size of the focus of the fundamental beam can be estimated more accurately by using linear Mie scattering theory. Figure 3.2B shows the calculated E-field distribution for a plane wave of 1028 nm illuminating a water (n=1.33) cylinder with a 35 μm diameter [58].

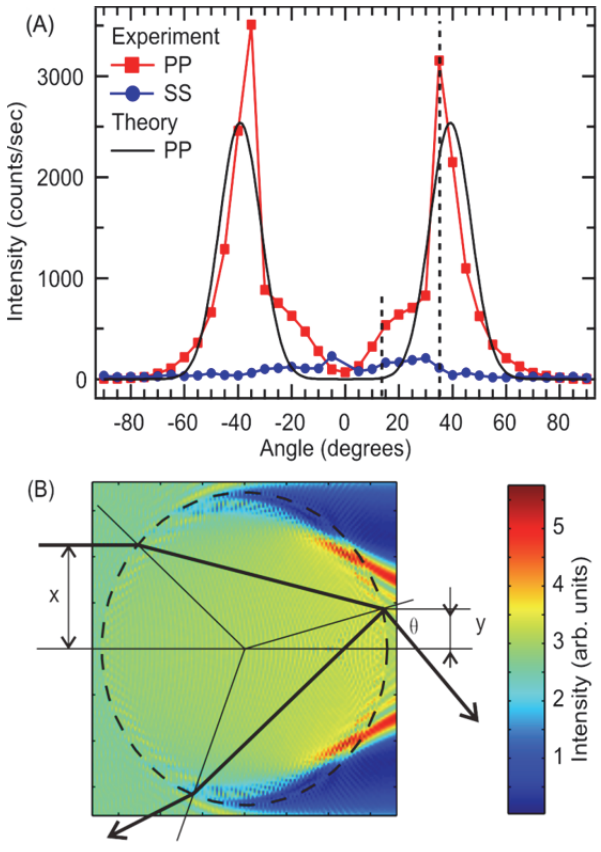

Figure 3.2. Second harmonic generation from a water jet. A: Scattering pattern from the laminar part of the liquid water jet. The polarization combinations were PP (red curve) and SS (blue curve). The dashed lines indicate the angles at which the power dependence measurements of Figure 3.3 were performed. The black solid line shows two Gaussian peaks with an angular FWHM width of 18.2° centered at 39.2°, which represents the result of the considerations described in the text. B: Linear Mie calculation electric field amplitude of the fundamental beam in P-polarization for a pla-

nar wave scattered from a cylinder of water. The drawing shows a scheme of refraction of one ray at the front and back side of the liquid jet.

At the back surface of the jet, the focused beam generates second harmonic photons in either reflection or transmission mode. Only the transmitted part reaches the detector. The reflected SHG light travels back through the liquid and then exits the jet in the direction of the incoming fundamental beam. The intensity of the transmitted second harmonic radiation can be written as:

$$I_{2\omega} \propto {\chi^{(2)}}_{eff} I_{\omega}^{2} \tag{3.4}$$

where ${\chi^{(2)}}_{eff}$ is the second-order susceptibility, which represents the response of the surface. For the polarization combination SS, the signal only relies on the $\chi^{(2)}_{y'y'y'}$ elements (with *x',y',z'* defined as a coordinate system with *z'* along the radially directed surface normal and *x'* along the azimuthal angle and *y'* along the length of the cylinder). Since this element vanishes for isotropic surfaces [27], Eq. (3.4) leads to $I_{2\omega} = 0$ for SS polarization. For the polarization combination PP, SHG signal arises from the elements $\chi^{(2)}_{z'z'z'};\ \chi^{(2)}_{z'x'x'} = \chi^{(2)}_{z'y'y'};\ \chi^{(2)}_{y'z'y'} = \chi^{(2)}_{x'z'x'};\ \chi^{(2)}_{x'x'z'} = \chi^{(2)}_{y'y'z'}$ which are non-zero.

Assuming that the beams are Gaussian in shape, the broadening of the peaks in the angular pattern can be estimated. The divergence Δθ of the Gaussian SHG beam is given by $\Delta\theta = \frac{\lambda}{\pi b}$ =18.2° where b is half the beam waist, i.e. 2b=1.028 μm, and λ is the SH wavelength (514 nm). This estimated size of the area of the generated SH light is in agreement with theoretical values [59]. A normalized representation of $I_{2\omega}$ that consists of two Gaussian peaks centered around 39.2° and with a FWHM width of 18.2° is plotted in Figure 3.2A. This curve can be seen to capture the essentials of the observed PP scattering pattern. Thus, the angular pattern can be explained by focusing of the incoming beam on the backside of the liquid jet in combination with subsequent surface second harmonic generation in transmission from the air/water interface. We note that this model is valid when the jet size (35 μm) is smaller or comparable with the fundamental beam waist (35 μm) and it is much larger than the wavelength (1.030 μm). Nonlinear Mie scattering theory can provide a more rigorous description of the angular pattern [60].

In Figure 3.2A the SH intensity at θ = 40° is much larger than the intensity that appears at θ = 0°, i.e. the phase matching direction (without refraction in the jet). We can now see that this is caused by the focusing properties of the liquid jet that depend only on the wavelength, the shape of the jet and the refractive index of the liquid. With such high intensities being generated at the backside of the liquid jet, it is valid to investigate to what extent this high intensity is damaging the material or altering its response. We have therefore measured the SHG response at two different

scattering angles as a function of increasing incident pulse power. If there are no higher order effects or thermal lensing [61] we expect that the intensity scales quadratically with the incident power (P). Figure 3.3 displays the emitted SHG intensity for two different scattering angles that are highlighted with dashed lines in Figure 3.2 A (θ=15° and θ=35°) versus power of the incoming beam. The solid lines are fits to a quadratic power dependence. Since the data can be described well by a quadratic dependence, we conclude that there is little influence of the higher order processes on the signal. An explanation for this observation can be found by considering the beam size and the flow speed of the jet: The jet flows with 7 m/s (or 35 μm for every 5 μs, which is the interval between the laser pulses). Thus, for every new pulse (with a 35 μm beam waist at the front plane, and a focus of 2 μm in horizontal and 35 μm in the vertical direction) at the back plane) the interface is continuously refreshed. Thus, there is no sign of photodamage or changes in surface structure due to laser induced heating [62] and one can use almost unlimited laser power.

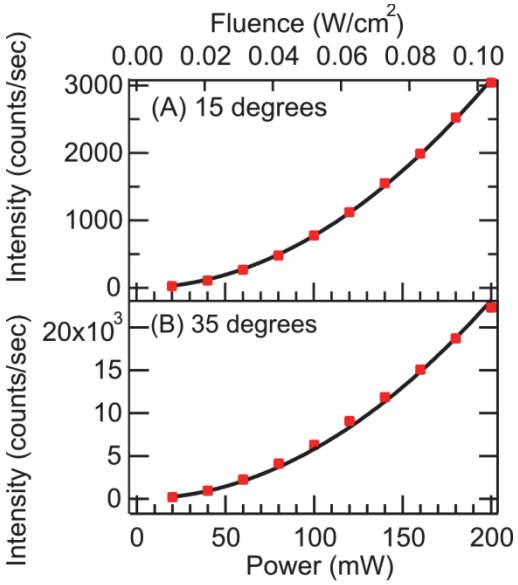

Figure 3.3. Power dependence of the SHG intensity (data points) from the liquid jet of water for different scattering angles: θ = 15° (A) and, θ = 35° (B). The iris size was 3 mm, corresponding to 3.5° angular resolution. The solid black line is a quadratic fit. The power was measured just before the beam hits the jet.

3.3.2 SFG from a jet of ethanol

To test whether the observed intensity increase and angular dependence can also be exploited with sum frequency generation, we have performed an SFG experiment using a liquid microjet of ethanol (C_2H_5OH). Ethanol is an ideal reference solution because of its well-established spectral resonance in the 3 micron region of the IR spectrum, which was used in these experiments [63]. The experiment was performed in the geometry sketched in Figure 3.1 C. Figure 3.4 shows the SFG spectra recorded in the polarization combination SSP, and acquired with an integration time

of 900 s. The spectrum displays three resonances: The CH_3 Fermi resonance at 2940 cm^{-1}, the CH_3 symmetric stretch mode at 2875 cm^{-1}, and the CH_2 symmetric stretch mode at 2850 cm^{-1}. These resonances were also observed in SFG experiments from a planar ethanol/air interface [63]. Compared to Refs. [63, 64], the spectrum in Figure 3.4 has a larger symmetric CH_2 peak stretch mode. The difference can be explained either by slight differences in the chemical surface structure or by the difference in spectral resolution. As with the SHG experiments, no signal was recorded in the forward direction. Compared to the SHG data in Figure 3.2 it does appear that the comparative enhancement of the signal is smaller for the SFG experiment. This can be explained by the difference in the wavelength of the two incoming beams: The 800 nm beam has a much narrower focus at the back plane of the jet (~1 μm) than the IR beam (~3 μm). This could in principle be improved by reshaping the beam size of the visible and IR beams so that they have the same size at the back plane of the jet. Nevertheless, Figure 3.4 does show that it is possible to perform SFG experiments from the surface of a liquid jet. This opens up the possibility to incorporate liquid jets in X-ray or UV resonant SFG experiments that require a vacuum environment. It also means that comparative measurements can be performed with both XPS [51] and SHG or SFG, which will be beneficial in understanding the complex chemical nature of liquid interfaces.

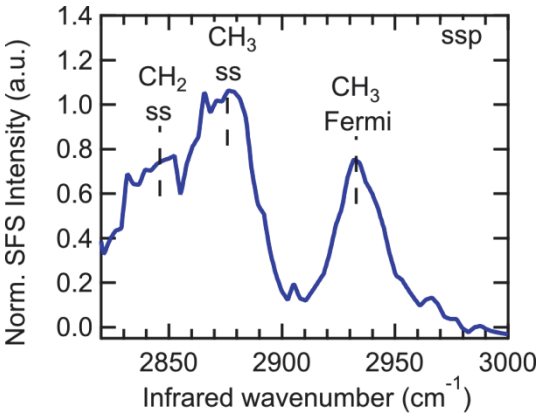

Figure 3.4. SFG spectrum from the ethanol/air interface of a 35 μm liquid jet. The spectrum was averaged for 15 minutes using SSP polarization combinations.

One possible application of SHG/SFG on a liquid microjet is to study the kinetics of adsorption on a gas/liquid interface, similar to studies with an overflowing cylinder [46-49]. Measurements on different vertical positions can be used here but are limited by the stability of the laminar part of the microjet. To estimate the time resolution and duration of such a kinetic experiment we need to consider the length of the laminar part, the flow speed, and the beam size. The flow speed in our setup was 7 m/s (but can be increased up to 70 m/s). The laminar height is approximately 2 mm, which results in a time window of 28-280 μs for the flow speed range 7-70 m/s. The size of focus is

35 μm in diameter, which means we can probe time intervals of Δt=0.5-5 μs for 70 or 7 m/s respectively.

3.4 Conclusions

SFG and non-resonant SHG experiments were performed from the surface of a liquid microjet. We have measured non-resonant SHG scattering patterns from a water microjet and observe a strong enhancement of the SHG signal for certain scattering angles. We explain the enhancement by inserting the optical properties and shape of the liquid microjet in a ray optics computation that shows the fundamental beam is focused on the back side of the liquid jet (in the case that the jet and the beam have comparable dimensions). The resultant focused optical field produces SHG signal from the air/water surface that is peaked at an angle of ~ 40^{o} with respect to the optical axis. A polarization analysis shows that there is a negligible contribution of bulk processes. The power dependence shows that even up to very high laser powers the process remains second-order in nature, which is undoubtedly caused by the high refreshment rate of the jet surface. SFG experiments from the surface of a liquid microjet of ethanol in air show that it is also possible to measure the coherent vibrational spectrum of the ethanol/air interface in this way. In the future, it should be possible to use liquid jets to perform far-UV or X-ray based nonlinear optical surface experiments [65]. In addition, combined XPS/SHG/SFG measurements are feasible which will be very useful in understanding molecular foundations of electrostatic and chemical surface properties and phenomena.

3.5 References

1. Ball, P., *Water as an Active Constituent in Cell Biology.* Chem. Rev., 2007. **108**(1): p. 74-108.
2. Thirumalai, D., G. Reddy, and J.E. Straub, *Role of Water in Protein Aggregation and Amyloid Polymorphism.* Acc. Chem. Res., 2011. **45**(1): p. 83-92.
3. Berkowitz, M.L., D.L. Bostick, and S. Pandit, *Aqueous Solutions next to Phospholipid Membrane Surfaces: Insights from Simulations.* Chem. Rev., 2006. **106**(4): p. 1527-1539.
4. Milhaud, J., *New insights into water–phospholipid model membrane interactions.* BBA - Biomembranes, 2004. **1663**(1–2): p. 19-51.
5. Jung, Y. and R.A. Marcus, *On the Theory of Organic Catalysis "on Water".* J. Am. Chem. Soc., 2007. **129**(17): p. 5492-5502.
6. Butler, R.N. and A.G. Coyne, *Water: Nature's Reaction Enforcer—Comparative Effects for Organic Synthesis "In-Water" and "On-Water".* Chem. Rev., 2010. **110**(10): p. 6302-6337.
7. Buszek, R.J., J.S. Francisco, and J.M. Anglada, *Water effects on atmospheric reactions.* Int. Rev. Phys. Chem., 2011. **30**(3): p. 335-369.
8. Solans, C., et al., *Nano-emulsions.* Curr. Opin. Colloid Interface Sci., 2005. **10**(3–4): p. 102-110.
9. Brown, F. and M. Matsuoka, *Effect of Adsorbed Surface Layers on Second-Harmonic Light from Silver.* Phys. Rev., 1969. **185**(3): p. 985-987.
10. Guyot-Sionnest, P., et al., *Vibrational spectroscopy of a silane monolayer at air/solid and liquid/solid interfaces using sum-frequency generation.* Chem. Phys. Lett., 1988. **144**(1): p. 1-5.
11. Hunt, J.H., P. Guyot-Sionnest, and Y.R. Shen, *Observation of C-H stretch vibrations of monolayers of molecules optical sum-frequency generation.* Chem. Phys. Lett., 1987. **133**(3): p. 189-192.
12. Harris, A.L., et al., *Monolayer vibrational spectroscopy by infrared-visible sum generation at metal and semiconductor surfaces.* Chem. Phys. Lett., 1987. **141**(4): p. 350-356.
13. Butcher, P. and D. Cotter, *The Elements of Nonlinear Optics* 1990: Cambridge University Press.
14. Roke, S., *Nonlinear Optical Spectroscopy of Soft Matter Interfaces.* Chem. Phys. Chem., 2009. **10**(9-10): p. 1380-1388.
15. Lambert, A.G., P.B. Davies, and D.J. Neivandt, *Implementing the Theory of Sum Frequency Generation Vibrational Spectroscopy: A Tutorial Review.* Appl. Spectrosc. Rev., 2005. **40**(2): p. 103-145.

16. Eisenthal, K.B., *Liquid Interfaces Probed by Second-Harmonic and Sum-Frequency Spectroscopy.* Chem. Rev., 1996. **96**(4): p. 1343-1360.
17. Richmond, G., *Structure and bonding of molecules at aqueous surfaces.* Annu. Rev. Phys. Chem., 2001. **52**(1): p. 357-389.
18. Richmond, G.L., *Molecular Bonding and Interactions at Aqueous Surfaces as Probed by Vibrational Sum Frequency Spectroscopy.* Chem. Rev., 2002. **102**(8): p. 2693-2724.
19. Simpson, G.J., *Molecular Origins of the Remarkable Chiral Sensitivity of Second-Order Nonlinear Optics.* Chem. Phys. Chem., 2004. **5**(9): p. 1301-1310.
20. Belkin, M.A. and Y.R. Shen, *Non-linear optical spectroscopy as a novel probe for molecular chirality.* Int. Rev. Phys. Chem., 2005. **24**(2): p. 257-299.
21. Shultz, M.J., et al., *Sum frequency generation spectroscopy of the aqueous interface: Ionic and soluble molecular solutions.* Int. Rev. Phys. Chem., 2000. **19**(1): p. 123-153.
22. Bloembergen, N., *Surface nonlinear optics: a historical overview.* Appl Phys B, 1999. **68**(3): p. 289-293.
23. Bain, C.D., *Sum-frequency vibrational spectroscopy of the solid/liquid interface.* J. Chem. Soc. Faraday T., 1995. **91**(9): p. 1281-1296.
24. Chen, Z., Y.R. Shen, and G.A. Somorjai, *Studies of polymer surfaces by sum frequency generation vibrational spectroscopy.* Annu. Rev. Phys. Chem., 2002. **53**(1): p. 437-465.
25. Arnolds, H. and M. Bonn, *Ultrafast surface vibrational dynamics.* Surf. Sci. Rep., 2010. **65**(2): p. 45-66.
26. Shen, Y.R., *A few selected applications of surface nonlinear optical spectroscopy.* Proc. Natl. Acad. Sci., 1996. **93**(22): p. 12104-12111.
27. Reider, G.A. and T.F. Heinz, *Chapter 9 - Second-order nonlinear optical effects at surfaces and interfaces: recent advances*, in *Photonic Probes of Surfaces*, P. Halevi, Editor 1995, Elsevier: Amsterdam. p. 413-478.
28. Roke, S. and G. Gonella, *Nonlinear Light Scattering and Spectroscopy of Particles and Droplets in Liquids.* Annu. Rev. Phys. Chem., 2012. **63**(1): p. 353-378.
29. Eisenthal, K.B., *Second Harmonic Spectroscopy of Aqueous Nano- and Microparticle Interfaces.* Chem. Rev., 2006. **106**(4): p. 1462-1477.
30. Scheu, R., et al., *Stern Layer Formation Induced by Hydrophobic Interactions: A Molecular Level Study.* J. Am. Chem. Soc., 2013. **135**(51): p. 19330-19335.
31. de Aguiar, H.B., J.-S. Samson, and S. Roke, *Probing nanoscopic droplet interfaces in aqueous solution with vibrational sum-frequency scattering: A study of the effects of path length, droplet density and pulse energy.* Chem. Phys. Lett., 2011. **512**(1–3): p. 76-80.
32. Jordan, I., et al., *Non-uniform spatial distribution of tin oxide (SnO2) nanoparticles at the air-water interface.* Chem. Commun., 2014. **50**(32): p. 4242-4244.

33. Brown, M.A., et al., *Effect of Surface Charge Density on the Affinity of Oxide Nanoparticles for the Vapor–Water Interface.* Langmuir, 2013. **29**(16): p. 5023-5029.
34. Gonella, G. and H.-L. Dai, *Second Harmonic Light Scattering from the Surface of Colloidal Objects: Theory and Applications.* Langmuir, 2013. **30**(10): p. 2588-2599.
35. Jen, S.-H., G. Gonella, and H.-L. Dai, *The Effect of Particle Size in Second Harmonic Generation from the Surface of Spherical Colloidal Particles. I: Experimental Observations†.* J. Phys. Chem. A, 2009. **113**(16): p. 4758-4762.
36. Wang, H., et al., *In Situ, Nonlinear Optical Probe of Surfactant Adsorption on the Surface of Microparticles in Colloids.* Langmuir, 2000. **16**(6): p. 2475-2481.
37. Castro, A., S. Ong, and K.B. Eisenthal, *Studies of molecular properties at the surface of a liquid jet by second harmonic generation.* Chem. Phys. Lett., 1989. **163**(4–5): p. 412-416.
38. Tokimoto, T., S. Tsukahara, and H. Watarai, *Lactone Cleavage Reaction Kinetics of Rhodamine Dye at Liquid/Liquid Interfaces Studied by Micro-Two-Phase Sheath Flow/Two-Photon Excitation Fluorescence Microscopy.* Langmuir, 2005. **21**(4): p. 1299-1304.
39. Tokimoto, T., S. Tsukahara, and H. Watarai, *Microscopic Fluorescence Measurement of Fast Interfacial Complexation by Two-Phase Sheath Flow Method.* Chem. Lett., 2001. **30**(3): p. 204-205.
40. Faubel, M., et al., *Ultrafast Soft X-ray Photoelectron Spectroscopy at Liquid Water Microjets.* Acc. Chem. Res., 2011. **45**(1): p. 120-130.
41. Lange, K.M., et al., *X-ray emission from pure and dilute H2O and D2O in a liquid microjet: Hydrogen bonds and nuclear dynamics.* Phys. Rev. B, 2012. **85**(15): p. 155104.
42. Wilson, K.R., et al., *X-ray Spectroscopy of Liquid Water Microjets.* J. Phys. Chem. B, 2001. **105**(17): p. 3346-3349.
43. Brown, M.A., et al., *Changes in the Silanol Protonation State Measured In Situ at the Silica–Aqueous Interface.* J, Phys. Chem. Lett., 2012. **3**(2): p. 231-235.
44. Brown, M.A., et al., *In situ photoelectron spectroscopy at the liquid/nanoparticle interface.* Surf. Sci., 2013. **610**(0): p. 1-6.
45. Sellberg, J.A., et al., *Ultrafast X-ray probing of water structure below the homogeneous ice nucleation temperature.* Nature, 2014. **510**(7505): p. 381-384.
46. Colegate, D.M. and C.D. Bain, *Adsorption Kinetics in Micellar Solutions of Nonionic Surfactants.* Phys. Rev. Lett., 2005. **95**(19): p. 198302.
47. Campbell, R.A., P.A. Ash, and C.D. Bain, *Dynamics of Adsorption of an Oppositely Charged Polymer−Surfactant Mixture at the Air−Water Interface: Poly(dimethyldiallylammonium chloride) and Sodium Dodecyl Sulfate.* Langmuir, 2007. **23**(6): p. 3242-3253.

48. Angus-Smyth, A., R.A. Campbell, and C.D. Bain, *Dynamic Adsorption of Weakly Interacting Polymer/Surfactant Mixtures at the Air/Water Interface.* Langmuir, 2012. **28**(34): p. 12479-12492.
49. Yan, C., A. Angus-Smyth, and C.D. Bain, *Adsorption kinetics of non-ionic surfactants in micellar solutions: effects of added charge.* Faraday Discuss., 2013. **160**(0): p. 45-61.
50. Lis, D., et al., *Liquid flow along a solid surface reversibly alters interfacial chemistry.* Science, 2014. **344**(6188): p. 1138-1142.
51. Brown, M.A., et al., *Measure of Surface Potential at the Aqueous–Oxide Nanoparticle Interface by XPS from a Liquid Microjet.* Nano Lett., 2013. **13**(11): p. 5403-5407.
52. Brown, M.A., et al., *Electronic Structures of Formic Acid (HCOOH) and Formate (HCOO–) in Aqueous Solutions.* J, Phys. Chem. Lett., 2012. **3**(13): p. 1754-1759.
53. Brown, M.A., et al., *Electronic structure of sub-10 nm colloidal silica nanoparticles measured by in situphotoelectron spectroscopy at the aqueous-solid interface.* Phys. Chem. Chem. Phys., 2011. **13**(28): p. 12720-12723.
54. Terhune, R.W., P.D. Maker, and C.M. Savage, *Measurements of Nonlinear Light Scattering.* Phys. Rev. Lett., 1965. **14**(17): p. 681-684.
55. Bersohn, R., Y.H. Pao, and H.L. Frisch, *Double-Quantum Light Scattering by Molecules.* J. Chem. Phys., 1966. **45**(9): p. 3184-3198.
56. Schürer, B., et al., *Probing colloidal interfaces by angle-resolved second harmonic light scattering.* Physical Review B, 2010. **82**(24): p. 241404.
57. Gomopoulos, N., et al., *Label-free second harmonic and hyper Rayleigh scattering with high efficiency.* Opt. Express, 2013. **21**(1): p. 815-821.
58. Harrington, R.F., *Time-Harmonic Electromagnetic Fields* 2001, Piscataway, NJ: IEEE Press.
59. Rohrbach, A. and W. Singer, *Scattering of a scalar field at dielectric surfaces by Born series expansion.* J. Opt. Soc. Am. A, 1998. **15**(10): p. 2651-2659.
60. de Beer, A.G.F. and S. Roke, *Nonlinear Mie theory for second-harmonic and sum-frequency scattering.* Phys. Rev. B, 2009. **79**(15): p. 155420.
61. Pyatt, R.D. and D.P. Shelton, *Hyper-Rayleigh scattering from CH4,CD4,CF4, and CCl4.* J. Chem. Phys., 2001. **114**(22): p. 9938-9946.
62. Backus, E.H.G., et al., *Laser-Heating-Induced Displacement of Surfactants on the Water Surface.* J. Phys. Chem. B, 2012. **116**(9): p. 2703-2712.
63. Velarde, L. and H.-F. Wang, *Unified treatment and measurement of the spectral resolution and temporal effects in frequency-resolved sum-frequency generation vibrational spectroscopy (SFG-VS).* Phys. Chem. Chem. Phys., 2013. **15**(46): p. 19970-19984.

64. Wang, H.-F., et al., *Quantitative spectral and orientational analysis in surface sum frequency generation vibrational spectroscopy (SFG-VS).* Int. Rev. Phys. Chem., 2005. **24**(2): p. 191-256.

65. Glover, T.E., et al., *X-ray and optical wave mixing.* Nature, 2012. **488**(7413): p. 603-608.

Chapter 4: The interfacial structure of water droplets in a hydrophobic liquid

Nanoscopic and microscopic water droplets and ice crystals embedded in liquid hydrophobic surroundings are key components of aerosols, rocks, oil fields and the human body. The chemical properties of such droplets critically depend on the interfacial structure of the water droplet. We report the surface structure of 200 nm sized water droplets in mixtures of hydrophobic oils and surfactants as obtained from vibrational sum frequency scattering measurements. The interface of a water droplet shows significantly stronger H-bonds than the air/water or hexane/water interface and previously reported planar liquid hydrophobic/water interfaces at room temperature. The observed spectral difference is similar to that of a planar air/water surface at a temperature that is ~50 K lower. Supercooling the droplets to 263 K does not change the surface structure. Below the homogeneous ice nucleation temperature a single vibrational mode is present with a similar mean H-bond strength as for a planar ice/air interface.

This chapter is based on the paper by Nikolay Smolentsev, Wilbert Smit, Huib Bakker, and Sylvie Roke "The interfacial structure of water droplets in a hydrophobic liquid" published in Nature Communications, 2017, 8, 15548.

4.1 Introduction

Aqueous hydrophobic interfaces play a defining role on nano- and microscopic length scales. Pockets and droplets of water in a hydrophobic environment are omnipresent in the atmosphere (as ice particles and cloud droplets [1]), the earth [2, 3] (in oil fields and inside internal pores of many geological materials), and in chemical [4, 5] and biological processes [6-8] (as vehicles for medicine delivery [9]). For all of these processes the nanoscopic water droplet/hydrophobic interface plays a critical role in determining the fate of the system. The reactivity of confined water is crucial for atmospheric science [1], earth science [3] and biology [10]. The molecular surface properties of water droplets are commonly inferred from data obtained from the macroscopic air/water interface [11-16] or from aqueous solutions of solvated hydrophobes [17], systems that are very different in both their size, chemical composition and temperature dependence from actual droplet surfaces. As such, the surface structure and reactivity of water droplets and confined water remains elusive, despite its relevance.

Here, we present temperature controlled sum frequency scattering experiments on nanoscopic water droplets in a liquid hydrophobic environment. We find that compared to planar water/air or water/hexane interfaces the spectrum reveals a greater order corresponding to that of a planar water surface at a ~50 K or 40 K lower temperature. This increase in order is explained by the formation of an extended hydrophobic network, which does not exist on planar interfaces and in solution. In addition, upon supercooling the droplets, the surface spectrum does not change shape. Cooling the water droplets below the homogeneous ice nucleation temperature results in a spectrum with a single symmetric peak that is similar to the one found for the basal ice/air interface.

4.2 Methods

Chemicals. Prior to use all glassware was cleaned with a 1:3 H_2O_2:H_2SO_4 solution, after which it was thoroughly rinsed with ultra-pure water (H_2O, Milli-Q UF plus, Millipore, Inc., electrical resistance of 18.2 MΩ cm). Hexadecane (Fluka, 99.8%), decane (Fluka, 99.8%), cyclohexane (Sigma, >99.7%), Span80 (Sigma, GC quality), Tween80 (Sigma, GC quality), sodium dodecyl sulfate, SDS (99% BioMol), d_{34}-hexadecane ($C_{16}D_{34}$, 98% d, Cambridge Isotope Laboratories), fluorinated oil (Novec HFE7500, 3-Ethoxy-dodecafluor-2-trifluormethyl-hexan), sulfuric acid (95-97%, ISO, Merck), H_2O_2 (30%, Reactolab SA) were used as received. The purity of alkanes was verified with a Zisman test [18, 19]. All samples for SFS measurements were prepared using D_2O (99.8% Armar, >2 MΩ cm). The D_2O for the water/air SFG experiment is obtained from Cambridge Isotope Laboratories (99.9%).

Water nanodroplets were prepared using a sonication procedure with 1 v.v.% D_2O in oil concentration and 5 mM Span80 (or Span80:Tween80 mixture), according to the procedure described in Ref. [20]. For some samples 10 mM SDS was added to the water phase before the emulsification. For all samples the droplets have a mean diameter of ~200 nm with a polydispersity index (PDI) of ~0.2.

Monocrystalline ice was grown following the manual of Basu et al.[21]. Five pieces of a PVC pipe with small notches at the bottom were placed in an aluminum pan which was chilled from underneath with a cooling liquid. Millipore water (18.2 MΩ cm) was degassed and added until the bottoms of the molds were covered. The temperature in the pan was set to -0.5°C and after equilibration ice nucleation was initiated by adding a small piece of ice to the middle of the pan. The small notches at the bottom of each PVC mold allow only one ice crystal to propagate through, resulting in a single ice crystal in each mold. For three subsequent days, 1 cm water was added to each mold and the temperature was lowered by 0.3°C. At day four, the ice was pushed outside of the pipe pieces and stored in a freezer, where all further handling was done. The crystal orientation was determined using a Rigsby-type universal stage [22] and cut to the basal plane with a band saw. The ice surface was polished by a microtome and a 4 mm thick slice was cut off for the experiment.

Vibrational sum frequency reflection mode spectra were recorded in the SSP polarization combination using the experimental setup described in Ref. [23]. The setup was purged with N_2 gas. The VIS beam with a pulse energy of 14 μJ was centered at 798.6 nm with a FWHM bandwidth of 13 cm^{-1}. The D_2O/air measurements were performed with the 10 μJ 300 cm^{-1} FWHM IR beam centered at a wavelength of 4 μm. The procedure for measuring hexane/water is given in Ref [23]. To measure the water/Span80 interface 0.16 μM Span80 was dissolved in 0.1 mL hexane and added to liquid D_2O. Subsequently, the hexane was evaporated off. The diameter of the teflon tray for this experiment was 3.5 cm. The basal ice/air measurements were performed with a 3 μJ 550 cm^{-1} FWHM IR beam centered at 3 μm. The angles of incidence with respect to the surface normal were 35° (VIS) and 40° (IR). The D_2O/air and basal ice spectra were recorded with acquisition times of 30 s and 300 s respectively. The spectral intensities were baseline subtracted and normalized with the IR and VIS pulse energies, and the (normalized) SFG spectrum recorded from z-cut quartz.

The ice measurements were performed using a temperature cell that was cooled with liquid N_2 and equipped with a CaF_2 window. The temperature was monitored by a thermocouple welded on the edge of the ice surface with a drop of water and the desired temperature was set by a heating foil resistance, covered by a copper plate.

Spectral shape and IR absorption. The scattered SF spectra recorded from the water droplets were baseline subtracted and summed to obtain the spectral intensity for the entire spectral region of the OD stretching mode. The resulting spectrum was then divided by the energies of the IR and VIS beams and normalized to the summed SFG spectrum of a z-cut quartz crystal. Since SF scattering experiments are performed in transmission mode we have to take into account that the oil phase is absorbing part of the IR spectrum, leading to a transmission spectrum μ_{FTIR}. To correct for absorption effects we divide the obtained SFS spectrum by an FTIR transmittance spectrum measured from the same sample in the same cuvette. Figure 4.1 shows the results of this correction as the blue spectra. It can be seen that this procedure results in significant spectral changes in the red spectral side since here the SFG spectrum overlaps with the CD modes of the deuterated main phase (d_{34}-hexadecane). The CH modes in the SFS spectrum originate from the Span80 molecules that are present on the oil side of the interface (Span80 is insoluble in water [24]).

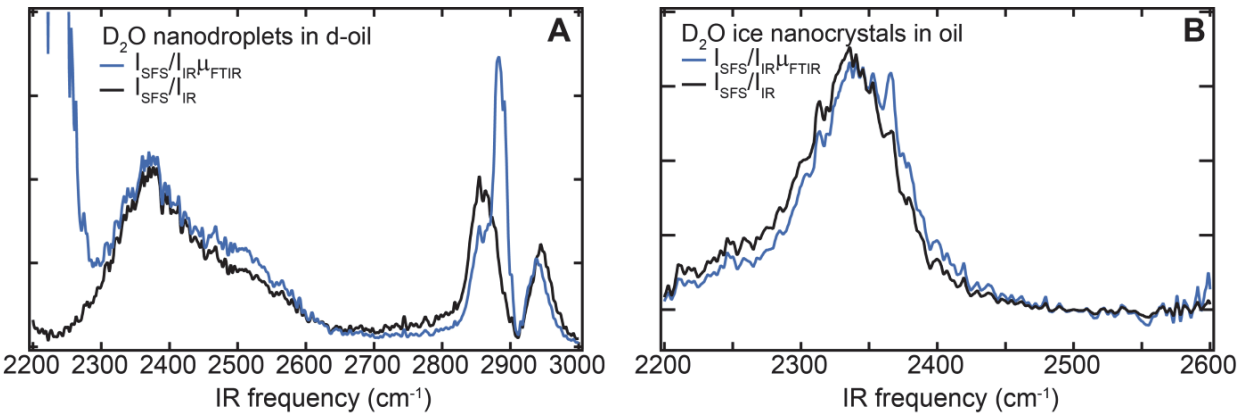

Figure 4.1. Normalization procedure. The SFS spectra of water droplets in the hydrophobic solvent (A) and frozen ice nanocrystals (B) with (blue) and without (black) correction with the FTIR spectrum.

Discontinuity in the interfacial electric fields. Frequency dependent refraction modifies the incident electromagnetic field at the interface, which can lead to significant frequency dependent distortions in the obtained water spectra [25, 26]. The sum frequency reflection mode spectra are therefore divided by the Fresnel factors [14], whereby we use the refractive indices of D_2O and ice from Refs. [27-29]. The effective refractive index of the interfacial layers is calculated using a simple slab model [30]. For linear light scattering experiments such effects are captured by linear Mie theory [31] and thus for sum frequency scattering experiments by nonlinear Mie theory [32]. Using nonlinear Mie theory, we calculated a frequency dependent correction factor for the SFS spectra using the input parameters fromTable 4.1. The refractive index values for oil and D_2O are taken from Refs. [33, 34]. Figure 4.2 shows the effects of the correction on the spectral data reported below, where it can be seen that the influence of refraction effects is minimal. The reason

for the small difference is that the droplets are small compared to the wavelength. For simplicity, in the text below we refer to the corrected SFS intensity $I_{SFS}/I_{IR}\mu_{FTIR}$ as Normalized SFS Intensity.

Parameter	Value
Opening angle between IR/VIS beams	15°
Scattering angle in the oil phase	45°
Number of expansion terms in the numerical algorithm	10
Effective orientation angle of the water molecules as represented by a δ distribution	39.2°
Non-zero independent $\beta^{(2)}$ components and their relative values [35, 36]	β_{ccc}=1; β_{aac}=0.92
Particle diameter	200 nm
Polarization combination (SF,VIS,IR)	SSP

Table 4.1. Parameters used for the nonlinear Mie calculation to correct the SFS spectra of D_2O droplets in oil for changes in the amplitude of the electromagnetic fields as they cross the droplet interface.

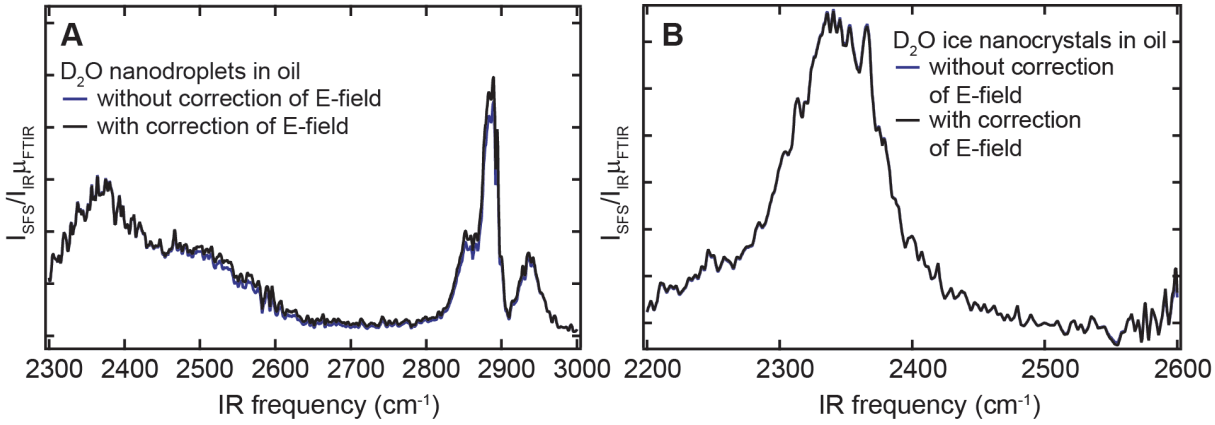

Figure 4.2. Discontinuity in the interfacial electric fields. Comparison of normalized SFS spectra ($I_{SFS}/I_{IR}\mu_{FTIR}$) with (black) and without (blue) nonlinear Mie correction for D_2O droplets in d_{34}-hexadecane at room temperature (A) and D_2O ice nanocrystals in a decane:cyclohexane mixture (B).

4.3 Results and discussion

Nanoscopic (100 nm radius) water droplets are prepared via sonication in d_{34}-hexadecane (Figure 4.3) or in a 1:1 mixture of decane and cyclohexane (Figure 4.5), both with 5 mM of a hydrophobic surfactant molecule that partially covers the interface (Span80, Figure 4.3A). The water-hexadecane partitioning coefficient for these hydrophobic liquids is 5.5×10^{-4} (Span80 [24]), $>1.6\times10^{-6}$ (decane), and 1.6×10^{-4} (cyclohexane) [37], providing a liquid hydrophobic/water interface in all systems. The interfacial structure of the water droplets and ice nanocrystals is measured with vibrational sum frequency scattering (SFS) [38, 39], a method that combines interface specific sum frequency generation (SFG) [11, 12, 14, 15, 40, 41] with light scattering [42] (illustrated in Figure 4.3B). The scattered vibrational spectra report on the average orientational order and H-bond network structure of water molecules in the first few monolayers of water at the interfacial region [39].

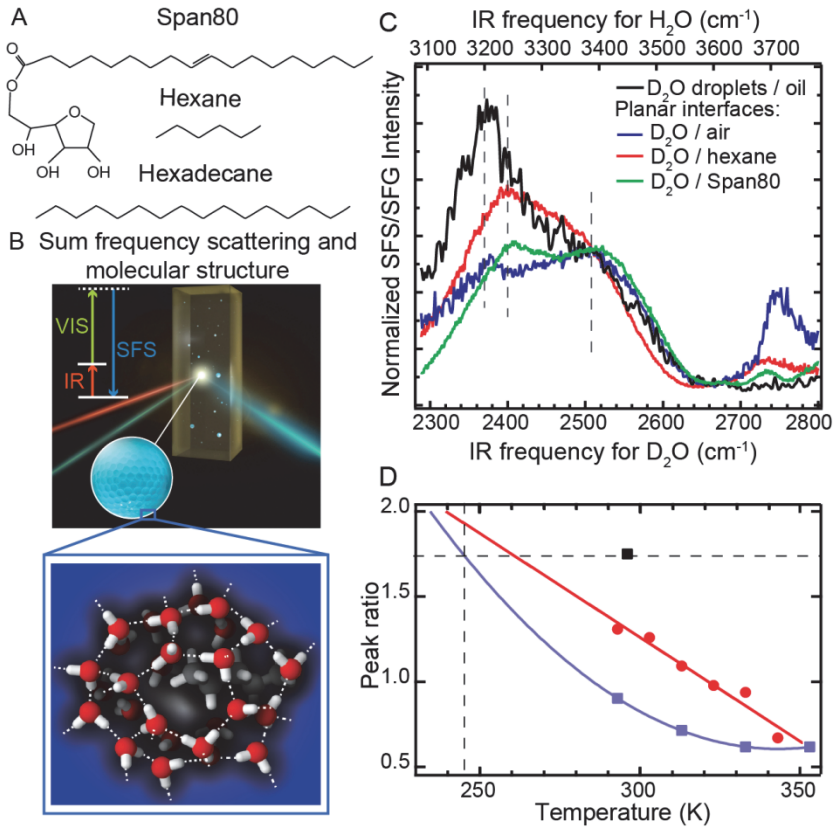

Figure 4.3. Surface structure of water droplets. A: Chemical structure of hexadecane, hexane and Span80 B. Illustration of a vibrational sum frequency scattering experiment. A femtosecond infrared (IR) and a picosecond visible (VIS) laser beam overlap in space and time in the sample and generate scattered sum frequency light from the water droplets. The inset illustrates the surface hydrogen-bond structure of a water droplet embedded in a hydrophobic liquid. In this figure we sketch a possible molecular arrangement of the water molecules at the surface of a droplet surrounding an alkane tail that protrudes into the water phase (looking from the inside of the droplet). Please note that the surfactant is not present in the illustration. C SFS spectra of D_2O droplets in d_{34}-hexadecane with 5 mM Span80 (black) and reflection SFG spectra of the planar D_2O/air interface (blue), D_2O/Span80 interface (green) and planar D_2O/hexane interface (red). The SFS/SFG spectra are collected with horizontally (P) polarized IR and vertically polarized (S) VIS and SF beams. The normalization procedure takes into account the IR pulse shape in the sample as well as discontinuities of the electromagnetic fields at the interface (see Methods). The top axis shows the corresponding frequencies axis for H_2O (×1.35 [15]). D. The ratio between the low and high frequency bands of the SFG spectrum of the planar water/air and water/hexane interface [23] (blue and red markers) and an extrapolation with a quadratic polynomial fit to a lower temperature range (blue and red lines). The ratio for the room temperature water nanodroplet spectrum is shown as a black marker.

Figure 4.3 C shows the scattered SF spectrum of D_2O nanodroplets in oil (296 K) and reflection SFG spectra of a planar liquid D_2O/air and a planar D_2O/hexane interface. The spectra were normalized taking into account linear absorption effects as well as discontinuities in the normal component of the electromagnetic fields as they cross the droplet interface (see Methods section). The SFG spectra of the two planar interfaces of Figure 4.3C have three main features: A peak at 2370 / 2400 cm^{-1}, a peak at 2500 cm^{-1}, and a peak at 2745 / 2725 cm^{-1}. The frequency of the OD stretching vibrations is correlated to the strength of the interfacial H-bond interaction: the

OD frequency decreases with increasing H-bond strength. Hence, the feature at 2500 cm^{-1} reports on water molecules that are more weakly H-bonded than the ones that attribute to the feature at 2370 / 2400 cm^{-1}. The peak at 2745 / 2725 cm^{-1} originates from interfacial OD bonds that are not H-bonded [43]. The 296 K droplet/hydrophobic interface spectrum contains the same 2370 cm^{-1} and 2500 cm^{-1} features (indicated by the dotted lines), but the higher frequency components are significantly less intense than they are in the planar interface spectra. This indicates that there are relatively more strongly H-bonded water molecules at the water droplet interface than at the air/water and hexane/water interface recorded at the same temperature. The SFG spectrum of the Span80/water interface is similar to that of D_2O/hexane and D_2O/air and shown in Figure 4.3.

The peak ratio of the 2370 cm^{-1} and 2500 cm^{-1} modes is temperature dependent. This temperature dependent ratio is plotted in Figure 4.3D for the air/water and hexane/water interfaces. Lowering the temperature increases [23] the ratio, indicating that the population of stronger H-bonds increases over that of weaker H-bonds. The peak ratio obtained for the water droplets is also plotted (black marker). Extrapolating the ratios found for the air/water and hexane/water spectra (blue and red lines) the same ratio as for the water droplets would be found at a hypothetical planar water/air or water/hexane interface of ~245 / 260 K (that is, ~50 / 40 K colder). Thus, the water molecules of the water droplet/hydrophobic interface appear to be much more structured than the water molecules at a planar water/air or water/hexane interface. Note that this conclusion was arrived at by comparing amplitudes at particular frequencies. The spectrum of water is known to be highly complex, involving strong inhomogeneous broadening [44, 45], excitonic coupling effects [46], and a Fermi resonance with the overtone of the bending vibration [47]. As such, aside from the feature that high frequency modes generally refer to more weakly H-bonded water molecules than low frequency modes, there are many ways to interpret the spectral information [15, 16, 23, 43, 45, 48-52]. Our analysis addresses the temperature dependence of the ratio of weakly and strongly H-bonded water molecules, and is as such quite model independent.

Very similar SFS spectra are obtained for other combinations of hydrophobic oils (mixtures of decane and cyclohexane, fluorinated oil) and surfactants (Tween80, tri-block PEG 900, Figure 4.4), which indicates that the observed red-shift of the spectrum is a common phenomenon for water droplets in various hydrophobic liquids. The absence of unbonded OD groups in the droplet spectrum can be partially explained by the presence of OH groups on the Span80 molecule that can form H-bonds with interfacial water molecules that would otherwise be unbonded (see Appendix). As a result, the peak at 2745 cm^{-1}, corresponding to OD groups that are not H-bonded, vanishes. From the detection limit of the SFS system [53], it follows that the imbalance between OD groups that point in or out of the water droplet surface is less than 1 free OD group per 27 nm^2. The difference with the droplet spectrum probably arises from a difference in structure, which we

will discuss in more detail further on. Note that impurities are not expected to be a problem here [53] as the sample volume is small (~50 μL), and the surface to volume ratio is large (~10^5 cm^{-1}; which is at least three orders of magnitude larger than in standard planar reflection SFG measurements).

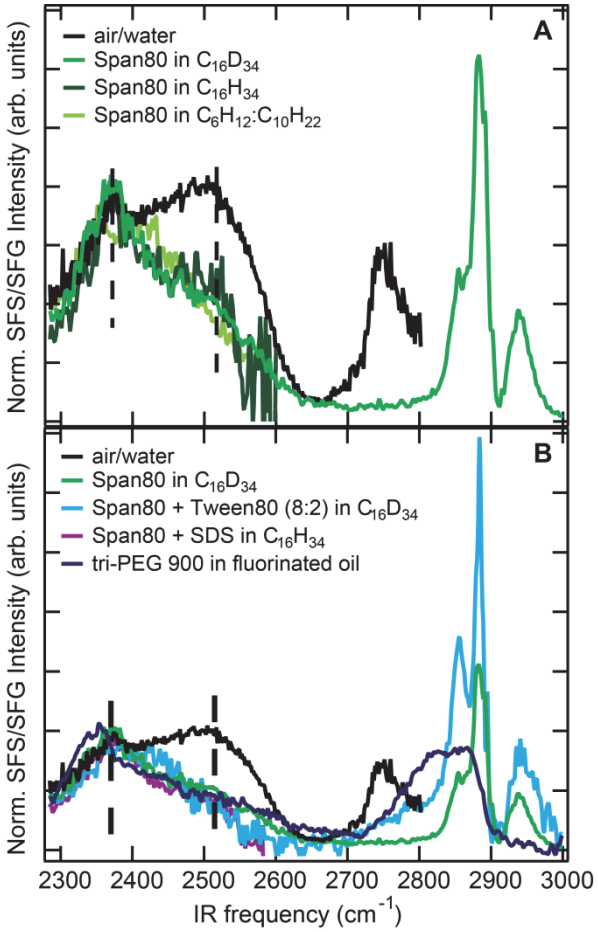

Figure 4.4. Additional SFS data. SFS data for water droplets in different solvents (A): D_2O droplets in hydrogenated hexadecane (dark green) and deuterated hexadecane (green) and D_2O droplets in a mixture of cyclohexane and decane (light green). The concentration of D_2O was 1% and emulsions were stabilized with 5 mM Span80. The spectra are very similar to the one reported in Figure 4.3 C. SFS data for stabilized water droplets stabilized with with different surfactants (B): 5 mM Span80 mixture in deuterated hexadecane (green), a 5 mM mixture of 84:16 weight fraction Span80:Tween80 in deuterated hexadecane (cyan), and a mixture of 10 mM SDS with 5 mM Span80 (purple). The addition of both anionic (SDS) and hydrophilic non-ionic surfactants (Tween80) does not result in significant changes of the SFS spectrum. Changing both the oil and the surfactant, using D_2O droplets prepared in HFE7500 fluorinated oil stabilized with a triblock PEG-900 surfactant (dark blue) also yields a similar spectrum. Aqueous micro-sized drops dispersed in a perfluorinated oil, HFE-7500 (3M, USA), containing 1 wt% of a triblock co-polymer surfactant were produced according to the protocol in [54]. Air/water planar SFG spectrum is shown in black.

Next, we repeat the experiment at reduced temperatures, supercooling the droplets (Figure 4.5A) and ultimately freezing them by cooling below the homogeneous nucleation point of D_2O (237 K [55], Figure 4.5B). Figure 4.5A shows SFS spectra recorded at different temperatures

(296 K, red, 273 K, green, and 263 K, blue) using a mixture of decane and cyclohexane as the main phase. The droplet spectrum from Figure 4.3C is also shown (black line). It can be seen that despite the different hydrophobic phase the water spectrum does not show a significant difference. In addition, reducing the liquid temperature below 273 K does not result in any spectral changes. Figure 4.5B shows the SF spectrum of D_2O nanocrystals (233 K) and the ice/air interface for different temperatures (170 K, 200 K, and 230 K) in the frequency range around the strongly H-bonded mode at ~2350 (3170) cm^{-1}. The resonance in the SF spectrum of the ice nanocrystals has a similar frequency as is observed for the planar ice surface of the same temperature. This indicates that the difference in surface structure observed for the liquid interface is not present in the solid phase.

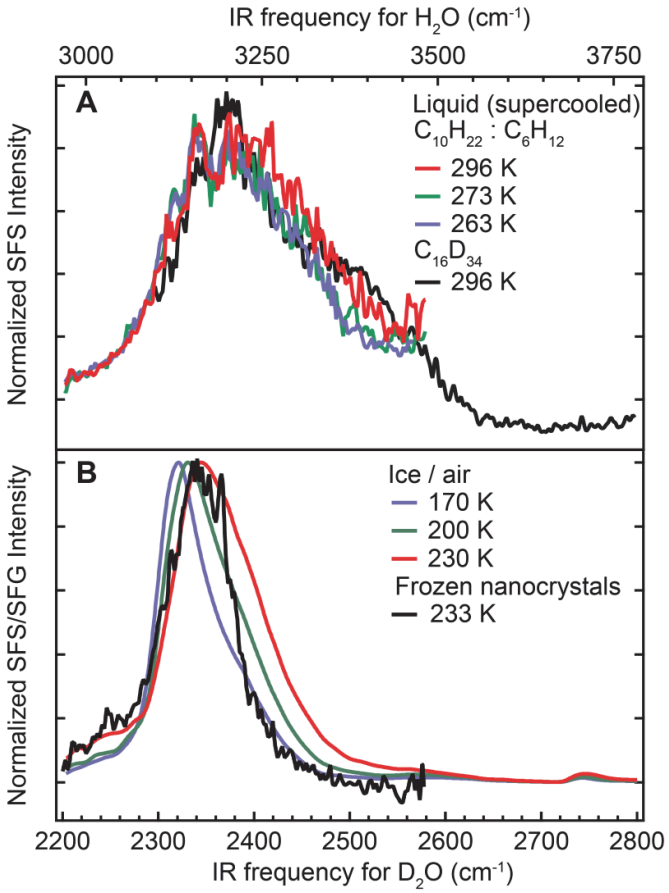

Figure 4.5. Supercooled water droplets and ice nanocrystals. A. SFS spectra of D_2O droplets at room temperature (296 K, in a mixture of decane and cyclohexane (red) and in d_{34}-hexadecane (black)) and under supercooled conditions (green, 273 K and blue, 263 K, both in a mixture of decane and cyclohexane). B. SFS spectra of D_2O droplets at 233 K, below the homogeneous ice nucleation temperature (black) and SFG spectra of the basal H_2O/air interface at 170 K (blue), 200 K (green) and 230 K (red). All droplets samples contain 5 mM Span80. Spectral data from H_2O and D_2O are interchangeable [15]. Frequency conversion between H_2O and D_2O was obtained by multiplying the D_2O frequencies by 1.35 [15]. The SFG spectra are collected with horizontally polarized IR and vertically polarized VIS and SF beams.

The absence of the effect for the frozen droplets can be understood from the fact that when the droplets freeze, the mutual water-water interactions become relatively more important for the

resulting water SFG spectrum (and the detected H-bond strength) than the interactions with the hydrophobic oil molecules. For crystalline planar ice, the observed SF ice/air spectrum originates in part from OH groups connecting the different layers in the ice crystal [56]. These deeper layers of water molecules are much less influenced by the hydrophobic groups at the interface. Hence, for planar ice and frozen water droplets of the same temperature the H-bonds of the probed OH groups are of similar strength.

Thermodynamic [57, 58] and Raman MCR measurements on solvated alkanols [17] show water molecules hydrating a hydrophobic solute are more tetrahedrally ordered and thus more constrained in configurational space than water molecules in bulk liquid water (as sketched in the inset of Figure 4.3B). These solutes are very small and fulfill the criterion of Chandler [4] that states that hydrophobic solutes/surfaces lead to an enhancement of the tetrahedral ordering of water if the radius of the solute/surface is < 1 nm [4]. In this perspective, the present observations of an enhanced ordering of water molecules at the surface of water nanodroplets embedded in oil is perhaps surprising, as the droplet radius (100 nm) is much larger than 1 nm. However, we can consider the oil surrounding the water droplet surface as an extended curved array of hydrophobic perturbations, i.e. hydrophobic groups protruding into the surface of the water droplet. The water molecules near the hydrophobic protrusions will fold their H-bond network around these (<1 nm) protrusions. We speculate that a high density of hydrophobic protrusions in combination with a modest overall curvature of the water surface (corresponding to a diameter of a few hundred nanometers), leads to a strong structuring of the water hydrogen-bond network, resulting in an extended highly-structured corrugated droplet surface. For smaller droplets (e.g. within micelles/solutes), the surface is too strongly curved to display such a favorable interplay between short-range and long-range interactions. For larger droplets, and flat surfaces, the curvature is too weak to get such a favorable interplay, leading to local disruptions of the hydrogen-bond network and an enhanced inhomogeneity. This picture of the enhanced ordering of curved water surfaces will require support from high-quality molecular dynamics simulations.

4.4 Conclusions

In summary, vibrational sum frequency scattering spectra from 100 nm radius water droplets embedded in a hydrophobic liquid at different temperatures show that the H-bond network of the interfacial water possesses a much enhanced (in-plane) tetrahedral structure compared to a planar air/water interface. This greater order manifests itself as a red shifted spectrum that has a 100 % increased peak ratio of the 2370 cm^{-1} and 2500 cm^{-1} modes. This increase is much larger than observed in previous studies of planar liquid hydrophobic/water interfaces. The observed structure of the water droplet interface corresponds to that of an air/water interface that is ~ 50 K colder. This increase in order is explained by the formation of an extended network of hydrophobic protrusions

into the water droplet surface, which does not exist on planar interfaces and in solution. Upon supercooling the droplets, the surface spectrum does not change shape. Cooling the sample below the homogeneous ice nucleation temperature results in a spectrum with a single symmetric peak at a comparable frequency as that of a planar basal ice/air interface of the same temperature.

The presented experiments demonstrate the possibility of quantifying the interfacial structure of water droplets and illustrate the effect of nanoscopic hydrophobic surfaces on the H-bond structure of water. With a reduction of the effective 'surface temperature' we expect that the reactivity of water droplets embedded in a hydrophobic environment [59], such as in cloud droplets, atmospheric ice particles [1], rocks [3] or medicine carriers [9] is lower than what one might think based on the actual temperature. Future studies on such nanoscopic systems may reveal important information on the role and reactivity of interfacial water in aerosol formation, protein folding, pore functioning [4, 6, 7, 60] and the charging and stabilization of hydrophobic interfaces.

4.5 Appendix: Analysis of Span80 surface structure

In order to estimate the surface structure of the Span80 molecules we fitted the C-H mode region of the Span80 spectra and derived the molecular orientation from the tilt angle of the single methyl group present in the molecule. Figure 4.6A displays the SF spectrum of Span80 at the water droplet / d_{34}-hexadecane oil interface using the same polarization combination as used in the main text. The obtained fit is shown as the black line in Figure 4.6A and the fit parameters are given in Table 4.2.

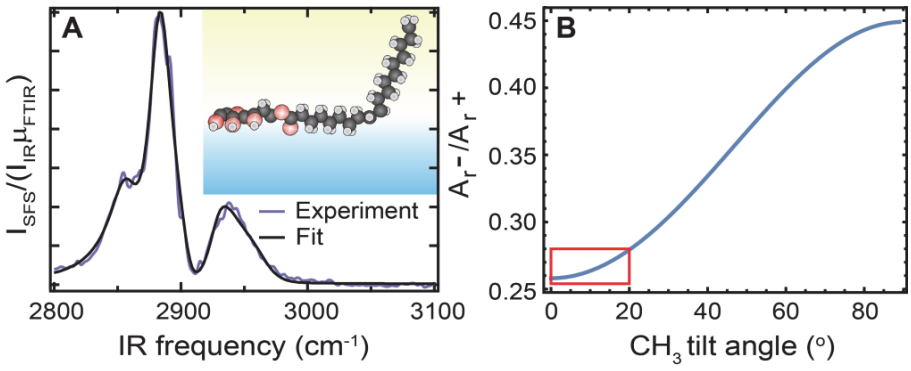

Figure 4.6. Analysis of Span80 surface structure. Experimental (blue) and fitted (black) spectra in the CH region of water droplets stabilized with Span80 in d_{34}-hexadecane. The inset shows the orientation of the Span80 molecule at the oil/water interface as discussed in the text. B: dependence of A_{r-}/ A_{r+} ratio on the tilt angle.

mode	ω_i (cm^{-1})	Υ_i (cm^{-1})	A_i
r^+	2883	11	1
d+	2857	14	0.42
d^+_{FR}	2928	14	0.45
r^-	2965	20	-0.26
d^-	2905	11	-0.25

Table 4.2. Fitted resonance frequency, amplitude, and linewidth of the SFS spectrum in the CH region of water droplets stabilized with Span80 in d_{34}-hexadecane.

To determine the average tilt angle of the CH_3 group with respect to the droplet surface normal we used the r^-/r^+ ratio amplitude ratio. The details of this analysis, as well as the used input values for the oil/water interface, are described in the Supporting Information of Ref. [61]. The r^-/r^+ scattered amplitude ratio was calculated using a hyperpolarizability ratio of $\beta^{(2)}_{aac}/\beta^{(2)}_{ccc}$ = 1.8. The result is plotted as a function of the tilt angle in Figure 4.6 B. The experimental amplitude ratio obtained from the fit to the data (blue) in Figure 4.6A is 0.27 and indicated in Figure 4.6B as a rectangle (which includes the error bar). This value translates to a methyl group tilt angle of 10°±10°, i.e. the CH_3 group is oriented approximately parallel to the surface normal. Since there are no vibrational modes present in the SFS spectrum above 3000 cm^{-1}, the unsaturated =C-H mode is likely adopting an orientation that is nearly parallel to the interfacial plane. The structure is sketched in the inset of Figure 4.6A and results in a surface that is partially covered with CD groups (from the oil phase), CH modes from the Span80, and 6(3) groups that can act as H-bond acceptors (donors) per Span80 molecule. Given the derived methyl group orientation, the H-bond acceptors and donors are likely pointing towards the water phase providing enough groups for the unbound OD water groups to H-bond with. Such a structure results in an absence of the free OD mode at 2745 cm^{-1} in Figure 4.3, Figure 4.4 and Figure 4.5.

4.6 References

1. de Leeuw, G., et al., *Production flux of sea spray aerosol.* Rev. Geophys., 2011. **49**(2): p. 1-39.
2. Putnis, A., *Why mineral interfaces matter.* Science, 2014. **343**(6178): p. 1441-1442.
3. Zachara, J., et al., *Internal domains of natural porous media revealed: critical locations for transport, storage, and chemical reaction.* Environ. Sci. Technol., 2016. **50**(6): p. 2811-2829.
4. Chandler, D., *Interfaces and the driving force of hydrophobic assembly.* Nature, 2005. **437**(7059): p. 640-647.
5. Zhang, L., et al., *Factors that determine zeolite stability in hot liquid water.* J. Am. Chem. Soc., 2015. **137**(36): p. 11810-11819.
6. Dyson, H.J., P.E. Wright, and H.A. Scheraga, *The role of hydrophobic interactions in initiation and propagation of protein folding.* Proc. Natl. Acad. Sci., 2006. **103**(35): p. 13057-13061.
7. Ball, P., *Water as an active constituent in cell biology.* Chem. Rev., 2008. **108**(1): p. 74-108.
8. Möhlmann, D.T.F., *Are nanometric films of liquid undercooled interfacial water bio-relevant?* Cryobiology, 2009. **58**(3): p. 256-261.
9. Amstad, E., S.-H. Kim, and D.A. Weitz, *Photo- and thermoresponsive polymersomes for triggered release.* Angew. Chem. Int. Ed., 2012. **51**(50): p. 12499-12503.
10. Grzybowski, B.A. and W.T.S. Huck, *The nanotechnology of life-inspired systems.* Nat. Nanotechnol., 2016. **11**(7): p. 585-592.
11. Johnson, C.M. and S. Baldelli, *Vibrational sum frequency spectroscopy studies of the influence of solutes and phospholipids at vapor/water interfaces relevant to biological and environmental systems.* Chem. Rev., 2014. **114**(17): p. 8416-8446.
12. McFearin, C.L., et al., *From Franklin to today: toward a molecular level understanding of bonding and adsorption at the oil−water interface.* J. Phys. Chem. C, 2009. **113**(4): p. 1171-1188.
13. Gan, W., et al., *Polarization and experimental configuration analyses of sum frequency generation vibrational spectra, structure, and orientational motion of the air/water interface.* J. Chem. Phys., 2006. **124**(11): p. 114705.
14. Wang, H.-F., et al., *Quantitative spectral and orientational analysis in surface sum frequency generation vibrational spectroscopy (SFG-VS).* Int. Rev. Phys. Chem., 2005. **24**(2): p. 191-256.

15. Bonn, M., Y. Nagata, and E.H.G. Backus, *Molecular structure and dynamics of water at the water–air interface studied with surface-specific vibrational spectroscopy.* Angew. Chem. Int. Ed., 2015. **54**(19): p. 5560-5576.
16. Shen, Y.R. and V. Ostroverkhov, *Sum-frequency vibrational spectroscopy on water interfaces: polar orientation of water molecules at interfaces.* Chem. Rev., 2006. **106**(4): p. 1140-1154.
17. Davis, J.G., et al., *Water structural transformation at molecular hydrophobic interfaces.* Nature, 2012. **491**(7425): p. 582-585.
18. Day, J.P.R. and C.D. Bain, *Ellipsometric study of depletion at oil-water interfaces.* Phys. Rev. E, 2007. **76**(4): p. 041601.
19. Bigelow, W.C., D.L. Pickett, and W.A. Zisman, *Oleophobic monolayers.* J. Colloid Sci., 1946. **1**(6): p. 513-538.
20. Chen, Y., et al., *Three dimensional nano "Langmuir trough" for lipid studies.* Nano Lett., 2015. **15**(8): p. 5558-5563.
21. Basu, K., et al., *Determining the ice-binding planes of antifreeze proteins by fluorescence-based ice plane affinity.* J. Vis. Exp., 2014(83): p. e51185.
22. Groenzin, H., *Sum-frequency studies of single crystalline ice Ih*, 2007, Tufts University.
23. Strazdaite, S., et al., *Enhanced ordering of water at hydrophobic surfaces.* J. Chem. Phys., 2014. **140**(5): p. 054711.
24. Peltonen, L.J. and J. Yliruusi, *Surface pressure, hysteresis, interfacial tension, and CMC of four sorbitan monoesters at water–air, water–hexane, and hexane–air interfaces.* J. Colloid Interface Sci., 2000. **227**(1): p. 1-6.
25. Pool, R.E., et al., *Comparative Study of Direct and Phase-Specific Vibrational Sum-Frequency Generation Spectroscopy: Advantages and Limitations.* J Phys Chem B, 2011. **115**(51): p. 15362-15369.
26. Feng, R.-r., et al., *Consistency in the Sum Frequency Generation Intensity and Phase Vibrational Spectra of the Air/Neat Water Interface.* J. Phys. Chem. A, 2011. **115**(23): p. 6015-6027.
27. Warren, S.G. and R.E. Brandt, *Optical constants of ice from the ultraviolet to the microwave: A revised compilation.* J. Geophys. Res., 2008. **113**(D14): p. D14220.
28. Max, J.-J. and C. Chapados, *Isotope effects in liquid water by infrared spectroscopy. III. H2O and D2O spectra from 6000 to 0cm−1.* J. Chem. Phys., 2009. **131**(18): p. 184505.
29. Kedenburg, S., et al., *Linear refractive index and absorption measurements of nonlinear optical liquids in the visible and near-infrared spectral region.* Opt. Mater. Express, 2012. **2**(11): p. 1588-1611.

30. Zhuang, X., et al., *Mapping molecular orientation and conformation at interfaces by surface nonlinear optics.* Phys. Rev. B, 1999. **59**(19): p. 12632-12640.
31. Jackson, J.D., *Classical Electrodynamics* 1999, New York: Wiley.
32. de Beer, A.G.F. and S. Roke, *Nonlinear Mie theory for second-harmonic and sum-frequency scattering.* Physical Review B, 2009. **79**(15): p. 155420.
33. Bertie, J.E., M.K. Ahmed, and H.H. Eysel, *Infrared intensities of liquids. 5. Optical and dielectric constants, integrated intensities, and dipole moment derivatives of water and water-d2 at 22.degree.C.* J. Phys. Chem., 1989. **93**(6): p. 2210-2218.
34. Tuntomo, A., C.L. Tien, and S.H. Park, *Optical Constants of Liquid Hydrocarbon Fuels.* Combust. Sci. Technol., 1992. **84**(1-6): p. 133-140.
35. Zhang, W.-k., et al., *Reconsideration of second-harmonic generation from isotropic liquid interface: Broken Kleinman symmetry of neat air/water interface from dipolar contribution.* The Journal of Chemical Physics, 2005. **123**(22): p. 224713.
36. de Beer, A.G.F. and S. Roke, *Obtaining molecular orientation from second harmonic and sum frequency scattering experiments in water: Angular distribution and polarization dependence.* The Journal of Chemical Physics, 2010. **132**(23): p. 234702.
37. Abraham, M.H., et al., *Thermodynamics of solute transfer from water to hexadecane.* Journal of the Chemical Society, Perkin Transactions 2, 1990(2): p. 291-300.
38. Roke, S., et al., *Vibrational sum frequency scattering from a submicron suspension.* Phys. Rev. Lett., 2003. **91**(25): p. 258302.
39. Roke, S. and G. Gonella, *Nonlinear light scattering and spectroscopy of particles and droplets in liquids.* Annu. Rev. Phys. Chem., 2012. **63**(1): p. 353-378.
40. Hunt, J.H., P. Guyot-Sionnest, and Y.R. Shen, *Observation of C-H stretch vibrations of monolayers of molecules optical sum-frequency generation.* Chem. Phys. Lett., 1987. **133**(3): p. 189-192.
41. Harris, A.L., et al., *Monolayer vibrational spectroscopy by infrared-visible sum generation at metal and semiconductor surfaces.* Chem. Phys. Lett., 1987. **141**(4): p. 350-356.
42. Bohren, C.F. and D.R. Huffman, *Absorption and scattering of light by small particles* 2007: Wiley, New York. 530.
43. Du, Q., et al., *Vibrational spectroscopy of water at the vapor/water interface.* Phys. Rev. Lett., 1993. **70**(15): p. 2313-2316.
44. Auer, B.M. and J.L. Skinner, *Vibrational Sum-Frequency Spectroscopy of the Water Liquid/Vapor Interface†.* J. Phys. Chem. B, 2009. **113**(13): p. 4125-4130.
45. Ni, Y. and J.L. Skinner, *Communication: Vibrational sum-frequency spectrum of the air-water interface, revisited.* J. Chem. Phys., 2016. **145**(3): p. 031103.

46. Buch, V., et al., *Sum frequency generation surface spectra of ice, water, and acid solution investigated by an exciton model.* J. Chem. Phys., 2007. **127**(20): p. 204710.
47. Sovago, M., et al., *Vibrational Response of Hydrogen-Bonded Interfacial Water is Dominated by Intramolecular Coupling.* Phys. Rev. Lett., 2008. **100**(17): p. 173901.
48. Scatena, L.F., M.G. Brown, and G.L. Richmond, *Water at Hydrophobic Surfaces: Weak Hydrogen Bonding and Strong Orientation Effects.* Science, 2001. **292**(5518): p. 908-912.
49. Stiopkin, I.V., et al., *Hydrogen bonding at the water surface revealed by isotopic dilution spectroscopy.* Nature, 2011. **474**(7350): p. 192-195.
50. Shultz, M.J., et al., *Sum frequency generation spectroscopy of the aqueous interface: Ionic and soluble molecular solutions.* Int. Rev. Phys. Chem., 2000. **19**(1): p. 123-153.
51. Nihonyanagi, S., et al., *Accurate determination of complex χ(2) spectrum of the air/water interface.* J. Chem. Phys., 2015. **143**(12): p. 124707.
52. Zhang, Z., et al., *Ultrafast vibrational energy transfer at the water/air interface revealed by two-dimensional surface vibrational spectroscopy.* Nat Chem, 2011. **3**(11): p. 888-893.
53. Jena, K.C., R. Scheu, and S. Roke, *Surface impurities are not responsible for the charge on the oil/water interface: a comment.* Angew. Chem., Int. Ed., 2012. **51**(52): p. 12938-12940.
54. Etienne, G., M. Kessler, and E. Amstad, *Influence of fluorinated surfactant composition on the stability of emulsion drops.* Macromol. Chem. Phys., 2017. **218**: p. 1600365.
55. Stöckel, P., et al., *Rates of homogeneous ice nucleation in levitated H2O and D2O droplets.* J. Phys. Chem. A, 2005. **109**(11): p. 2540-2546.
56. Li Barnett, I., H. Groenzin, and M.J. Shultz, *Hydrogen bonding in the hexagonal ice surface.* J. Phys. Chem. A, 2011. **115**(23): p. 6039-6045.
57. Frank, H.S. and M.W. Evans, *Free volume and entropy in condensed systems iii. Entropy in binary liquid mixtures; partial molal entropy in dilute solutions; structure and thermodynamics in aqueous electrolytes.* J. Chem. Phys., 1945. **13**(11): p. 507-532.
58. Glew, D.N., *Aqueous solubility and the gas-hydrates. The methane-water system.* J. Phys. Chem., 1962. **66**(4): p. 605-609.
59. Jung, Y. and R.A. Marcus, *On the Theory of Organic Catalysis "on Water".* J. Am. Chem. Soc., 2007. **129**(17): p. 5492-5502.
60. Aryal, P., et al., *A hydrophobic barrier deep within the inner pore of the TWIK-1 K2P potassium channel.* Nat. Commun., 2014. **5**.
61. Chen, Y., K.C. Jena, and S. Roke, *From Hydrophobic to Hydrophilic: The Structure and Density of the Hexadecane Droplet/Alkanol/Water Interface.* The Journal of Physical Chemistry C, 2015. **119**(31): p. 17725-17734.

Chapter 5: Surface potential, ion pairing and surface water order on water droplets dispersed in non-polar solvent

Water micro- and nanodroplets are important components of many environmental, medical, catalytical, industrial and technological systems. Within these systems the water droplet interface greatly determines the physicochemical properties and reactivity. Interfacial droplet properties are traditionally inferred from results obtained from experiments performed on a solution or planar extended interfaces, even though confinement and curvature may result in completely different circumstances. Here, we use sum frequency scattering and second harmonic scattering to determine the water orientation and surface potential of charge stabilized water droplets in the hydrophobic solvent CCl_4. The method also allows us, uniquely, to extract the amount of free ions in the oil phase from the optical process. The interfacial water restructures upon addition of docusate sodium (AOT) amphiphiles, due to the enhanced interaction of the charged head groups with the water. Upon increasing the concentration of AOT molecules this favorable interaction constitutes a mechanism for interface-facilitated micellization.

5.1 Introduction

Water droplets are omnipresent in nature as clouds, aerosols [1], in oil fields and in geological materials [2, 3]. In biotechnological applications water droplets are used as nanoliter reaction vessels for the mixing [4-7] and delivery [8] of chemicals in life inspired or medical systems. The chemical properties and reactivity of water droplets are strongly determined by the surface structure of the water droplet and the role it plays in the delivery of chemicals to the interior or exterior, or the transformation in surface chemical reactions.

The molecular properties of water droplet interfaces are elusive and are thus inferred from studies on solutes, such as alcohols [9] or dissolved gases [10] or studies of extended planar oil/water interfaces [11, 12]. However, as we showed in the previous chapter, 100 nm water droplets dispersed in a hydrophobic liquid have a surface structure that corresponds to an equivalent planar interface that is 50 K colder. The water surface of such a droplet in contact with a hydrophobic liquid has substantially more ordering in the hydrogen bond network. In addition sum frequency scattering studies on charged surfactant stabilized oil droplets in water showed that surfactant coverage is at least a factor of ten lower than on equivalent planar interfaces [13, 14]. The nanoscale dimension of the aqueous droplet interface therefore has a significant influence on the chemical properties and surface chemical properties cannot be inferred from observation done on planar interfaces or in bulk solution.

To further chart the unknown interfacial nanoscale properties of water droplets we have performed sum frequency and second harmonic scattering measurements on ~100 nm water droplets in CCl_4 stabilized with the charged amphiphile molecule docusate sodium (AOT). AOT is present at the interface and distorts the hydrogen bond network of interfacial water, resulting in a larger population of more weakly hydrogen bonded water molecules, presumably through the hydrogen bond interaction with the charged SO_3^- head group. Polarimetric angle resolved SHS measurements are recorded for different concentrations of AOT (0.1-15 mM) and are modeled with an adapted nonlinear light scattering theory, from which the amount of orientational order at the water interface can be extracted, as well as the surface potential and the number of free charges in the oil phase, which is in the nanomolar range. The rest of the charges are ion-paired or self-assembled in micelles. Below the cmc, with increasing concentration, AOT molecules adsorb increasingly to the interface, reduce the surface potential and enhance the water ordering. Above the cmc the surface potential reduces and the orientational ordering of water inverts, which suggests that the surface water molecules play an active role in the conversion of AOT into micelles. Thus, we observe that the droplet interface acts as a nucleation site for micelles.

5.2 Materials and methods

5.2.1 Sample preparation and chemicals

Sample preparation was performed using constant size approach described previously [13]. First, a stock emulsion of 1% H_2O with 2 mM AOT was prepared using sonication in Badelin Sonorex Digiplus DL156BH ultrasonic bath for 10 min. Then the sample was diluted to 0.05% for SHS measurements adding appropriate amounts of CCl_4 and AOT. The size distribution was measured using a Malvern Zetasizer Nano. The z-average radius was 72.5 nm and the polydispersity index was 0.17. To get sufficient intensity in the SFS measurements we used 1% D_2O droplets stabilized with 4 mM AOT. AOT (98%) and CCl_4 (for HPLC >99.9%) were provided by Sigma-Aldrich. Since CCl_4 might be corrosive to normal pipette tips, all handling of the solutions of CCl_4 was performed using glass Pasteur pipettes or solventsafe pipette tips as well as glass vials with caps for chloroform solutions.

5.2.2 Partitioning experiment

Partitioning experiment was performed using a FTIR Bruker Vertex 70 spectrometer**.** 10 mM of AOT was dispersed in water and added to the equal amount of pure CCl_4 and equilibrated for 3 days in closed vials. The spectra are shown in Figure 5.1 indicating that AOT has slightly larger propensity to water phase.

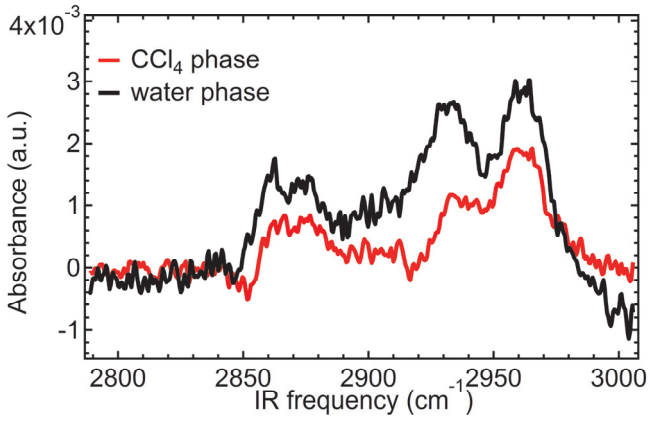

Figure 5.1. FTIR spectra of water phase (black) and CCl_4 phase (red) with AOT in the partitioning experiment.

5.2.3 Analysis of the SHS data

To determine the surface potential and the relative number of oriented water molecules as well as the amount of free ions in the oil phase we measured angle resolved SHS patterns of a range of AOT concentrations, from 0.1 mM up to 15 mM. The cmc for AOT in CCl_4 is 0.6 mM [15]. Polari-

metric angle resolved SHS has been used recently to determine the surface potential of oil droplets [16] and liposomes [17] in aqueous solutions. This method relies on the mixing of the interfacial electrostatic field (generated by the charges, and the polarization of the medium) with the optical fields into second harmonic photons. The angle resolved scattered SH field can be expressed as a function of the surface potential (Φ_0) and the effective surface susceptibility of the interface ($\chi_2^{(2)}$) and the ionic strength in the aqueous phase. In this implementation the water molecules rotate in response to the electrostatic field and are effectively used as a reporter of the surface potential via their non-zero second-order hyperpolarizability tensor $\beta^{(2)}$. Here, the situation is different as the main phase that is used as a reporter of the electrostatic field is CCl_4, a centrosymmetric molecule that cannot be reoriented by an electrostatic field and has no second order hyperpolarizability tensor. However, the third-order hyperpolarizability tensor of CCl_4 is non-zero, which effectively results in a second harmonic polarizability that can be used to read out the surface potential of the interface.

The algorithm that allows extracting a unique value of the surface potential without making any assumptions on the surface chemistry is described in detail in Refs. [18, 19]. First, we describe general consideration and then the corrections made to apply this formalism in the current study. The algorithm to obtain the surface potential is based on nonlinear light scattering theory using the Rayleigh-Gans-Debye-(RGD) approximation with a first-order correction for the jump in the electromagnetic field amplitude across the interface [20, 21]. The scattered polarized light is a function of the geometry of the illuminating electromagnetic fields and their respective polarization state, the shape and size of the particles, and the effective nonlinear particle susceptibility, a material property. Within the RGD approximation, an analytical solution [22] is obtained for normalized SHS intensity $S_{PPP}(\theta)$ from a sphere (or shell):

$$\frac{I_{PPP}(\theta)}{I_{SSS}(\theta)} = \frac{\left(E_1(\omega)^2\left[\cos\left(\frac{\theta}{2}\right)^3\Gamma_1^{(2)}+\cos\left(\frac{\theta}{2}\right)\left(\Gamma_2^{(2)}+\Gamma_2^{(3)\prime}\right)(2\cos(\theta)+1)\right]\right)^2}{\overline{\mu}^2 N_b/N_p} = S_{PPP}(\theta) \tag{5.1}$$

in which $\Gamma_i^{(2)}$ and $\Gamma_2^{(3)\prime}$ are the only non-zero elements of the nonlinear effective particle susceptibilities (defined in Ref.[23]), $\overline{\mu}$ is the averaged induced dipole moment; $N_p$is the number droplets, and N_b is the density of bulk water (3.34 $\cdot 10^{28}$ molecules/m^3). The elements of the nonlinear effective particle susceptibility are linked to the surface susceptibility according to the expressions in Table 5.1. N_b/N_p is the number of bulk water molecules per droplet. Water, with a known [24] nonlinear optical response, is used here as a reference.

Equation (5.1) is derived assuming that the liquid interface is spatially isotropic in the azimuthal direction, the optical process is lossless, and that water possesses a broad orientational distribution. These assumptions were validated in previous studies [18, 19, 25]. Although we employ the

Susceptibility elements for water	Susceptibility elements for CCl_4
$\Gamma_1^{(2)} = \left(2F_1(qR) - 5F_2(qR)\right)\chi_{s,1}^{(2)''}$ $\Gamma_2^{(2)} = F_2(qR)\chi_{s,1}^{(2)''} + 2F_1(qR)\chi_{s,2}^{(2)''}$ $\Gamma_2^{(3)'} = 0$ $\chi_{s,1}^{(2)''} = 27\eta\frac{\left(\chi_{s,1}^{(2)}\eta^2 + 3\chi_{s,2}^{(2)}(\eta^2-1)\right)}{(2+\eta)^3}$ $\chi_{s,2}^{(2)''} = 27\,\eta\,\frac{\chi_{s,2}^{(2)}}{(2+\eta)^3}$	$\Gamma_1^{(2)} = 0$ $\Gamma_2^{(2)} = 0$ $\Gamma_2^{(3)'} = 2\,\chi_2^{(3)''}\Phi_0\left(F_1(qR) + F_3(qR,\kappa R)\right)$ $\chi_2^{(3)''} = 27\,\eta\,\frac{\chi_2^{(3)'}}{(2+\eta)^3}$ $\chi_2^{(3)'} = \frac{N_b}{\epsilon_0}\bar{\beta}^{(3)}$
Constants and equalities	
μ_{dc}=8.97 × 10^{-30} Cm $\bar{\beta}^{(2)}$=3.09 × 10^{-52} $C^3m^3J^{-2}$	μ_{dc}=0; $\bar{\beta}^{(2)}$=0 $\bar{\beta}^{(3)}$ =122 × 10^{-65} $C^4m^4J^{-3}$
$\chi_{s,1}^{(2)} = \chi_{s,\perp\perp\perp}^{(2)} - \chi_{s,\parallel\parallel\perp}^{(2)} - \chi_{s,\parallel\perp\parallel}^{(2)} - \chi_{s,\perp\parallel\parallel}^{(2)}$ $\chi_{s,2}^{(2)} = \chi_{s,\parallel\parallel\perp}^{(2)}$ (⊥: surface normal direction; || tangential direction) $\chi_{s,1}^{(2)} \to 0$ $\chi_{s,4}^{(2)} = \chi_{s,3}^{(2)} = \chi_{s,2}^{(2)}$; $\chi_4^{(3)'} = \chi_3^{(3)'} = \chi_2^{(3)'}$ $\eta = \left(\frac{n_{H2O}}{n_{CCl4}}\right)^2$	
Form factor functions and scattering vector [18, 21]	
$F_1(qR) = 2\pi R^2 i\left(\frac{\sin(qR)}{(qR)^2} - \frac{\cos(qR)}{qR}\right)$ $F_2(qR) = 4\pi R^2 i\left(3\frac{\sin(qR)}{(qR)^4} - 3\frac{\cos(qR)}{(qR)^3} - \frac{\sin(qR)}{(qR)^2}\right)$ $F_3(\kappa R, qR) = 2\pi R^2 i\frac{qR\cos(qR) + \kappa R\sin(qR)}{(qR)^2 + (\kappa R)^2}$ $\boldsymbol{q} \equiv \boldsymbol{k}_0 - 2\boldsymbol{k}_1$; $q = \left\lvert\frac{4\pi n}{\lambda_{SH}}\sin\frac{\theta}{2}\right\rvert$	

Table 5.1. Susceptibility elements, constants, and equalities as used in Eq. 5.2 to describe the water normalized scattering patterns.

RGD assumption for the linear interaction, the nonlinear interaction contains a correction to account for the change in field amplitude when the optical electromagnetic fields cross the particle/water interface. Dadap *et al.* showed that a linear correction term to the second-order suscepti-

bility is sufficient to correct for the change in the electromagnetic field when it crosses the interface [26]. This correction for the susceptibility value is used here and listed in Table 5.1.

For the water droplets dispersed in CCl_4 these general equations were adopted as follows:

$$\frac{I_{PPP}(\theta)}{I_{SSS}(\theta)} = \frac{\left(E_1(\omega)^2\left[\cos\left(\frac{\theta}{2}\right)^3(\Gamma^{(2)}_{1,H2O}-\Gamma^{(2)}_{1,CCl4})+\cos\left(\frac{\theta}{2}\right)\left(\Gamma^{(2)}_{2,H2O}-\Gamma^{(2)}_{2,CCl4}+\Gamma^{(3)\prime}_{2,H2O}+\Gamma^{(3)\prime}_{2,CCl4}\right)(2\cos(\theta)+1)\right]\right)^2}{\overline{\mu}^2 N_b/N_p} \tag{5.2}$$

where $\Gamma^{(2)}_{1,H2O}$, $\Gamma^{(2)}_{2,H2O}$ and $\Gamma^{(3)\prime}_{2,H2O}$ correspond to the inner part of the droplet, and $\Gamma^{(2)}_{1,CCl4}$, $\Gamma^{(2)}_{2,CCl4}$ and $\Gamma^{(3)\prime}_{2,CCl4}$ correspond to the outer part of the droplet.

CCl_4, because of its tetrahedral symmetry, has a vanishing dipole moment as well as zero value of average $\bar{\beta}^{(2)}$ (therefore, there is no induced dipole moment either). Thus the second-order susceptibility elements $\Gamma^{(2)}_{1,CCl4}$ and $\Gamma^{(2)}_{2,CCl4}$ are zero. Futhermore, we assume that the inner part of the water droplet does not contribute to the SHS signal with $\Gamma^{(3)\prime}_{2,H2O}$ because of the absence of water ordering inside the droplet due to electrostatic considerations: The electric field inside the droplet should vanish [27]. The assumption that $\Gamma^{(3)\prime}_{2,H2O}$ is zero means that surface potential inside the droplet is constant. In addition contributions from inside would be much smaller than those of the outside as the intensity scales with R^6. Thus we obtain the simplified version of the Eq. (5.2):

$$\frac{I_{PPP}(\theta)}{I_{SSS}(\theta)} = \frac{\left(E_1(\omega)^2\left[\cos\left(\frac{\theta}{2}\right)^3\Gamma^{(2)}_{1,H2O}+\cos\left(\frac{\theta}{2}\right)\left(\Gamma^{(2)}_{2,H2O}+\Gamma^{(3)\prime}_{2,CCl4}\right)(2\cos(\theta)+1)\right]\right)^2}{\overline{\mu}^2 N_b/N_p}.$$

Here, $\Gamma^{(2)}_{1,H2O}$ and $\Gamma^{(2)}_{2,H2O}$ depend on the non-zero second-order surface susceptibility element $\chi^{(2)}_2$ which is a fitting parameter. $\chi^{(2)}_2$ is related to microscopic properties with eq. (2.6). $\Gamma^{(3)\prime}_{2,CCl4}$ depend on the concentration of ions in the outer phase c_{ions} and surface potential Φ. The examples of calculated SHS scattering patterns to show the influence of different parameters are shown in Figure 5.3. The results of the fitting for all samples are shown in Figure 5.4. Other required parameters, constants, and equalities are listed for completeness in Table 5.1.

5.3 Results and discussion

Figure 5.2 shows SFS spectra of AOT stabilized water droplets in CCl_4 (red trace), water droplets in a hydrophobic liquid (blue trace), composed of hexadecane and 5 mM Span80 [28], and the air/water SFG reflection mode spectrum (black trace [11]). The spectra were normalized taking into account linear absorption effects as well as discontinuities in the normal component of the electromagnetic fields as they cross the droplet interface (as in [28]). The modes in the frequency range

2800-3000 cm^{-1} report on the CH stretch modes of the Span80 or AOT, which confirms that these molecules are present at the interface. All three OD spectra have two broad features: A peak at 2370 cm^{-1}, and a peak at 2500 cm^{-1}. The frequency of the OD stretching vibrations is correlated to the strength of the interfacial hydrogen bond interaction since the OD frequency decreases with increasing hydrogen bond strength. The feature at 2500 cm^{-1} therefore reports on water molecules that are more weakly hydrogen bonded than the ones that attribute to the 2370 cm^{-1} feature. Comparing the charged AOT/CCl_4 water droplet interface to the hexadecane/Span80 droplet interface, it can be seen that there are relatively more weakly hydrogen bonded water molecules at the AOT/CCl_4 water droplet interface. The spectrum of AOT stabilized water droplets has relatively more intensity in the frequency range 2600-2800 cm^{-1}, which indicates that there is a larger population of very weakly hydrogen bonded water molecules. Given the similarity to Raman solvation shell spectra of SOS in water [29], these weakly hydrogen bonded water molecules are likely interacting with the charged sulfonate head group of AOT. The peak at 2745 cm^{-1} originates from interfacial OD bonds that are not hydrogen bonded and is only present at the air/water interface. The SFS spectrum for the CCl_4 water droplet interface is very different from the one measured from the macroscopic CCl_4/water interface, which displays dominating weakly H-bonded peak [12]. The concepts of weakly and strongly H-bonded water were introduced in Chapter 1.

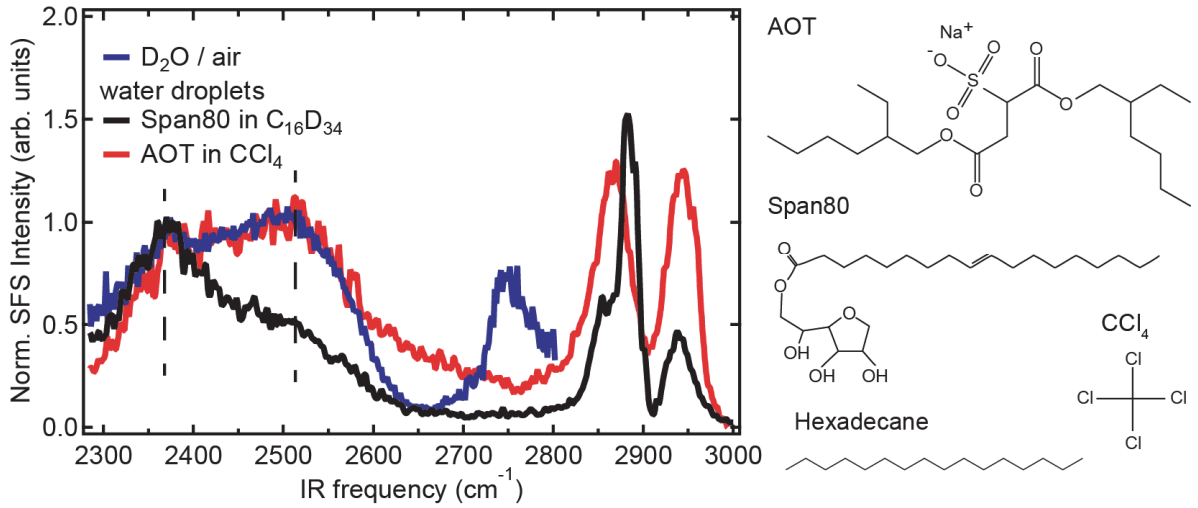

Figure 5.2. SFG spectrum of water/air interface [11] (blue) and SFS spectra of water droplets in CCl_4 stabilized with 4.2 mM AOT (red) and in deuterated hexadecane stabilized with 5mM Span80 (black). All spectra were measured in SSP polarization combination. Structures of AOT, CCl_4, Span80, and hexadecane are shown on the right.

Next, we describe SH scattering patterns that report on the surface potential, the surface susceptibility of water and the ionic strength in the hydrophobic phase in three different ways. The details of the implementation are shown above. Figure 5.3A-C show three computations of SHS patterns in the PPP polarization combination, using Φ_0, $\chi_2^{(2)}$ and c_{ion} as input parameters, where Φ_0 is varied from -20 to -40 mV (A), $\chi^{(2)}{}_2$ is varied from 5.65 10^{-23} m^2/V to 2.26 10^{-22} m^2/V (B), and c_{ion}

is varied from 1 nM to 100 nM (C). This shows that an increase in surface potential results in more intense scattering patterns, while an increase in the amount of orientational ordering of the interfacial water inside the droplet results in more intense side lobes, and an increase in the amount of free charge carriers results in broader forward peaks. Thus, these three distinct features can be used to quantify the surface potential, the amount of ordered interfacial water molecules and the number of free charge carriers in the oil phase.

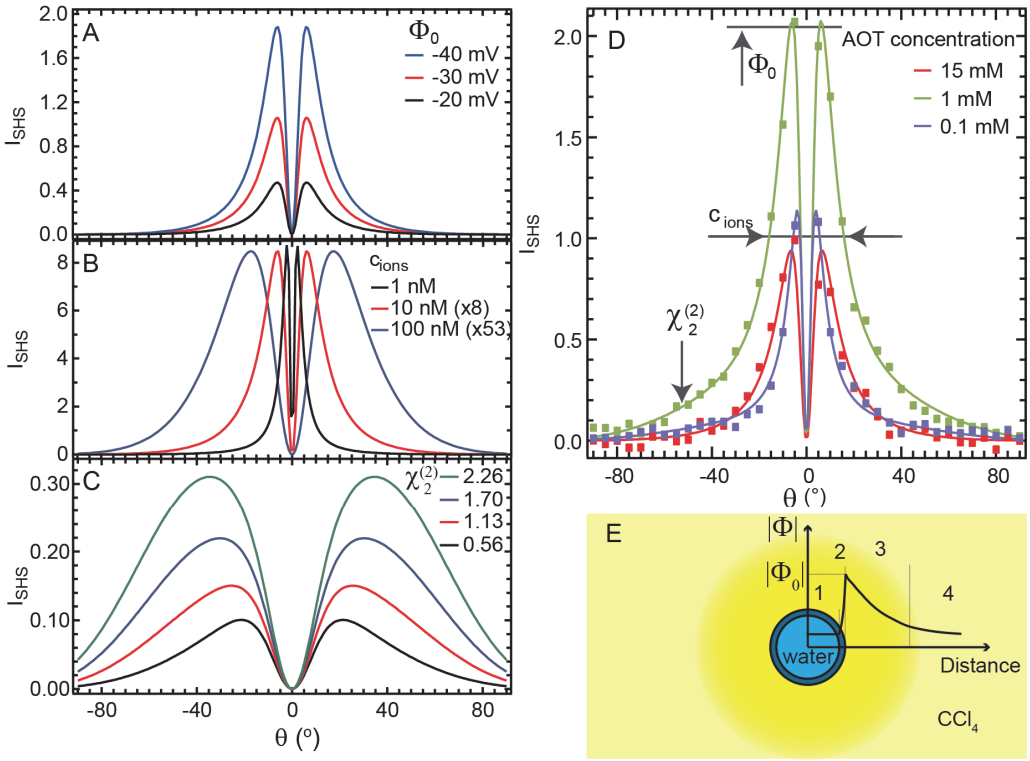

Figure 5.3. Left panels: Calculated SHS patterns for particles with the same size and number density in solution with different computational parameters: A: SHS patterns calculated only for the diffuse layer of CCl_4 with 10 nM concentration of free charges and different values of surface potential. B: SHS patterns calculated for the diffuse layer of CCl_4 with fixed value of surface potential (-30 mV) and different concentration of free charges. C: SHS patterns calculated for water with a zero value of the surface potential and different values of $\chi_2^{(2)}$ (in 10^{-22} m^2/V). Right panels: D. SHS scattering patterns measured in the PPP polarization combination of water droplets of the same size (with the radius of 72 nm) dispersed in CCl_4 and stabilized with different concentrations of AOT (15 mM, red, 1 mM, green and 0.1 mM, blue). The markers show the experimental data and the lines are fits. Details of the fitting are described in the text. E. Water droplet in CCl_4 with the sketch of electrostatics in the surrounding of the interfacial region: (1) The inner part of the water droplet, which does not contribute to the SHS response. (2) Dark-blue shows surface layer together with the Stern layer in the water phase. The SHS from this region is shown in panel C (3) The extended diffuse layer in the hydrophobic phase, which give rise to SHS shown in panels B and C (4) Unperturbed CCl_4 far from the droplet, which does not contribute to the SHS response.

Figure 5.3 D shows three representative SHS patterns in the PPP polarization combination recorded from water droplets prepared with AOT at three different concentrations, below the cmc

(0.1 mM), approximately at the cmc [15] (1 mM), and above the cmc (15 mM) of AOT in CCl_4. Note that AOT partitions roughly equally in the aqueous phase of the drops but since we use 0.05 vol.% of drops this does not significantly alter the concentration in CCl_4. It can be seen that the scattering patterns are different in magnitude (Φ_0), in the width of the forward peaks (concentration of ions in the oil phase) and in the presence of scattered light at larger angles ($\chi_2^{(2)}$). Additional SHS data measured in PSS polarization combination is shown in Figure 5.5. We note that fitting of these data does not provide additional information because of small intensity and relatively poor signal-to-noise ratio.

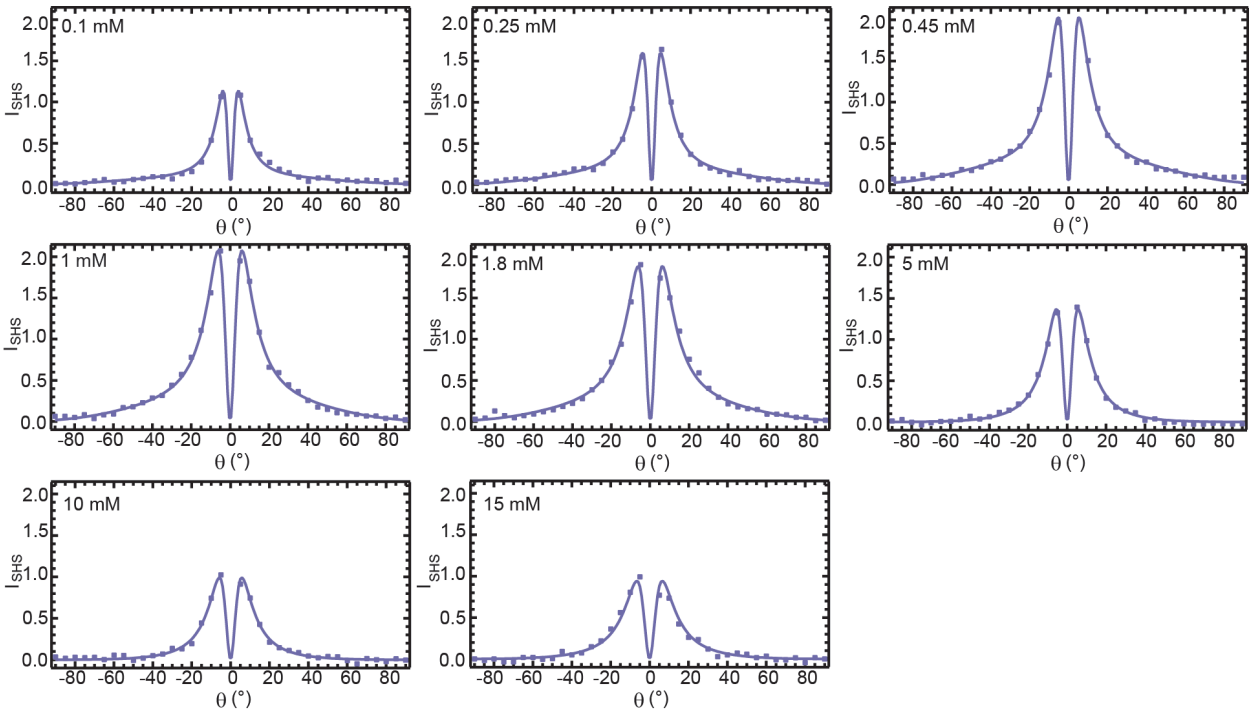

Figure 5.4. Experimental (markers) and fitted (lines) SHS patterns in PPP polarization combination for samples with the concentration of AOT in CCl_4 from 0.1 mM to 15 mM.

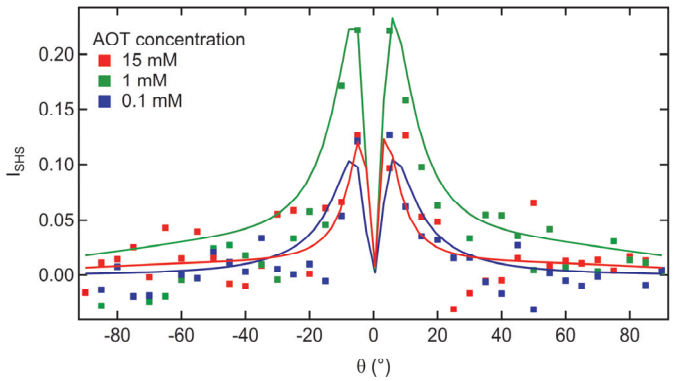

Figure 5.5. Second harmonic scattering patterns measured in PSS polarization combination for water droplets in CCl_4 stabilized with different concentrations of AOT: 15 mM (red), 1 mM (green) and 0.1 mM (blue). Solid lines are fit curves with the values described in the text.

Analyzing a series of scattering patterns (see Figure 5.5) we derive values for Φ_0, $\chi_2^{(2)}$ and c_{ion}. The values are plotted in Figure 5.6. As AOT is increased in concentration, up to the cmc, we observe an increase in $|\Phi_0|$, an increase in $\chi_2^{(2)}$ and an increase in c_{ion}. This reflects the increase in interfacial number density of AOT, which orients more water molecules as it adds more negative charge to the interface.

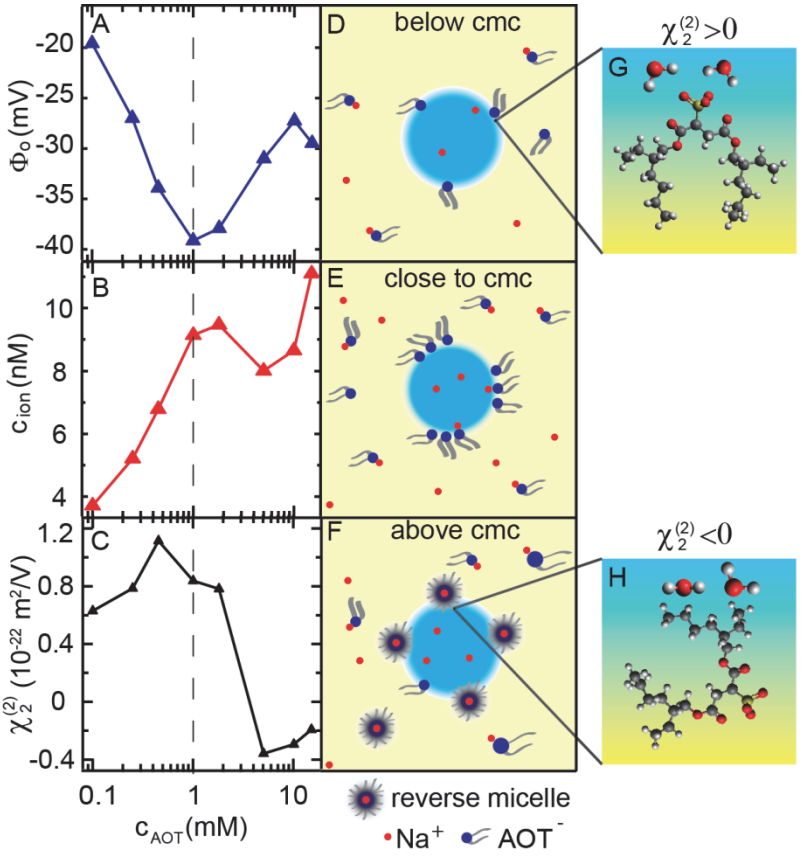

Figure 5.6. Fitted values of surface potential Φ_0 (A), concentration of free ions c_{ions} (B) and water ordering $\chi_2^{(2)}$ (C). Panels D-F show the proposed mechanism of changes at the interface of the water droplet (blue) in CCl_4 (yellow) with an increase of the surfactant concentration. D. At low surfactant concentration the interface is stabilized with single AOT anions which produce a negative surface potential. Only a small portion of surfactant molecules is dissociated. E: The amount of these anions at the surface is increasing with increasing of the concentration of AOT, resulting in a larger charge at the interface and a larger amount of ions in the solution. Water ordering is gradually increasing as well. F: Above the cmc, the droplet is starting to be stabilized not only by single anions but also by reverse micelles that are seen to form at the interface. The surface potential increases and water ordering is decreasing, while the amount of charge carriers in solution levels off. Inlets G and H show possible molecular orientation of the interfacial water molecules below the cmc ($\chi_2^{(2)}>0$) and above the cmc ($\chi_2^{(2)}<0$), respectively. Molecules are not to scale for clarity.

The concentration of dissociated ions in the oil phase meanwhile increases from 4 to 9 nM. Note that this is to our knowledge the first non-invasive quantification of ion pairing in solution and of the ~ 1 mM AOT molecules, just 1 in 10^5 AOT molecules is ionized. Above the cmc $|\Phi_0|$ decreases,

$\chi_2^{(2)}$ decreases and inverts sign and c_{ion} levels off and increases further. The latter can be explained by the appearance of inverted micelles in the CCl_4 phase, which also carry a charge. On the interface the drop in $|\Phi_0|$ suggests that a smaller number of free AOT ions are absorbed. The inverse of the sign in $\chi_2^{(2)}$ means that water molecules have changed their orientation. This can happen when AOT molecules move out of the water phase and into the oil side as a partially self-assembled structure closes up around a few water molecules that form the core of the micelle. The micelle then moves into the bulk CCl_4 phase. The average orientation of the interfacial water is first determined by the S-O - H-O interaction, and above the cmc by the interaction of micelle alkyl chains with water. This results in an initial average orientation of water hydrogens towards the interface, and at higher concentration average orientation that favors a more parallel orientation with water oxygens pointing towards the interface, as it was shown in [30]. Such interactions also explain the drop in Φ_0, and clearly suggest that the water droplet interface acts as a reaction site for the self-assembly of micelles.

5.4 Conclusions

Thus, we have measured the molecular structure, the electrostatic potential, and orientation of water at the interface of water droplets in the hydrophobic solvent, in contact with charged surfactants. We observe that the nanoscale water droplet interfaces behave as a reaction intermediate, at low concentrations by collecting AOT molecules at the interface that modify the water surface structure such that its hydrogen bond network weakens. The weakly hydrogen bonded water molecules are then used as cores for the micelles that form at the droplet interface. Upon their formation the average orientation of water molecules at the interface changes from on average hydrogen up to on average weakly hydrogen down or parallel to the interface. During the whole process the surface potential first rises, reflecting an increase in surface AOT, and then drops, reflecting the formation of micelles.

The present experiments demonstrate the possibility of determining the interfacial water orientation and surface potential from water droplets, as well as the amount of free ions in the non-conducting oil phase adjacent to the interface, by combining sum frequency and polarimetric angle resolved second harmonic scattering. The observed role of the water droplet surface as a reaction intermediate for self-assembly highlights the importance of these interfaces and it can be expected that many more types of examples can be found. Since water droplets play important roles in our environment, industry and technology characterizing them will lead to both an increase in our understanding of diverse processes, such as cloud formation, the working of micro- and nanofluidics and self-assembly, as well fundamental knowledge on diverse length scale processes in nature.

5.5 References

1. de Leeuw, G., et al., *Production flux of sea spray aerosol.* Rev. Geophys., 2011. **49**(2): p. 1-39.
2. Zachara, J., et al., *Internal domains of natural porous media revealed: critical locations for transport, storage, and chemical reaction.* Environ. Sci. Technol., 2016. **50**(6): p. 2811-2829.
3. Putnis, A., *Why mineral interfaces matter.* Science, 2014. **343**(6178): p. 1441-1442.
4. Duncanson, W.J., et al., *Microfluidic synthesis of advanced microparticles for encapsulation and controlled release.* Lab on a Chip, 2012. **12**(12): p. 2135-2145.
5. Theberge, A.B., et al., *Microdroplets in Microfluidics: An Evolving Platform for Discoveries in Chemistry and Biology.* Angewandte Chemie International Edition, 2010. **49**(34): p. 5846-5868.
6. Miller, O.J., et al., *High-resolution dose–response screening using droplet-based microfluidics.* Proceedings of the National Academy of Sciences, 2012. **109**(2): p. 378-383.
7. Tawfik, D.S. and A.D. Griffiths, *Man-made cell-like compartments for molecular evolution.* Nat Biotech, 1998. **16**(7): p. 652-656.
8. Gerhardt, N.I. and S.R. Dungan, *Time-dependent solubilization of IgG in AOT-brine-isooctane microemulsions: Role of cluster formation.* Biotechnology and Bioengineering, 2002. **78**(1): p. 60-72.
9. Davis, J.G., et al., *Water structural transformation at molecular hydrophobic interfaces.* Nature, 2012. **491**(7425): p. 582-585.
10. Grdadolnik, J., F. Merzel, and F. Avbelj, *Origin of hydrophobicity and enhanced water hydrogen bond strength near purely hydrophobic solutes.* Proc. Natl. Acad. Sci., 2017. **114**(2): p. 322-327.
11. Strazdaite, S., et al., *Enhanced ordering of water at hydrophobic surfaces.* J. Chem. Phys., 2014. **140**(5): p. 054711.
12. Scatena, L.F., M.G. Brown, and G.L. Richmond, *Water at Hydrophobic Surfaces: Weak Hydrogen Bonding and Strong Orientation Effects.* Science, 2001. **292**(5518): p. 908-912.
13. Aguiar, H.B.d., et al., *The Interfacial Tension of Nanoscopic Oil Droplets in Water Is Hardly Affected by SDS Surfactant.* J. Am. Chem. Soc., 2010. **132**(7): p. 2122-2123.
14. Scheu, R., et al., *Specific Ion Effects in Amphiphile Hydration and Interface Stabilization.* J. Am. Chem. Soc., 2014. **136**(5): p. 2040-2047.

15. Tran, C.D. and S. Yu, *Near-infrared spectroscopic method for the sensitive and direct determination of aggregations of surfactants in various media.* J. Colloid Interface Sci., 2005. **283**(2): p. 613-618.
16. Lütgebaucks, C., G. Gonella, and S. Roke, *Optical label-free and model-free probe of the surface potential of nanoscale and microscopic objects in aqueous solution.* Physical Review B, 2016. **94**(19): p. 195410.
17. Lütgebaucks, C., C. Macias-Romero, and S. Roke, *Characterization of the interface of binary mixed DOPC:DOPS liposomes in water: The impact of charge condensation.* J. Chem. Phys., 2017. **146**(4): p. 044701.
18. Gonella, G., et al., *Second Harmonic and Sum Frequency Generation from Aqueous Interfaces is Modulated by Interference.* J. Phys. Chem. C, 2016. **120**: p. 9165-9173.
19. Lütgebaucks, C., G. Gonella, and S. Roke, *Optical label-free and model-free probe of the surface potential of nanoscale and microscopic objects in aqueous solution.* Phys. Rev. B, 2016. **94**(19): p. 195410- 195410.
20. Dadap, J.I., et al., *Second-Harmonic Rayleigh Scattering from a Sphere of Centrosymmetric Material.* Phys. Rev. Lett., 1999. **83**(20): p. 4045-4048.
21. de Beer, A.G.F. and S. Roke, *Obtaining molecular orientation from second harmonic and sum frequency scattering experiments in water: Angular distribution and polarization dependence.* J. Chem. Phys., 2010. **132**(23): p. 234702.
22. Gonella, G., et al., *Second Harmonic and Sum-Frequency Generation from Aqueous Interfaces Is Modulated by Interference.* The Journal of Physical Chemistry C, 2016. **120**(17): p. 9165-9173.
23. Roke, S., M. Bonn, and A.V. Petukhov, *Nonlinear optical scattering: The concept of effective susceptibility.* Phys Rev B, 2004. **70**(11).
24. Gubskaya, A.V. and P.G. Kusalik, *The multipole polarizabilities and hyperpolarizabilities of the water molecule in liquid state: an ab initio study.* Mol Phys, 2001. **99**(13): p. 1107-1120.
25. de Beer, A.G.F., R.K. Campen, and S. Roke, *Separating surface structure and surface charge with second-harmonic and sum-frequency scattering.* Phys. Rev. B, 2010. **82**(23): p. 235431.
26. Dadap, J.I., J. Shan, and T.F. Heinz, *Theory of optical second-harmonic generation from a sphere of centrosymmetric material: small-particle limit.* J. Opt. Soc. Am. B, 2004. **21**(7): p. 1328-1328.
27. Jackson, J.D., *Classical Electrodynamics* 1999, New York: Wiley.
28. Smolentsev, N., et al., *The interfacial structure of water droplets in a hydrophobic liquid.* 2017. **8**: p. 15548.

29. Scheu, R., et al., *Charge Asymmetry at Aqueous Hydrophobic Interfaces and Hydration Shells.* Angew. Chem., Int. Ed., 2014. **53**(36): p. 9560-9563.

30. Samson, J.-S., et al., *Sum frequency spectroscopy of the hydrophobic nanodroplet/water interface: Absence of hydroxyl ion and dangling OH bond signatures.* Chem. Phys. Lett., 2014. **615**: p. 124-131.

Chapter 6: Intermolecular headgroup interaction and hydration as driving forces for lipid trans-membrane asymmetry

Variations between the inner and outer leaflets of cell membranes are crucial for cell functioning and signaling, drug-membrane interactions, and the formation of lipid domains. Transmembrane asymmetry can in principle be comprised of an asymmetric charge distribution, differences in hydration, specific headgroup/H-bonding interactions or a difference in the number of lipids per leaflet. Here, we characterize the transmembrane asymmetry of small unilamellar liposomes consisting of zwitterionic and charged lipids in aqueous solution using vibrational sum frequency scattering and second harmonic scattering, label-free methods, specifically sensitive to lipid and water asymmetries. For single component liposomes, transmembrane asymmetry is present for the charge distribution and lipid hydration, but the leaflets are not detectably asymmetric in terms of the number of lipids per leaflet, even though geometrical packing arguments would predict so. Such a lipid transmembrane asymmetry can, however, be induced in binary lipid mixtures under conditions that enable H-bonding interactions between phosphate and amine groups. In this case, the measured asymmetry consists of a different number of lipids in the outer and inner leaflet, a difference in transmembrane headgroup hydration, and a different headgroup orientation for the interacting phosphate groups.

This chapter is based on the paper by Nikolay Smolentsev, Cornelis Lütgebaucks, Halil I. Okur, Alex G. F. de Beer and Sylvie Roke "Intermolecular headgroup interaction and hydration as driving forces for lipid transmembrane asymmetry" published in Journal of the American Chemical Society, 2016, 138 (12), pp 4053–4060 with equal contributions of Nikolay Smolentsev and Cornelis Lütgebaucks. Nikolay Smolentsev performed all SFS measurements, analysis and calculation of the orientation of the chemical groups, whereas Cornelis Lütgebaucks prepared all the samples, measured and evaluated the SH data.

6.1 Introduction

Compositional diversity between the inner and outer leaflets of cellular and organelle membranes are crucial for cell functioning. Non-random and non-equal leaflet composition occurs in eukaryotic membranes [1-3]. Certain lipids, such as glycolipids, phosphatidylcholine (PC) and sphingomyelin, are predominantly present in the outer leaflet, whereas others, such as phosphatidylserine (PS), are almost completely localized in the inner leaflet of the plasma membrane [4]. Although the molecular level details are still ambiguous, it is clear that transmembrane asymmetry [5], is vital for a cell. PS transmembrane asymmetry was, for example, shown to regulate and maintain cell metabolism [6, 7]. Transmembrane asymmetry can occur by means of active and passive pathways [2, 4]. Active pathways use regulating proteins and peptides to induce asymmetry [3, 8, 9], whereas passive pathways comprise several effects: a non-homogeneous inter-leaflet charge distribution or hydration, asymmetry of specific interactions, and packing differences between leaflets. Although all these effects have been studied, most attention has been given to transmembrane asymmetry as caused by a different available area in the inner and outer leaflet, which results in a different number of lipids in the inner and outer leaflet, and is related to local membrane stiffness and curvature [10].

The investigation of passive asymmetry [11-22] is in general challenging as it ideally requires free floating, unperturbed, membranes. In addition, labeling, substrates, or invasive tools, which can induce changes in the bilayer composition should ideally be avoided [23]. Sensitivity to molecular structure and the ability to distinguish between the inner and outer leaflet of a bilayer are further requirements. Vibrational sum frequency generation (SFG) [24-27] is a nonlinear spectroscopy that can be considered as a simultaneous IR and Raman measurement. SFG is forbidden in a centrosymmetric medium (under the dipole approximation [28]). It can therefore directly detect transmembrane asymmetry. Assuming identical orientational distributions with respect to the surface plane for lipids located on the inner and outer leaflets, SFG reports on the average number difference of lipids between the leaflets. These features were elegantly demonstrated by Conboy and co-workers who measured lipid redistribution across a supported planar bilayer that was initially made asymmetric [12-14].

Here we investigate hydration, charge and lipid transmembrane asymmetry in free floating lipid membranes. Lipid asymmetry and hydration in small unilamellar liposomes in solution (diameter < 100 nm) are probed using nonlinear light scattering. By measuring vibrational sum frequency scattering (SFS) spectra in the C-H and P-O stretch region of the vibrational spectrum, we quantify the transmembrane asymmetry of the fatty acid tails and headgroups of the lipids. Vibrational SFS [29-31] is a combination of SFG and light scattering that allows for the probing of chemically specific molecular asymmetry along the interfacial normal in liposome membranes. Transmembrane hy-

dration asymmetry is measured with non-resonant angle resolved [32] second harmonic scattering (SHS) [31, 33, 34], which probes transmembrane asymmetry in the orientational distribution of water molecules along the interfacial normal. The SHS signal relates to the surface potential [35-39] and to H-bond interactions involving water [40]. A change in the SHS intensity from liposomes is thus related to the difference in charge distribution between the leaflets. We find that charge and hydration asymmetry is present for liposomes made of 1,2-dioleoyl-*sn*-glycero-3-phosphocholine (DOPC), 1,2- dipalmitoyl-*sn*-glycero-3-phosphocholine (DPPC), 1,2- dipalmitoyl-*sn*-glycero-3-phosphoserine (DPPS), 1,2-dioleoyl-*sn*-glycero-3-phospho-L-serine (sodium salt) (DOPS), and mixtures of either DOPC with DPPS or 1,2- dipalmitoyl-*sn*-glycero-3-phosphate (DPPA). Figure 6.1 displays a sketch of the chemical structure of each lipid. For the same single component liposomes, lipid transmembrane asymmetry is not detected, even though calculations using a constant area per lipid indicate a detectable difference in lipid number between the inner and outer leaflet. Binary mixtures may display transmembrane asymmetry, which can be detected in the phosphate stretch region as a shifted vibrational resonance. This PO_2^- group has a tilt angle with respect to the surface that is more upright, compared to the same groups in a lipid monolayer. A signature of the acyl chains is also observed, but only for one of the lipids. These observations only occur if phosphoserine is present in the binary bilayer mixture, and the acyl chains of the lipids are different in length. Based on these observations and the structure of the lipids, we postulate that lipid transmembrane asymmetry is likely induced by H-bonding interactions between amine and phosphate groups that depend on packing differences as induced by differences in the fatty acid chain structure. Using this interpretation, we quantify the amount of asymmetry in the liposomes composed of a DOPC:DPPS mixture.

6.2 Materials and methods

6.2.1 Chemicals

Prior to use all glassware was cleaned with a 1:3 H_2O_2:H_2SO_4-solution, after which it was thoroughly rinsed with ultra-pure water (H_2O, Milli-Q UF plus, Millipore, Inc., electrical resistance of 18.2 MΩ cm). d_{34}-hexadecane ($C_{16}D_{34}$, 98% d, Cambridge Isotope), sulfuric acid (95-97%, ISO, Merck), H_2O_2 (30%, Reactolab SA) and chloroform (Emsure, ACS, ISO, Merck) was used as received. Lipids 1,2-dioleoyl-*sn*-glycero-3-phosphocholine (DOPC), 1,2-dipalmitoyl-*sn*-glycero-3-phosphocholine (DPPC), 1,2-dioleoyl-*sn*-glycero-3-phospho-L-serine (sodium salt) (DOPS), 1,2-dipalmitoyl-sn-glycero-3-phospho-L-serine (sodium salt) (DPPS), 1,2-dipalmitoyl-*sn*-glycero-3-phosphate (sodium salt) (DPPA), 1,2-dipalmitoyl-sn-glycero-3-phosphoethanolamine (DPPE), d_{62}-1,2-dipalmitoyl-sn-glycero-3-phospho-L-serine (sodium salt) (d_{62}-DPPS), and d_{66}-1,2-dioleoyl-*sn*-glycero-3-phosphocholine (d_{66}-DOPC), were purchased in powder form (>99%) from Avanti Polar

Lipids (Alabama, USA) and stored at -20 °C until further use. All samples for SFS measurements were prepared using D_2O (99.8% Armar, >2 MΩ cm). The chemical structures of the used lipids are presented in Figure 6.1

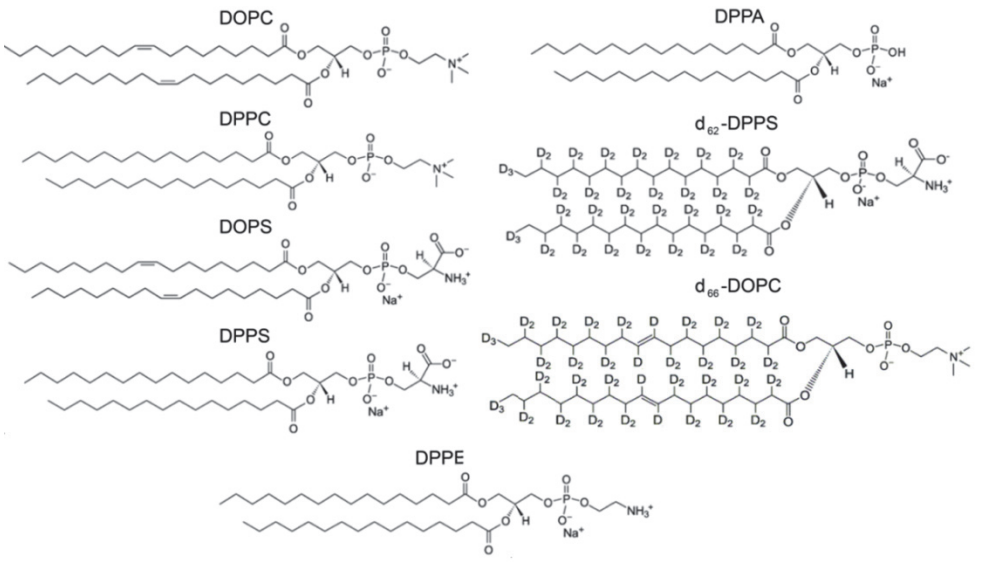

Figure 6.1. Chemical structures of the used phospholipids.

6.2.2 Sample preparation

Nanodroplets with a phospholipid monolayer were prepared according to the procedure described in Ref. [41]. We used 1 mM DPPC or DPPE on 2 vol. % d-hexadecane which gives saturated monolayer of lipid on oil droplets. The droplet size distribution was measured with dynamic light scattering (DLS, Zetasizer Nano ZS, Malvern). The droplets had a mean diameter of ~200 nm with a polydispersity index (PDI) of ~0.2.

Liposomes Small unilamellar vesicles were prepared by extrusion according to Ref. [42, 43]. Lipid stock solutions were created by dissolving the lipid powder in chloroform in a 4 ml glass vial with a PTFE screw cap. Stocks were stored at -20° C, but not for more than 6 months. First, multilamellar vesicles were created by pipetting the desired amounts of lipid stock solutions into a round-bottom glass tube using a glass syringe (Hamilton). When a mixture of different lipids was used, the desired amounts of the various lipid solutions were mixed together. While rotating the glass tube, a nitrogen gas stream was directed into the tube to evaporate the chloroform. The resulting lipid film was further dried in vacuum (<100 mbar, created by an oil-free diaphragm pump) at room temperature for at least 2 hours. Finally, the lipid film was re-suspended in D_2O or H_2O and vortexed. To create unilamellar vesicles, the resulting multilamellar vesicle solutions were extruded with a Miniextruder (AvantiPolarLipids, Al) using a polycarbonate membrane with a pore diameter of 100 nm at room temperature (or above their respective lipid transition temperature). Unilamellar

vesicles were stored in closed containers up to 2 weeks at 4 °C. The size and ζ-potential distribution of the liposomes were measured with DLS and laser Doppler electrophoresis at 25 °C (Malvern ZS nanosizer). To determine the size distribution of the vesicles, three subsequent measurements, each 11 runs, were averaged. To determine the ζ-potential of the vesicles three subsequent measurements, each 75 runs at automated voltage, were averaged. The liposomes were found to have a mean diameter in the range of 70 - 100 nm with a polydispersity index (PDI) of less than 0.1. The final lipid concentration was determined using a calorimetric phosphorus assay; for further details see Ref. [44]. The concentration of the lipids in the sample was 0.8 mg lipids/ml weight ratio for DLS, ζ-potential measurements, and SHS experiments. For sum frequency scattering the sample concentration was ~5 mg/ml. The mean values of DLS and ζ-potential measurements are summarized in Table 6.1 including the standard deviations of the mean from three consecutive measurements. The standard deviation of the distribution in a single measurement was 10% and 20% for size- and ζ-potential measurements, respectively.

Sample	Hydrodynamic diameter (nm)	ζ-potential (mV)
DPPS	98.4(0.5)	-45(1)
DOPC	94.0 (0.3)	-6(1)
DPPC	96.0 (0.3)	-4(1)
d_{66}-DOPC:DPPS	90.4(0.4)	-42(1)
DOPC:d_{62}-DPPS	69.8(0.3)	-43(1)
DOPC:DPPS	95.3(0.3)	-43(1)
d_{66}-DOPC:DPPA	99.2(0.5)	-36(1)
DOPS:DPPS	73.0(0.3)	-52(2)

Table 6.1 The results of dynamic light scattering and ζ-potential measurements. Standard deviations from the mean of three measurements are given in parenthesis.

6.2.3 Calculation of the orientational distribution of phosphate groups

The orientational analysis to calculate the ratio of SFS amplitudes in SSP and PPP polarization combinations of s-PO_2^- vibration is adapted from our procedure published earlier [41, 45] based on Rayleigh-Gans-Debye approximation in combination with nonlinear light scattering theory. We use a tilt angle ϕ of PO_2^- group to the surface normal and a twist angle ψ of the PO_2^- group about its

molecular axis with respect to the surface normal. This results in the following relation [46] between surface second order polarizability $\chi^{(2)}$ and molecular hyperpolarizabilities $\beta^{(2)}$:

$$\chi_{xxz}^{(2)} = \chi_{yyz}^{(2)} = \frac{1}{2}N(\beta_{aac}^{(2)}cos^2\psi + \beta_{bbc}^{(2)}sin^2\psi + \beta_{ccc}^{(2)})cos\phi + \frac{1}{2}N(\beta_{aac}^{(2)}sin^2\psi + \beta_{bbc}^{(2)}cos^2\psi - \beta_{ccc}^{(2)})cos^3\phi$$

$$\chi_{zzz}^{(2)} = N\left(\beta_{aac}^{(2)}sin^2\psi + \beta_{bbc}^{(2)}cos^2\psi\right)cos\phi - N(\beta_{aac}^{(2)}sin^2\psi + \beta_{bbc}^{(2)}cos^2\psi - \beta_{ccc}^{(2)})cos^3\phi \qquad (6.1)$$

with N being the surface density of PO_2^- groups. We assume that interface is azimuthally isotropic. The values of second order hyperpolarizability were taken from Ref. [46].

6.2.4 Calculation of the degree of asymmetry based on geometrical arguments

The number of lipids per leaflet can be calculated assuming that the liposomes have a spherical shape. We assume that each lipid headgroup occupies a constant area, *a*, which is the same at the inner and outer leaflets [10]. Then we get for the respective number difference (ΔN) between the outer leaflet and inner leaflet: $\Delta N = \frac{4\pi((R^2-(R-d)^2)}{a}$. ΔN can be expressed as a percentage of the total lipid number density per liposome (N_{tot}), which is given by $N_{tot} = \frac{4\pi((R^2+(R-d)^2)}{a}$. Here, *R* is the outer radius of the liposome and *d* is the membrane thickness, for which we take d ~ 5 nm.

6.2.5 Calculation of the degree of asymmetry from the SFS data

For a monodisperse solution the number densities (N_d) of nanodroplets can be calculated by dividing the volume concentration of oil (V_{oil}) by the volume of one droplet with radius R_d:

$$N_d = \frac{V_{oil}}{\frac{4}{3}\pi R_d^3} \qquad (6.2)$$

For liposomes we have a spherical bilayer rather than a sphere with radius R_{lip} and thickness *d* and lipid volume concentration V_{lip}, so that the number density is different:

$$N_{lip} = \frac{V_{lip}}{\frac{4}{3}\pi(R_{lip}^3 - (R_{lip}-d)^3)} \qquad (6.3)$$

For the calculation of the number density of liposomes we use d = 5 nm [47].

To extract the degree of asymmetry for a certain vibrational mode accounting for polydispersity, we fit the obtained spectra according to Eq. (2.15) and use the obtained amplitude $A_i(\theta)$ in the expression for α (Eq. (2.10)):

$$\alpha_{lip,i}(\theta, R_{eff,lip}) = \frac{|A_i(\theta)|^2}{N_{lip}R_{eff,lip}^6} \qquad (6.4)$$

This value is now independent of liposomes size, has been corrected for polydispersity and can be compared to other samples. For droplets we obtain the same expression.

6.3 Results and discussion

In what follows we first describe transmembrane hydration and lipid asymmetry for single component liposomes and then move on to binary mixtures. Finally, we aim to quantify the measured transmembrane asymmetry in terms of percentage number differences and differences in the orientational distributions of headgroups.

6.3.1 Single component liposomes

Starting with lipid hydration, Figure 6.2 A shows SHS patterns of single component liposomes made from DOPC, DPPC, and DPPS. The experimental procedure for the optical measurements can be found in Section 2.2.5. The data is scaled to correct for the difference in number density and size of the scatterers (see 2.1.1.1 and 2.1.1.2 for details). The SH signal is non-zero, which indicates that for these ~ 100 nm diameter liposomes the hydration environment of the inner leaflet is different from the outer leaflet. Also, charged DPPS liposomes generate ~21× more intensity per liposome than the zwitterionic, neutral, liposomes. This difference can be explained by the interaction of the electrostatic field of the headgroup charge with the adjacent water molecules, which induces changes in the orientational distribution of the interfacial water molecules and hence increases the SHS intensity. This effect is absent for zwitterionic lipids. Thus, we observe a sizeable asymmetry in the distribution of water molecules that is particularly sensitive to charge. Differently oriented hydrating water molecules in the inner and outer leaflets agree with the finding from X-ray, neutron and dynamic light scattering that the electron density is asymmetrically distributed across the leaflets of anionic vesicles [48]. They also agree with the commonly employed assumption that the inner leaflet is considered charge neutral [36].

Does such transmembrane hydration asymmetry require transmembrane lipid asymmetry as well? According to calculations assuming a spherical geometry and constant lipid headgroup areas [10] a number difference of 8 % should be present between the inner and outer leaflet of these liposomes (see section 6.2.4 for details). The difference in the number of lipids per leaflet can be estimated from SFS spectra, since SFS is exquisitely sensitive to transmembrane asymmetry. In particular, assuming a homogeneous distribution of lipid molecules, the SFS amplitude obtained from a sphere with a monolayer of lipids on its surface is proportional to the averaged projection of the molecular tilt angle on the interfacial normal, multiplied by the number of lipids present in the probed area. For purposes of brevity we refer to this as the ‘projected surface density’. For a liposome that has two oppositely oriented leaflets, the SFS amplitude reports on the transmembrane difference in projected surface density. Therefore, to quantify transmembrane lipid

asymmetry, we measured with SFS the headgroup intensity in the P-O stretch region of liposomes as well as the headgroup intensity of a DPPC monolayer on 100 nm hexadecane droplets in water with a known molecular area of 0.48 nm^2 per DPPC molecule [41]. Knowing the area per lipid of the nanodroplet system, the size distribution of the droplets, and having a reasonable estimate of the average tilt angle of the P-N headgroup, we can compute the amplitude per lipid molecule, which can be used to derive a detection limit in terms of transmembrane lipid asymmetry. Assuming that the cross sections of the vibrational modes and average chain orientation are comparable, our previously derived detection limit [49], can be converted to a lower limit for the detectable transmembrane number difference of ~ 2 %.

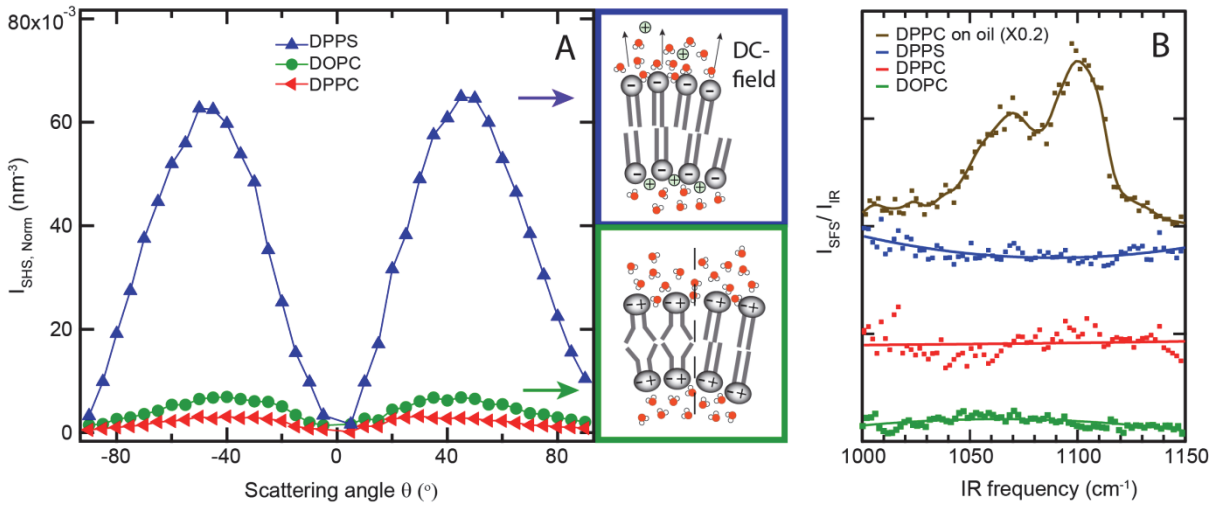

Figure 6.2. Liposome transmembrane asymmetry A: SHS patterns measured with all beams polarized parallel to the scattering plane (PP) of DPPS (blue), DOPC (green), and DPPC (red) liposomes in pure H_2O (0.8 mg/mL; extruded through a 100 nm pore). The scattering pattern originates from the overall transmembrane asymmetry in the orientational distribution of water molecules around the lipids (as illustrated in the cartoons). The data is scaled to correct for differences in size distribution and number density of the scatterers (as described in 2.1.1.1 and 2.1.1.2). B: SFS spectra of the same liposomes in D_2O in the P-O stretch region together with an SFS spectrum of hexadecane oil droplets covered with a DPPC monolayer (top trace). The spectra were collected with the IR (VIS, SF) beam polarized parallel (perpendicular) to the scattering plane (SSP). The SFS data are offset vertically for clarity.

Figure 6.2 B shows SFS spectra of the same liposomes as in Figure 6.2 A in the P-O stretch region: Within the signal to noise ratio of our instrument no apparent transmembrane lipid asymmetry is detected. For the C-H modes the same result was obtained (not shown). Thus, the lipid number difference for these single component liposomes is under our detection limit, meaning that the projected surface density difference is below 2 %. Comparing this to the 8 % in transmembrane lipid asymmetry [10] that can be found from a computation considering constant headgroup areas per leaflet, it appears that a different lipid hydration does not require transmembrane lipid

asymmetry in terms of a different number of lipids in the inner and outer leaflet. Instead, it may be influenced by specific lipid-lipid intermolecular interactions [50]. Such interactions would result in changes in the local (aqueous) environment of the lipids that can be probed in binary mixtures via the vibrational resonances of phospholipid headgroups.

6.3.2 The phosphate stretch mode is sensitive to the local environment

The symmetric (s)-PO_2^- stretch mode has been shown to be very sensitive to changes in intermolecular and H-bonding interactions as well as the local aqueous environment. Counter ion induced shifts in the s-PO_2^- stretch mode have been reported [46, 51]. Dehydration of a DPPC monolayer on a planar air/water interface results in a ~ 10 cm^{-1} spectral shift of the s-PO_2^- mode to higher frequencies [46]. In order to verify that the s-PO_2^- stretch vibration is indeed a sensitive probe for changes in the local environment / lipid-lipid interactions, we have measured vibrational SFS spectra of hexadecane droplets covered with a dense monolayer of DPPC (analyzed in detail in Ref. [41]) and of DPPE (1,2-dipalmitoyl-sn-glycero-3-phosphoethanolamine). It is worth noting that DPPE is different from DPPC in that it lacks the CH_3 groups around the N atom in the headgroup (Figure 6.1). For DPPE the amine and the phosphate group are expected to interact through intermolecular interactions [10], which results in an increase of the gel phase transition temperature from 314 K for DPPC to 336 K for DPPE. The SFS spectra for DPPC and DPPE covered hexadecane droplets in water are shown in Figure 6.3 A. The DPPC monolayer spectrum contains two peaks, one at ~1070 cm^{-1}, assigned to the s-(C=O)-O-C stretch mode, and one at ~1100 cm^{-1} assigned to the s-PO_2^- stretch mode of DPPC in a hydrated monolayer [41, 46, 52, 53]. The DPPE monolayer spectrum is different: it shows a single peak at ~1080 cm^{-1}. Based on the demonstrated sensitivity of the s-PO_2^- stretch mode on the local environment at the air/water interface, this peak likely originates from a population of H-bonded PE groups resulting in red shifted[1] s-PO_2^- stretch modes. In addition, since the s-PO_2^- mode consists of an isolated vibrational resonance it can easily be used to obtain the orientational distribution of the headgroups.

In what follows we use this mode as a probe to study transmembrane lipid asymmetry in liposomes composed of two different lipids. As a starting point, studies of giant unilamellar vesicles composed of PS lipids and a lipid of different acyl chain length [54, 55] can be used. These mixtures display phase separation behavior as a function of acyl chain conformation, and thus may exhibit a certain amount of transmembrane asymmetry.

[1] Although the mode at 1080 cm^{-1} could in principle be assigned to both modes the s-(C=O)-O-C stretch mode is not involved in any lipid specific interaction, which means it is an unlikely candidate for the assignment.

6.3.3 Liposomes from binary mixtures

Figure 6.3 B shows SFS spectra of liposomes in the P-O stretch region composed of a 1:1 mixture of DOPC:DPPS, DOPS:DPPC, DOPS:DPPS and DOPC:DPPA. As a comparison, the P-O signal from the DPPC monolayer is also shown (green curve). It can be seen that the DOPC:DPPS liposomes generate a non-zero SF spectrum. Compared to the spectrum of the PC headgroups in a DPPC monolayer, there is a single peak at ~1080 cm^{-1}. Based on the comparison between DPPC and DPPE monolayers in Figure 6.3 A, the 1080 cm^{-1} mode is likely assigned to a population of H-bonded s-PO_2^- stretch modes. Liposomes composed of a 1:1 DOPS:DPPC mixture possess the same headgroup chemistry, but they will likely have a different packing. It can be seen from Figure 6.3 B that these liposomes do not generate any detectable SFS intensity. Thus, in these mixtures all the lipid headgroups are distributed symmetrically across both leaflets (within the detection limit). The same is also true for DOPS:DOPC, and DPPS:DPPC mixtures (see Figure 6.4). Removing the amine group, but keeping the negative charge as in a DOPC:DPPA mixture also results in an absence of transmembrane asymmetry.

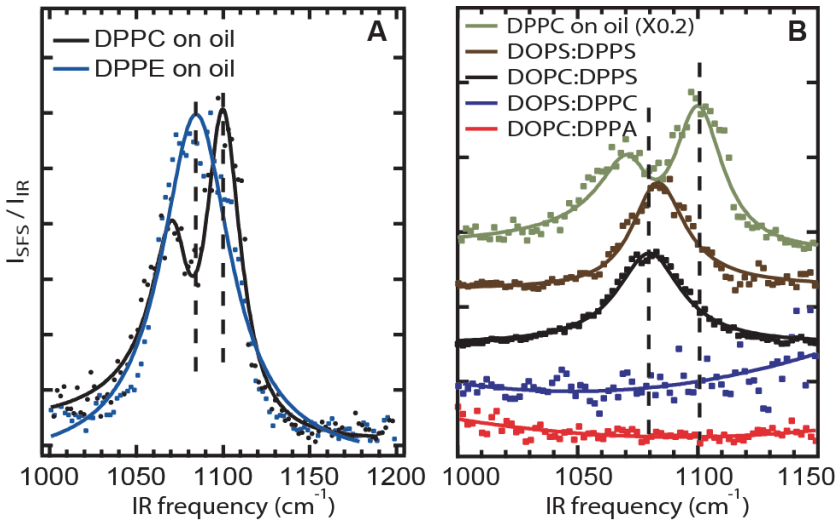

Figure 6.3. Transmembrane asymmetry. A: SFS spectra of DPPC (black) and DPPE (blue) monolayers on oil nanodroplets at maximum lipid coverage measured using the SSP polarization combination. The dashed lines show the positions of the PO_2^- symmetric stretch modes in DPPC and DPPE. B: SFS (SSP) spectra taken in the P-O stretch region of ~100 nm diameter liposomes in pure D_2O composed of 1:1 mixtures of DOPS:DPPS (brown), DOPC:DPPS (black), DOPS:DPPC (blue) and DOPC:DPPA (red) and the P-O spectrum of the liquid condensed like DPPC monolayer (with known headgroup area) on oil droplets (green). The SFS data are offset vertically for clarity.

Since the phosphate groups in the PA and PS headgroups are likely equally well hydrated, it appears, based on the observed differences in intensity, that a charged lipid with a free amine group is crucial for the observed transmembrane asymmetry. This apparent PS specificity is further investigated by measuring single lipid DOPS liposomes and DOPS:DPPS liposomes. The former displays a comparable hydration asymmetry as DPPS, with no apparent transmembrane asym-

metry (data not shown). A 1:1 DOPS:DPPS mixture, however, which possesses the same headgroup chemistry and the same difference in fatty acid tail chemistry as the DOPC:DPPS liposomes does display transmembrane asymmetry (Figure 6.3 B). For this binary lipid mixture, we observe the s-PO_2^- stretch mode at 1085 cm^{-1}, thus with a comparable frequency and intensity as for DOPC:DPPS liposomes. The measured PO_2^- modes represent the population of asymmetrically distributed phosphate groups between the leaflets.

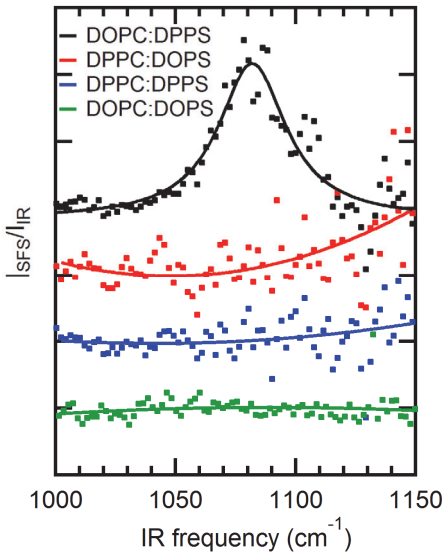

Figure 6.4 SFS spectra of mixtures of PC and PS lipids with different combinations of fatty acid tails: DOPC:DPPS (black), DPPC:DOPS (red), DPPC:DPPS (blue) and DOPC:DOPS (green).

In what follows we formulate a hypothesis to rationalize where this PO_2^- signal originates from and how intermolecular interactions are created.

6.3.4 Lipid-lipid interactions drive transmembrane asymmetry?

As Figure 6.3 B shows, in order to establish transmembrane asymmetry in the studied systems, charged PS headgroups are crucial ingredients. PS headgroups possess oppositely charged phosphate, carboxylate and amine groups, which can each participate in H-bonding interactions with a neighboring lipid and with water [15, 50, 56]. NH_4^+ ions as well as NH_3^+ groups are known to interact with PO_4^- groups of neighboring molecules [56-58] (in the fashion illustrated in Figure 6.5). However, as Figure 6.2 shows, no transmembrane lipid asymmetry is observed for pure DPPS liposomes, indicating that an additional criterion needs to be satisfied. Namely, a difference in the fatty acid chain length and associated packing appears to be necessary, as is also corroborated by the afore mentioned studies on giant unilamellar vesicles [54, 55]. We also confirmed that the s-PO_2^- stretch mode is sensitive to the local environment. Observing a similar red shift in the phos-

phate stretch mode as in the DPPE monolayer that exhibit headgroup-headgroup H-bonding interactions, it seems likely that intermolecular interactions are also crucial here.

Figure 6.5 A and B illustrate one possibility to explain the observed data: PS-PC headroups may interact through H_2N-H···O-PO H-bonding, which would shift the vibrational frequency of the interacting phosphate groups (on the PC lipids) to a lower frequency. In doing so, they become SFS active. This interaction can, however, only occur if the probability of intermolecular interactions is increased (compared to the pure DPPS or DOPS liposomes). By changing the lipid tails from DO (18 C atoms, one unsaturated bond) to the ~1 Å shorter DP tails [59] (16 C atoms, saturated) the distance between the H_2N-H and the O-PO groups is reduced, facilitating more favorable intermolecular interactions [15] in a mixture of DOPC with DPPS, or DOPS with DPPS. Although this explanation agrees with the presented data, it will have to be investigated in more details e.g. by employing molecular dynamics simulations.

Using this explanation and the C-H mode signal as a probe for lipid transmembrane asymmetry, and the phosphate stretch mode signal as a probe for (DOPC) lipids that are interacting with DPPS lipids we quantify both types of transmembrane asymmetry in the DOPC:DPPS liposomes.

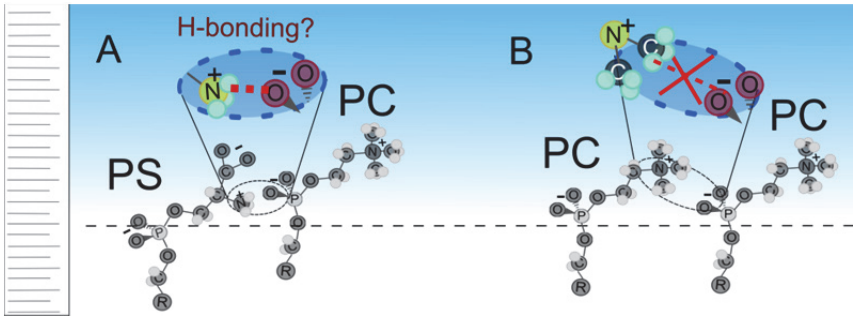

Figure 6.5 H-bonding interactions between lipids. The H-bonding interaction between phospholipid headgroups is determined by the lipid structure and by the headgroup- and fatty acid tail chemistry. A: For a PS – PC pair the H_2N-H…O-PO H-bond may be present depending on the distance between lipid headgroups (which can be changed by selecting proper combination of fatty acid tails). B: In contrast, for a PC – PC pair the headgroup chemistry is different and there is no possible intermolecular H-bonding.

6.3.5 Quantifying transmembrane asymmetry

To determine the percentage of lipids that are asymmetrically distributed across the membrane, we use selective deuteration and measure SFS spectra in the C-H stretch mode region, targeting the lipid fatty acid tails. Since C-D modes vibrate at different frequencies, the amount of lipid transmembrane asymmetry can be determined (as the C-H modes are insensitive to changes in the local environment).

Figure 6.6 A shows SFS spectra of liposomes in the C-H stretch region composed of a 1:1 mixture of d_{66}-DOPC:DPPS, and DOPC:d_{62}-DPPS. The C-H mode signal from the DPPC monolayer on oil droplets is shown in the top trace for comparison. The C-H mode region is comprised of the following peaks [29, 53, 60, 61]: the s-CH_2 stretch mode (~2852 cm^{-1}, d^+), the s-CH_3 stretch mode (~2876 cm^{-1}, r^+), the antisymmetric (as) CH_3 stretch mode (~2965 cm^{-1}, r^-), the s-CH_2-Fermi resonance (~2919 cm^{-1}, d^+_{FR}), the s-CH_3-Fermi resonance (~2935 cm^{-1}, r^+_{FR}) and the as-CH_2 stretch mode (~2905 cm^{-1}, d^-). It can be seen that the s-CH_3 stretch mode is dominant for the monolayer on droplets, which means that the alkyl chains are nearly all-trans in their conformation [41]. The liposomes with PS and PC mixtures display only a detectable SF response in the case of the d_{66}-DOPC:DPPS mixture, which indicates that only the DPPS molecules are asymmetrically distributed

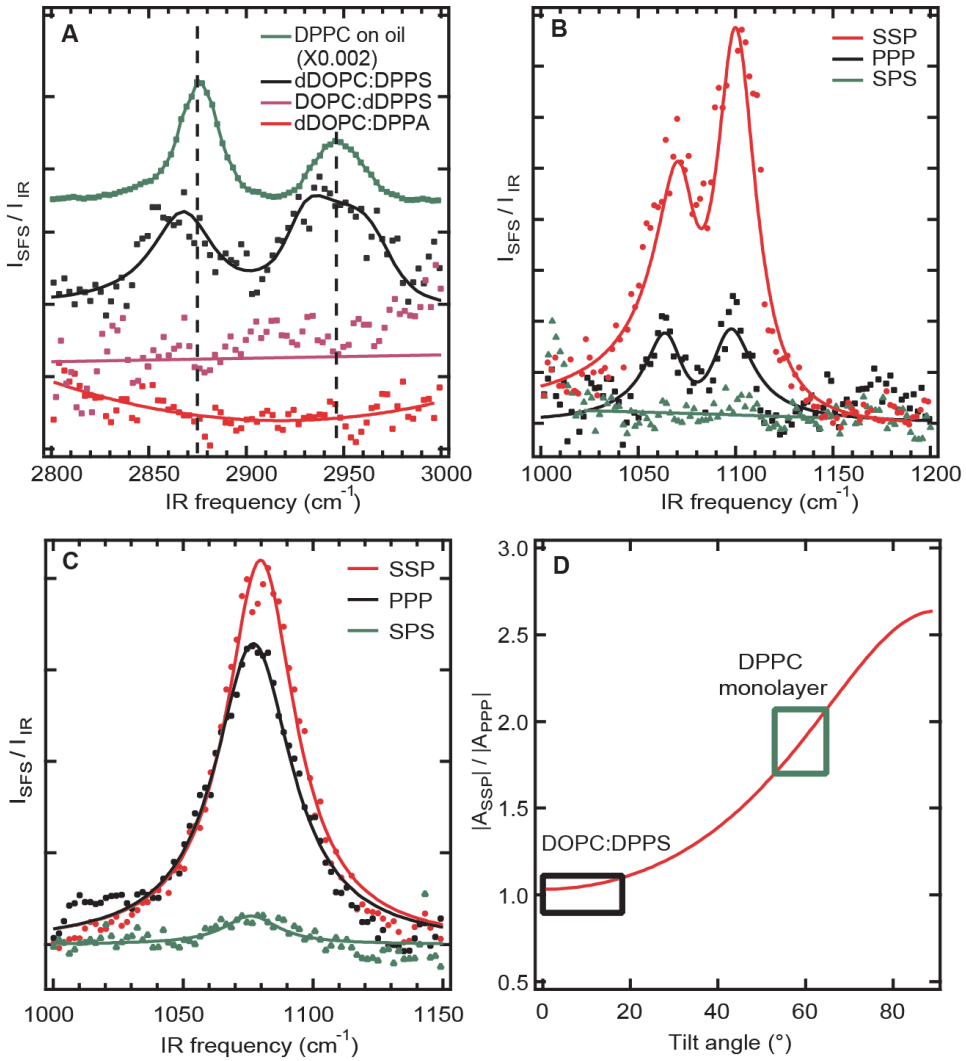

Figure 6.6. Quantifying transmembrane asymmetry. A: SFS (SSP) spectra taken in the C-H stretch region of ~100 nm diameter liposomes in pure water composed of 1:1 mixtures of d_{66}-DOPC:DPPS (black), DOPC:d_{62}-DPPS (purple) and d_{66}-DOPC:DPPA (red) and the spectrum of the DPPC monolayer on oil droplets (green). The solid lines represent fits to the data. The SFS data are offset vertically for clarity. B: SFS spectra of a DPPC monolayer on oil droplets, recorded in SSP (red), PPP (black) and SPS (green) polarization combinations. C: SFS spectra of DOPC:DPPS liposomes in SSP

(red), PPP (black) and SPS (green) polarization combinations. D: dependence of the amplitude ratio of the SSP and PPP polarization combinations of the s-PO_2^- stretch mode on the tilt angle (details of the computation can be found in section 6.2.3). The boxes indicate the measured ratios obtained from the spectra in panels B and C. Fitting parameters are given in the Table 6.2 and Table 6.3.

mode	ω_i (cm^{-1})	Υ_i (cm^{-1})	A_i
r^+	2868	20	0.15
d^+_{FR}	2926	16	0.11
r^-	2968	20	0.14
d^-	2906	20	0.02

Table 6.2 Fitted frequency, amplitude and linewidth for the SFS spectrum in the C-H and P-O stretch region of d_{66}-DOPC:DPPS liposomes.

Sample		DOPC:DPPS		DPPC on oil		DPPE on oil	DOPS:DPPS
Polarization		SSP	PPP	SSP	PPP	SSP	SSP
	A_i	1.13	1	1.85	1	1	1
ss PO_2^-	ω_i (cm^{-1})	1079	1079	1099	1096	1085	1083
	Υ_i (cm^{-1})	17	17	10	13	20	13
	A_i			1.31	0.93		
ss C-O-P	ω_i (cm^{-1})			1072	1066		
	Υ_i (cm^{-1})			20	12		

Table 6.3 Fitted frequency, amplitude and linewidth for the SFS spectra in the P-O stretch.

across the bilayer, and not the DOPC molecules (assuming that the deuteration procedure does not change any lipid properties, which is generally expected to be the case [62]). The SF spectrum of the DPPS molecules shows a prominent peak at 2870 cm^{-1}, which corresponds to the s-CH_3 stretch mode, while very little intensity is observed at 2850 cm^{-1}, indicating an all-trans conformation of the tails (identical to that of DPPC). We thus assume that the DP acyl tail conformations in both systems are equal. Comparing the obtained SFS intensity (α) of the s-CH_3 stretch mode for the d_{66}-DOPC:DPPS liposomes to that of the DPPC monolayer we find a transmembrane asymmetry in terms of the surface number density ratio ($n_{lip,DPPS}/n_d$) of:

$$\sqrt{\frac{\alpha_{lip}}{\alpha_d}}(C-H) = \frac{n_{lip,DPPS}}{n_d} \tag{6.5}$$

where α is scaled in order to be independent of the size of the droplet/liposome (see Eqs. (6.2)-(6.4) and sections 2.1.1.1, 2.1.1.2 and 6.2.5 for a derivation of all parameters). From Eq. (6.5) the transmembrane asymmetry is then determined for DPPS to be $\frac{n_{lip,DPPS}}{n_d,}$ = 0.16 (i.e. ~58 % of the DPPS molecules is located on the outer leaflet and ~42 % of the DPPS molecules is located on the inner leaflet, assuming similar sizes for DPPS and DPPC).

The orientational distribution <cos ϕ_d> (<cos ϕ_{lip}>) of the asymmetrically distributed phosphate headgroups on the DPPC covered droplets (DOPC:DPPS liposomes) can be estimated from polarization dependent SFS spectra. The data is shown in Figure 6.6 B and C. The angle ϕ represents the tilt angle of the symmetry axis of the s-PO_2^- mode with the surface normal of the liposome or droplet. To determine <cos ϕ_d>, the orientational analysis for polarization resolved SFS [41, 45] is extended to include a relationship between the second-order susceptibility and hyperpolarizability elements that uses a tilt (ϕ) and a twist (ψ) angle for the phosphate group. We follow here the procedure as introduced by the Allen lab [46]. The computed amplitude polarization ratio for the s-PO_2^- stretch mode for the case that $\psi=0$ [46] is displayed as a function of tilt angle in Figure 6.6 D. The experimentally measured scattering amplitude ratios obtained from Figure 6.6 B and C are indicated as rectangular areas in Figure 6.6 D and show that the phosphate groups of the DPPC molecules situated on oil droplets have an average tilt angle of ϕ=60±10° with respect to the droplet surface normal. Note that this is an advancement of the analysis in Ref. [46]. The calculated value is in good agreement with the tilt angle found for DPPC molecules at the air/water interface [46]. For the liposomes we find a tilt angle of ϕ=10±10°. Details about the analysis and numerical parameters can be found in Table 6.4, Table 6.5, Sections 2.2.4 and 6.2.3. Note that we have assumed a narrow Gaussian distribution for the tilt angle, as well as a uniform distribution of lipids. The latter is expected [63] since we have not detected any SFS signal in the polarization combinations PSP, PPS and SPP. Using a Gaussian distribution may not be completely justifiable since the number of participating lipids (several thousand) are not sufficient to make a statistical distribution.

Sample	DPPC on $C_{16}D_{34}$ (droplets)	d_{66}-DOPC:DPPS (liposomes)
R_{eff}, nm	97.6	41.4
concentration	2 vol. %	5 mg/ml
A_i, s-CH3 mode	3.87	0.15
$\frac{n_{sample}}{n_d}$, s-CH3 mode	1	0.16

Table 6.4 Calculation of the degree of transmembrane asymmetry for d_{66}-DOPC:DPPS liposomes, using a DPPC monolayer on an oil droplet with known lipid density as a reference.

Sample	R_{eff}, nm	$\frac{n_{sample}}{n_d}$, s-PO_2^- mode
DOPC:DPPS	33	0.95
d_{66}-DOPC:DPPS	44	0.88
DOPS:DPPS	33	0.92

Table 6.5 Calculation of the degree of head group orientation asymmetry for DOPC:DPPS and DOPS:DPPS liposomes, using a DPPC monolayer on an oil droplet with known lipid density as a reference.

To estimate the percentage of DOPC molecules that interact with DPPS, we compare the s-PO_2^- mode amplitude of the DOPC:DPPS mixtures and the DPPC monolayer. We use the following expression:

$$\sqrt{\frac{\alpha_{lip}}{\alpha_d}}(P-O) = \frac{n_{lip,DOPC}<\cos(\phi_{lip})>}{n_d <\cos(\phi_d)>} \tag{6.6}$$

The ratio $\sqrt{\frac{\alpha_{lip}}{\alpha_d}}(P-O)$ represents the amplitude ratio of the s-PO_2^- mode of the lipids in the liposomes and the droplet monolayers (corrected for the difference in droplet/liposome number density and size distribution). This number reports only on the head groups that exhibit intermolecular interactions, and thus likely on DOPC molecules. The ratio $\frac{n_{lip,DOPC}}{n_d}$ represents the number density ratio of the interacting DOPC lipids in the liposomes compared to the DPPC number density on the droplets. The orientational distribution is represented by <cos ϕ>, as discussed in the previous paragraph. From Figure 6.6 A we have $\sqrt{\frac{\alpha_{lip}}{\alpha_d}}(P-O)$= 0.9 ± 0.3. The factor $\frac{<\cos(\phi_{lip})>}{<\cos(\phi_d)>}$ = 2. From Eq. (6.6) we then have $\frac{n_{lip,DOPC}}{n_d}$ = 0.45. This means effectively that all the DOPC molecules in the outer leaflet are interacting with DPPS molecules. Note that in this analysis we implicitly assumed that the inner leaflet is charge neutral [36]. Since this means that the Na^+ counterions are in close proximity to the PS headgroups (but likely not ion paired so that no frequency shifts are detectable [64]), it will result in a much lower probability for intermolecular H-bonding in the inner leaflet between PS and PC headgroups.

Thus, from the analysis of the spectra in Figure 6.3 and Figure 6.6 (and relying on the interpretation in Figure 6.5) we find that there is a lipid number difference of ~16 % of DPPS between the inner and outer leaflets. There is no detectable difference in the number of DOPC lipids between the outer and inner leaflets. The shifted s-PO_2^- SFS response from the liposomes indicates that some of the DOPC molecules interact with DPPS through intermolecular H-bonding, which significantly alters the orientation of the headgroups towards a more parallel orientation with re-

spect to the surface plane. Assuming charge neutrality in the interior, and a consequential lack of intermolecular H-bonds, we find that nearly all of the DOPC in the outer leaflet interact with DPPS.

6.4 Conclusions

We find that charge and hydration transmembrane asymmetry is present in liposomes in aqueous solution, while for the same single component liposomes lipid transmembrane asymmetry is not detectable. Asymmetry in the number of lipids per leaflet can be induced by H-bond interactions between PS and PC/PS headgroups that depend on and can be influenced by varying the lipid structure. DOPC:DPPS liposomes exhibit a 16 % DPPS asymmetry but no detectable DOPC asymmetry. The P-O vibrational stretch mode intensity becomes clearly observable, indicating transmembrane asymmetry. This is related to a different orientational distribution of PC phosphate groups that participate in H-bond interactions with the PS amine groups. In particular we find that the average orientational angle with respect to the surface normal of the phosphate group becomes close to 10°, which is substantially different from the 60° that is found in a saturated monolayer. This indicates that in the liposomes the interacting headgroups of the DOPC are aligned along the interface (and thus occupy a maximum volume).

The presence of lipid transmembrane asymmetry and probable underlying mechanism offer insights into the complexity of lipid membrane chemistry. If specific/chemical interactions lead to the association of molecules in a 100 nm liposome then it is likely that similar mechanisms can play a role in the formation and stabilization of lipid domains. Lipid rafts are considered to be dynamic structures > 40 nm in size that form and dissolve on ms timescales [65]. As such our work provides insights into how these domains might form. Future work that is geared at further understanding the link between the transmembrane asymmetry studied here and lipid raft structure might involve nonlinear scattering experiments performed in all polarization combinations, which is sensitive to structural heterogeneities [63]. These measurements should be performed on liposomes with a diameter of ~ 10 μm, to enable the formation of multiple domains and to obtain good signal-to-noise ratios.

Given the importance of membrane properties and liposomes in basic biophysical research and biotechnology, our combination of SF and SH scattering techniques demonstrates a high potential to elucidate transmembrane asymmetry in lipid membranes. Particularly, these methods can be used to investigate lipid asymmetry induced by drug-membrane or biomacromolecule-membrane interactions along with domain formation in lipid mixtures.

6.5 References

1. Binder, W.H., V. Barragan, and F.M. Menger, *Domains and Rafts in Lipid Membranes.* Angew. Chem., Int. Ed., 2003. **42**(47): p. 5802-5827.
2. van Meer, G., D.R. Voelker, and G.W. Feigenson, *Membrane lipids: where they are and how they behave.* Nat. Rev. Mol. Cell Biol., 2008. **9**(2): p. 112-124.
3. Leventis, P.A. and S. Grinstein, *The Distribution and Function of Phosphatidylserine in Cellular Membranes.* Annu. Rev. Biophys., 2010. **39**(1): p. 407-427.
4. van Meer, G. and A. de Kroon, *Lipid map of the mammalian cell.* J. Cell Sci., 2011. **124**(1): p. 5-8.
5. Yeagle, P.L., W.C. Hutton, and R.B. Martin, *Transmembrane asymmetry of vesicle lipids.* J. Biol. Chem., 1976. **251**(7): p. 2110-2112.
6. Fadok, V.A. and P.M. Henson, *Apoptosis: Getting rid of the bodies.* Curr. Biol., 1998. **8**(19): p. R693-R695.
7. Cong, X., et al., *Unquenchable Surface Potential Dramatically Enhances Cu2+ Binding to Phosphatidylserine Lipids.* J. Am. Chem. Soc., 2015. **137**(24): p. 7785-7792.
8. Frechin, M., et al., *Expression of Nuclear and Mitochondrial Genes Encoding ATP Synthase Is Synchronized by Disassembly of a Multisynthetase Complex.* Mol. Cell, 2014. **56**(6): p. 763-776.
9. Frechin, M., et al., *Cell-intrinsic adaptation of lipid composition to local crowding drives social behaviour.* Nature, 2015. **523**(7558): p. 88-91.
10. Israelachvili, J.N., *Intermolecular and surface forces* 1991: Academic Press; New York.
11. Siu, S.W.I., et al., *Biomolecular simulations of membranes: Physical properties from different force fields.* J. Chem. Phys., 2008. **128**(12): p. 125103.
12. Brown, K.L. and J.C. Conboy, *Electrostatic Induction of Lipid Asymmetry.* J. Am. Chem. Soc., 2011. **133**(23): p. 8794-8797.
13. Anglin, T.C. and J.C. Conboy, *Lateral pressure dependence of the phospholipid transmembrane diffusion rate in planar-supported lipid bilayers.* Biophys. J., 2008. **95**(1): p. 186-93.
14. Liu, J. and J.C. Conboy, *Direct measurement of the transbilayer movement of phospholipids by sum-frequency vibrational spectroscopy.* J. Am. Chem. Soc., 2004. **126**(27): p. 8376-8377.
15. Berkowitz, M. and S. Pandit, *Molecular dynamics simulation of DPPC : DPPS bilayers in electrolyte solutions.* Biophys. J., 2003. **84**(2): p. 46a-46a.

16. Mondal, S. and C. Mukhopadhyay, *Molecular level investigation of organization in ternary lipid bilayer: A computational approach.* Langmuir, 2008. **24**(18): p. 10298-10305.
17. Vacha, R., et al., *Effects of Alkali Cations and Halide Anions on the DOPC Lipid Membrane.* J. Phys. Chem. A, 2009. **113**(26): p. 7235-7243.
18. Cascales, J.J.L., et al., *Model of an asymmetric DPPC/DPPS membrane: Effect of asymmetry on the lipid properties. A molecular dynamics simulation study.* J Phys Chem B, 2006. **110**(5): p. 2358-2363.
19. Kiessling, V., C. Wan, and L.K. Tamm, *Domain coupling in asymmetric lipid bilayers.* Biochim. Biophys. Acta, Biomembr., 2009. **1788**(1): p. 64-71.
20. Nakano, M., et al., *Determination of interbilayer and transbilayer lipid transfers by time-resolved small-angle neutron scattering.* Phys. Rev. Lett., 2007. **98**(23): p. 238101.
21. Veatch, S.L., et al., *Liquid domains in vesicles investigated by NMR and fluorescence microscopy.* Biophys. J., 2004. **86**(5): p. 2910-2922.
22. Serebryany, E., G.A. Zhu, and E.C.Y. Yan, *Artificial membrane-like environments for in vitro studies of purified G-protein coupled receptors.* Biochim. Biophys. Acta, Biomembr., 2012. **1818**(2): p. 225-233.
23. Richter, R.P., R. Berat, and A. A Brisson, *Formation of solid-supported lipid bilayers: An integrated view.* Langmuir, 2006. **22**(8): p. 3497-3505.
24. Hunt, J.H., P. Guyot-Sionnest, and Y.R. Shen, *Observation of C-H stretch vibrations of monolayers of molecules optical sum-frequency generation.* Chem. Phys. Lett., 1987. **133**(3): p. 189-192.
25. Harris, A.L., et al., *Monolayer vibrational spectroscopy by infrared-visible sum generation at metal and semiconductor surfaces.* Chem. Phys. Lett., 1987. **141**(4): p. 350-356.
26. Yan, E.C.Y., Z. Wang, and L. Fu, *Proteins at Interfaces Probed by Chiral Vibrational Sum Frequency Generation Spectroscopy.* J Phys Chem B, 2015. **119**(7): p. 2769-2785.
27. Johnson, C.M. and S. Baldelli, *Vibrational sum frequency spectroscopy studies of the influence of solutes and phospholipids at vapor/water interfaces relevant to biological and environmental systems.* Chem. Reviews, 2014. **114**(17): p. 8416-8446.
28. Boyd, R.W., *Nonlinear Optics (Third Edition)*2008, Burlington: Academic Press. 613.
29. Roke, S., et al., *Vibrational sum frequency scattering from a sub-micron suspension.* Phys. Rev. Lett., 2003. **91**: p. 258302.
30. Strader, M.L., et al., *Label-free spectroscopic detection of vesicles in water using vibrational sum frequency scattering.* Soft Matter, 2011. **7**(10): p. 4959-4963.
31. Roke, S. and G. Gonella, *Nonlinear Light Scattering and Spectroscopy of Particles and Droplets in Liquids.* Annu. Rev. Phys. Chem., 2012. **63**(1): p. 353-378.

32. Schürer, B., et al., *Probing colloidal interfaces by angle-resolved second harmonic light scattering.* Phys. Rev. B: Condens. Matter, 2010. **82**(24): p. 241404.
33. Wang, H., et al., *Second harmonic generation from the surface of centrosymmetric particles in bulk solution.* Chem. Phys. Lett., 1996. **259**(1–2): p. 15-20.
34. Eisenthal, K.B., *Second Harmonic Spectroscopy of Aqueous Nano- and Microparticle Interfaces.* Chem. Rev., 2006. **106**(4): p. 1462-1477.
35. Liu, J., et al., *Second Harmonic Studies of Ions Crossing Liposome Membranes in Real Time.* J Phys Chem B, 2008. **112**(48): p. 15263-15266.
36. Liu, Y., et al., *Surface potential of charged liposomes determined by second harmonic generation.* Langmuir, 2001. **17**(7): p. 2063-2066.
37. Rao, Y., et al., *Label-free probe of HIV-1 TAT peptide binding to mimetic membranes.* Proc. Natl. Acad. Sci. U. S. A., 2014. **111**(35): p. 12684-12688.
38. Yan, E.C.Y., Y. Liu, and K.B. Eisenthal, *In Situ Studies of Molecular Transfer between Microparticles by Second-Harmonic Generation.* J Phys Chem B, 2001. **105**(36): p. 8531-8537.
39. de Beer, A.G.F., R.K. Campen, and S. Roke, *Separating surface structure and surface charge with second-harmonic and sum-frequency scattering.* Phys. Rev. B, 2010. **82**(23): p. 235431.
40. Scheu, R., et al., *Charge Asymmetry at Aqueous Hydrophobic Interfaces and Hydration Shells.* Angew. Chem., Int. Ed., 2014. **53**(36): p. 9560-9563.
41. Chen, Y., et al., *Three Dimensional Nano "Langmuir Trough" for Lipid Studies.* Nano Lett., 2015. **15**(8): p. 5558-5563.
42. Hope, M.J., et al., *Production of large unilamellar vesicles by a rapid extrusion procedure. Characterization of size distribution, trapped volume and ability to maintain a membrane potential.* Biochim. Biophys. Acta, Biomembr., 1985. **812**(1): p. 55-65.
43. Macdonald, R.C., et al., *Small-Volume Extrusion Apparatus for Preparation of Large, Unilamellar Vesicles.* Biochim. Biophys. Acta, 1991. **1061**(2): p. 297-303.
44. Chen, P.S., T.Y. Toribara, and H. Warner, *Microdetermination of Phosphorus.* Anal. Chem., 1956(28): p. 1756-1758.
45. de Beer, A.G.F. and S. Roke, *Obtaining molecular orientation from second harmonic and sum frequency scattering experiments in water: Angular distribution and polarization dependence.* J. Chem. Phys., 2010. **132**(23): p. 234702.
46. Casillas-Ituarte, N.N., et al., *Na+ and Ca2+ Effect on the Hydration and Orientation of the Phosphate Group of DPPC at Air−Water and Air−Hydrated Silica Interfaces.* J Phys Chem B, 2010. **114**(29): p. 9485-9495.

47. Gramse, G., et al., *Nanoscale Measurement of the Dielectric Constant of Supported Lipid Bilayers in Aqueous Solutions with Electrostatic Force Microscopy.* Biophys. J., 2013. **104**(6): p. 1257-1262.
48. Anghel, V.N.P., et al., *Scattering from laterally heterogeneous vesicles. II. The form factor.* J. Appl. Crystallogr., 2007. **40**(3): p. 513-525.
49. Jena, K.C., R. Scheu, and S. Roke, *Surface impurities are not responsible for the charge on the oil/water interface: a comment.* Angew. Chem., Int. Ed., 2012. **51**(52): p. 12938-12940.
50. Pandit, S.A., D. Bostick, and M.L. Berkowitz, *Mixed Bilayer Containing Dipalmitoylphosphatidylcholine and Dipalmitoylphosphatidylserine: Lipid Complexation, Ion Binding, and Electrostatics.* Biophys. J., 2003. **85**(5): p. 3120-3131.
51. Casal, H.L., et al., *Infrared and 31P-NMR studies of the effect of Li+ and Ca2+ on phosphatidylserines.* BBA - Lipid Lipid Met., 1987. **919**(3): p. 275-286.
52. Chen, X. and H.C. Allen, *Interactions of Dimethylsulfoxide with a Dipalmitoylphosphatidylcholine Monolayer Studied by Vibrational Sum Frequency Generation.* J. Phys. Chem. A, 2009. **113**(45): p. 12655-12662.
53. Liljeblad, J.D.F., et al., *Phospholipid Monolayers Probed by Vibrational Sum Frequency Spectroscopy: Instability of Unsaturated Phospholipids.* Biophys. J., 2010. **98**(10): p. L50-L52.
54. Shimokawa, N., et al., *Phase separation of a mixture of charged and neutral lipids on a giant vesicle induced by small cations.* Chem. Phys. Lett., 2010. **496**(1–3): p. 59-63.
55. Bandekar, A. and S. Sofou, *Floret-Shaped Solid Domains on Giant Fluid Lipid Vesicles Induced by pH.* Langmuir, 2012. **28**(9): p. 4113-4122.
56. Pandit, S.A. and M.L. Berkowitz, *Molecular Dynamics Simulation of Dipalmitoylphosphatidylserine Bilayer with Na+ Counterions.* Biophys. J., 2002. **82**(4): p. 1818-1827.
57. Petrache, H.I., et al., *Structure and Fluctuations of Charged Phosphatidylserine Bilayers in the Absence of Salt.* Biophys. J., 2004. **86**(3): p. 1574-1586.
58. Mukhopadhyay, P., L. Monticelli, and D.P. Tieleman, *Molecular Dynamics Simulation of a Palmitoyl-Oleoyl Phosphatidylserine Bilayer with Na+ Counterions and NaCl.* Biophys. J., 2004. **86**(3): p. 1601-1609.
59. Nagle, J.F. and S. Tristram-Nagle, *Structure of lipid bilayers.* BBA - Rev. Biomembranes, 2000. **1469**(3): p. 159-195.
60. Walker, R.A., J.C. Conboy, and G.L. Richmond, *Molecular Structure and Ordering of Phospholipids at a Liquid−Liquid Interface.* Langmuir, 1997. **13**(12): p. 3070-3073.

61. Liu, J. and J.C. Conboy, *1,2-diacyl-phosphatidylcholine flip-flop measured directly by sum-frequency vibrational spectroscopy.* Biophys. J., 2005. **89**(4): p. 2522-2532.
62. Tokutake, N., et al., *Quantifying the Effects of Deuterium Substitution on Phospholipid Mixing in Bilayer Membranes. A Nearest-Neighbor Recognition Investigation.* J. Am. Chem. Soc., 2003. **125**(51): p. 15764-15766.
63. de Beer, A.G.F., S. Roke, and J.I. Dadap, *Theory of optical second-harmonic and sum-frequency scattering from arbitrarily shaped particles.* J. Opt. Soc. Am. B, 2011. **28**(6): p. 1374-1384.
64. N. F. A. van der Vegt, K.H., S. Roke, J. Zheng, M. Lund, and H. J. Bakker, *Water-Mediated Ion Pairing: Occurrence and Relevance.* Chem. Rev., 2016. **116**.
65. Honigmann, A., et al., *STED microscopy detects and quantifies liquid phase separation in lipid membranes using a new far-red emitting fluorescent phosphoglycerolipid analogue.* Faraday Discuss., 2013. **161**(0): p. 77-89.

Chapter 7: Conclusions and outlook

7.1 Achieved results

In this thesis, nonlinear optical scattering techniques were applied to study curved interfaces of water in contact with hydrophobic solvents or model cell membranes. We first introduced the topic and state-of-the-art of the field. Then we described the techniques and the experimental setups. Here, sum frequency and second harmonic scattering techniques were applied for the first time to study: a liquid jet surface, water droplets, and phospholipid liposomes. The obtained results help to understand chemistry and structure of the interfaces. Furthermore, this work has expanded the range of applications of the second harmonic and sum frequency scattering spectroscopies.

In Chapter 3 we described SHS and SFS experiments performed on the surface of a liquid microjet. This measurement is similar to the measurement of the surface second harmonic or sum frequency generation in the transmission geometry. The jet can focus a beam leading to an enhanced nonlinear signal from the inner surface. In addition, application of a jet eliminates heating effects due to the continuous refreshment of the surface.

In Chapter 4 we applied sum frequency scattering spectroscopy to study water droplets dispersed in oil. We compared spectra of water droplets with equivalent planar interfaces and concluded that the strength of H-bonding of water molecules at the surface of droplet corresponds to that of a planar interface at a 50°C lower temperature. Surprisingly, the surface structure of supercooled droplets remains the same. Below the homogeneous ice nucleation temperature, the SFS spectrum of the frozen droplets is similar to the spectrum of the surface of the ice crystal. These findings are important for the chemistry of hydrophobic interfaces and confined water.

In Chapter 5 we used second harmonic scattering to study water droplets dispersed in CCl_4 stabilized with the anionic surfactant AOT. The analysis of angular-resolved second harmonic scattering data gave surface potential, ionic strength, and water ordering parameters. These fitting parameters give a different type of changes in the scattering patterns and thus can be resolved independently. Using this analysis we mapped surfactant induced structural changes in the surface water and potential and found that interface acts as a nucleation site for micelles.

In Chapter 6 we applied second harmonic scattering and sum frequency spectroscopy to a biological interface, a lipid bilayer in the form of a liposome in water. We found that the liposomes exhibit asymmetry in water ordering between the inner and outer parts. For a certain combination

of lipids, the formation of H-bonds between phosphate and amine groups of headgroups of different lipid molecules was observed. The asymmetry in the distribution of lipid molecules was detected and quantified. In addition, the analysis of orientation of phosphate headgroups was performed.

7.2 Future development

This work has opened many possible directions for future studies. More experiments can be carried out based on the background presented in this work. In Chapter 3 we described the possibility to measure SHS and SFS using the liquid jet. The measurement of the SHS and SFS data using constantly flowing surfaces opens ways for new experiments. The liquid microjet technique was initially developed to perform X-ray photoelectron spectroscopy and other vacuum experiments. Experiments combining optical and X-ray measurements may provide additional insights. In addition, because of short equilibration time of the interface after it exits the nozzle, and by measuring at different distances from the nozzle one could study the kinetics of surfactants at water/air interface using SFS on the liquid jet.

In Chapter 4 we discussed water structure in water droplets dispersed in a hydrophobic solvent. We showed that water has enhanced ordering at the hydrophobic interface. In future, regarding the chemistry of emulsions, it would be interesting to compare the surface densities or orientation of surfactants in the oil-in-water emulsion and in the complimentary water-in-oil emulsion. These systems are typically stabilized with different surfactants, but often combinations of two co-surfactants can be used. The interface of a droplet in the emulsion is almost flat on the molecular scale; nonetheless, the properties of interfaces may be drastically different. Furthermore, follow-ups may be devoted to the structure of water at hydrophobic droplet interfaces in presence of salts, acids, and bases.

In Chapter 5 the SHS technique was applied to study water droplets in the non-polar solvent. This technique enables the estimation of concertation of free charge carriers and surface potential in non-polar solvents using different surfactants and types of particles. A possible application is the study of water droplets dispersed in chloroform stabilized with phospholipids. This example could provide some insights about confined water in biologically relevant environment.

In Chapter 6 we discussed SFS measurements on single-lipid liposomes and liposomes composed of binary mixtures of lipids. The interaction of liposomes with proteins such as phospholipases can potentially be detected using SHS (as a change in interfacial charge) or with SFS (by looking on vibrational modes of the headgroup). The detailed study of surface potential and charge condensation in liposomes composed of binary mixtures of lipids was published after we performed this study [1]. There are different values of the rate of trans-leaflet motion reported in the literature. However, labels and support may affect this rate. Recently developed techniques allow the produc-

tion of asymmetric liposomes [2]. Using these samples and with deuteration of one of the lipids in the mixture trans-leaflet motion rate can be calculated from the time dependence of the SFS signal, with the advantage of using label-free measurement and without the influence of the support.

7.3 References

1. Lütgebaucks, C., C. Macias-Romero, and S. Roke, Characterization of the interface of binary mixed DOPC:DOPS liposomes in water: The impact of charge condensation. J. Chem. Phys., 2017. **146**(4): p. 044701.

2. Heberle, F.A., et al., Subnanometer Structure of an Asymmetric Model Membrane: Interleaflet Coupling Influences Domain Properties. Langmuir, 2016. **32**(20): p. 5195-5200.

List of publications

This thesis is based on the following publications/manuscripts:

1. **Smolentsev, N.,** and Roke, S., *Surface potential, ion pairing and surface water order on water droplets dispersed in non-polar solvent,* in preparation

2. **Smolentsev, N.**, Smit, W.J., Bakker, H.J., and Roke, S., *The interfacial structure of water droplets in a hydrophobic liquid.* Nature Communications, 2017, 8, 15548.

3. **Smolentsev, N.**, Lütgebaucks, C., Okur, H.I., de Beer, A.G.F., and Roke, S., *Intermolecular Headgroup Interaction and Hydration as Driving Forces for Lipid Transmembrane Asymmetry.* Journal of the American Chemical Society, 2016. 138 p. 4053-4060.

4. **Smolentsev, N.**, Chen, Y., Jena, K.C., Brown, M.A., and Roke, S., *Sum frequency and second harmonic generation from the surface of a liquid microjet.* The Journal of Chemical Physics, 2014. 141 p. 18C524.

The introductory chapter is partially based on this paper:

5. Samson, J.-S., Scheu, R., **Smolentsev, N.**, Rick, S.W., and Roke, S., *Sum frequency spectroscopy of the hydrophobic nanodroplet/water interface: Absence of hydroxyl ion and dangling OH bond signatures.* Chemical Physics Letters, 2014. 615 p. 124-131. Frontiers article, on the journal's cover

Other publications/manuscripts by the author not described within this thesis:

6. Zdrali, E., Etienne, G., **Smolentsev, N.**, Amstad, E., Roke, S. *Correlating droplet stability with surfactant surface structure*, in preparation

7. Kovacik F., Okur H.I., **Smolentsev, N.**, Scheu R., and Roke, S., *Hydration mediated surface structural transitions on mixed hydrophobic/hydrophilic nanodroplet interfaces*, submitted to Physical Chemistry Chemical Physics

8. Okur H.I., **Smolentsev, N.**, Scheu R., and Roke, S*., Probing the surface of oil nanodroplets with bulk fluorescence measurements,* in preparation

9. Olenick L.L., Troiano J.M., **Smolentsev N.**, Ohno P.E., Roke S., Geiger F.M., S*um frequency scattering spectroscopy of the interactions of cationic polymers and phospholipid monolayers on oil nanodroplets,* in preparation

10. Okur, H., Chen, Y., **Smolentsev, N.**, Zdrali, E. Roke, S., *Interfacial Structure and Hydration of 3D-Lipid Monolayers in Aqueous Solution*, Journal of Physical Chemistry B, 2017, **121**, pp 2808–2813.

11. Smit, W.J., **Smolentsev, N.**, Versluis, J., Roke, S., and Bakker, H.J., *Freezing effects of oil-in-water emulsions studied by sum-frequency scattering spectroscopy.* The Journal of Chemical Physics, 2016. 145 p. 044706.

12. **Smolentsev, N.**, Sikora, M., Soldatov, A.V., Kvashnina, K.O., and Glatzel, P., *Spin-orbit sensitive hard X-ray probe of the occupied and unoccupied 5d density of states.* Physical Review B, 2011. 84 p. 235113.

13. **Smolentsev, N.**, Smolentsev, G., Wei, S., and Soldatov, A.V., *Local atomic structure around Mn ions in GaN:Mn thin films: Quantitative XANES analysis.* Physica B: Condensed Matter, 2011. 406 p. 2843-2846.

14. **Smolentsev, N.**, Soldatov, A.V., Smolentsev, G., and Wei, S.Q., *Determination of the 3D atomic spatial distribution around Mn in (Mn, Zn)O films using multidimensional interpolation of XANES spectra.* Solid State Communications, 2009. 149 p. 1803-1806.

15. **Smolentsev, N.**, Guda, A.A., Safonova, O.V., Soldatov, M.A., Paun, C., Smolentsev, G., van Bokhoven, J.A., and Soldatov, A.V., *Application Ce L 1 HERFD XAS to determine the atomic structure of CeO_2 based nano-catalysts under working conditions.* Journal of Physics: Conference Series, 2013. 430 p. 012062.

16. Safonova, O.V., Guda, A.A., Paun, C., **Smolentsev, N.**, Abdala, P.M., Smolentsev, G., Nachtegaal, M., Szlachetko, J., Soldatov, M.A., Soldatov, A.V., and van Bokhoven, J.A., *Electronic and Geometric Structure of Ce^{3+} Forming Under Reducing Conditions in Shaped Ceria Nanoparticles Promoted by Platinum.* The Journal of Physical Chemistry C, 2014. 118 p. 1974-1982.

17. Guda, A.A., **Smolentsev, N.**, Rovezzi, M., Kaidashev, E.M., Kaydashev, V.E., Kravtsova, A.N., Mazalova, V.L., Chaynikov, A.P., Weschke, E., Glatzel, P., and Soldatov, A.V., *Spin-polarized electronic structure of the core-shell ZnO/ZnO:Mn nanowires probed by X-ray absorption and emission spectroscopy.* Journal of Analytical Atomic Spectrometry, 2013. 28 p. 1629-1637.

18. Lomachenko, K.A., Garino, C., Gallo, E., Gianolio, D., Gobetto, R., Glatzel, P., **Smolentsev, N.**, Smolentsev, G., Soldatov, A.V., Lamberti, C., and Salassa, L., *High energy resolution core-level X-ray spectroscopy for electronic and structural*

characterization of osmium compounds. Physical Chemistry Chemical Physics, 2013. 15 p. 16152-16159.

19. Glatzel, P., Weng, T.-C., Kvashnina, K., Swarbrick, J., Sikora, M., Gallo, E., **Smolentsev, N.**, and Mori, R.A., *Reflections on hard X-ray photon-in/photon-out spectroscopy for electronic structure studies.* Journal of Electron Spectroscopy and Related Phenomena, 2013. 188 p. 17-25.

20. Garino, C., Gallo, E., **Smolentsev, N.**, Glatzel, P., Gobetto, R., Lamberti, C., Sadler, P.J., and Salassa, L., *Resonant X-ray emission spectroscopy reveals d-d ligand-field states involved in the self-assembly of a square-planar platinum complex.* Physical Chemistry Chemical Physics, 2012. 14 p. 15278-15281. on the journal's cover

21. Smirnova, Y.O., **Smolentsev, N.**, Guda, A.A., Soldatov, M.A., Kvashnina, K.O., Glatzel, P., Korotaev, E.V., Soldatov, A.V., and Mazalov, L.N., *Local surrounding of vanadium atoms in* $CuCr_{1-x}V_xS_2$*: X-ray absorption spectroscopy analysis.* Optics and Spectroscopy, 2013. 114 p. 397-400.

22. Guda, A.A., **Smolentsev, N.**, Verbeeck, J., Kaidashev, E.M., Zubavichus, Y., Kravtsova, A.N., Polozhentsev, O.E., and Soldatov, A.V., *X-ray and electron spectroscopy investigation of the core–shell nanowires of ZnO:Mn.* Solid State Communications, 2011. 151 p. 1314-1317.

23. Guda, A.A., Lau, S.P., Soldatov, M.A., **Smolentsev, N.**, Mazalova, V.L., Ji, X.H., and Soldatov, A.V., *Copper defects inside AlN:Cu nanorods – XANES and LAPW study.* Journal of Physics: Conference Series, 2009. 190 p. 012136.

These papers received 171 citations and H-index = 9 (Web of Science, October 2017).

Curriculum Vitae

Nikolay SMOLENTSEV (Николай Юрьевич Смоленцев)

E-mail: Nikolay.Smolentsev@gmail.com

Address: av. du 1er Mai 8 bis, 1020 Renens, Switzerland

Date and place of birth: 19.12.1989, Rostov-on-Don, Russia

Citizenship: Russia

Marital status: Married, 2 children

EDUCATION

Ph.D.	in photonics, EPFL, Lausanne	2017
M.Sc.	in physics, cum laude, Southern Federal University, Rostov-on-Don, Russia	2012
B.Sc.	in physics, cum laude, Southern Federal University, Rostov-on-Don, Russia	2010

HONORS AND AWARDS

Best poster award at Future of Chemical Physics Conference, Oxford, UK	2016
Best student of Rostov-on-Don in research	2012
Best student of Southern Federal University in research	2012
Fellowship of President of Russian Federation for study abroad	2010
(given only to 40 best students in all subject in Russia per year)	
Fellowship from the German-Russian Interdisciplinary Science Center DAAD	2010
Fellowship for Excellent Students from the Center-Invest Bank	2009,2011,2012

WORK EXPERIENCE

École polytechnique fédérale de Lausanne 2012-2017

Ph.D. student in Laboratory for fundamental BioPhotonics (under supervision of prof. Sylvie Roke)

Operation and alignment of TiSa lasers (SpecraPhysics SpitFire and Quantronix Integra-C and ADD-ON) and OPAs (TOPAS, Light Conversion, old and new generations, ORPHEUS)

Sum frequency and second harmonic measurements of colloids using home-made setup

Data analysis using Mathematica, Matlab, and IgorPro software

Design and validation of custom temperature cells for two setups

FTIR, dynamic light scattering and UV-VIS measurements

Wet lab experience: preparation of water-in-oil and oil-in-water emulsions

European Synchrotron Radiation Facility, Grenoble, France 2010-2011

Trainee (10 months), ID26, under supervision of Dr. Pieter Glatzel

Experiments and simulations for X-ray absorption and emission spectroscopy using Matlab and DFT calculations

Research Center "Smart Materials", SFedU, Rostov-on-Don, Russia 2006-2011

Part-time Junior Researcher, under supervision of Prof. Alexander Soldatov

X-ray spectroscopy studies of diluted magnetic semiconductors (theoretical and experimental), Participation in measurements at synchrotrons

SELECTED CONFERENCES

Swiss Chemical Society Fall Meeting, Bern, Switzerland, poster	2017
Future of Chemical Physics, Oxford, UK, poster	2016
"Water & Aqueous Solutions" Gordon Research Conference, Holderness, USA, poster	2014
Condensed Matter in Paris, oral	2014

COMPUTER SKILLS

Mathematica, Matlab, Origin, Igor Pro, Adobe Illustrator, SolidWorks, Linux, MS Office

TEACHING EXPERIENCE

Teaching assistant of Prof. Sylvie Roke for

Interfaces for biology and nanoscience, Nonlinear optics, Nonlinear spectroscopy

LANGUAGES

English: Advanced (C2)

French: Fluent (B2)

Russian: Native

HOBBIES

Chess, guitar, basketball